Dynamics and Interactions of Cavity Solitons in Photonic Devices

A thesis presented in fulfilment
of the requirements for the degree of
Doctor of Philosophy

Craig McIntyre
Department of Physics, University of Strathclyde

2013

This thesis is the result of the author's original research. It has been composed by the author and has not been previously submitted for examination which has led to the award of a degree.

Signed: Date:

For their love, support and encouragement
I dedicate this work to my children,
Rebecca, Eilidh and Ruaridh.

Acknowledgements

I would like to firstly thank my supervisor, Gian-Luca Oppo, for all of his help, guidance and patience throughout my studies. I am so grateful for this support, without which, I would not have made it this far. I would like to acknowledge and thank Alison Yao, Willie Firth, Franco Prati, Giovanna Tissoni, Massimo Giudicci and Pavel Paulau for their efforts in collaboration with my work. I would also like to thank those from the photonics group, in particular Thorsten Ackemann, Neal Radwell and Yoann Noblet, who have provided valuable insight and collaboration with the experimental side of the work on this subject.

Finally, I would like to thank my family. My wife, Laura, my children, Rebecca, Eilidh and Ruaridh and my Mum. Their continued support and patience has been a great help throughout my studies.

Abstract

In this thesis, we present a theoretical and numerical study of the properties and dynamics of cavity solitons in photonic systems. Three systems are investigated – a semiconductor laser with optical injection, a semiconductor laser with frequency selective feedback and a nonlinear cavity with a Kerr material. Cavity solitons have common features which can be observed in all three systems as well as properties which are unique to each specific system. The writing and erasing process under the action of an external pump is characterised first leading to the establishment and subsequent erasure of stable cavity solitons in these systems. In general a coherent writing beam is used, although in the case of lasers with frequency selective feedback an incoherent writing beam is required. Switch-on time is measured, allowing for optimisation of the writing process. Cavity soliton drift is introduced by manipulating the detuning and, where appropriate, the phase of the optical injection. Phase modulations of the optical injections are preferable as cavity solitons remain stable over a larger range of parameters, although this is not always possible. Cavity soliton interactions are particularly interesting, with collisions resulting in differing behaviour in each system, including locking, merging and the annihilation of the two cavity solitons. Furthermore Adler-type locking is shown for two cavity solitons pinned by localised defects in the detuning by varying the depth of one defect with respect to the other. Finally, oscillating and pulsing regimes of cavity solitons are investigated in the laser with frequency selective feedback. Unlocked oscillations and mode-locked oscillations and pulses are described with the possible observation of fully self localised three dimensional pulses or "light bullets." The intriguing properties of cavity solitons investigated in this thesis can be of practical application in the realisation and optimisation of optical memories, optical delay lines and optical logic gates.

Publications and conference presentations

Publications

- C. McIntyre, A.M. Yao, G.-L. Oppo, F. Prati and G. Tissoni, "All-optical delay line based on a cavity soliton laser with injection,"*Phys. Rev. A* **81**, 013838 (2010).

- F. Prati, G. Tissoni, C. McIntyre and G.-L. Oppo, "Static and dynamic properties of cavity solitons in VCSELs with optical injection," *Eur. Phys. J. D* **59**, 139 (2010).

- N. Radwell, C. McIntyre, A.J. Scroggie, G.-L. Oppo, W.J. Firth and T. Ackemann, "Switching spatial dissipative solitons in a VCSEL with frequency selective feedback," *Eur. Phys. J. D* **59**, 121 (2010)

- P.V. Paulau, C. McIntyre, W.J. Firth, Y. Noblet, T. Ackemann, P. Colet, G.-L. Oppo "Adler synchronization of spatial laser solitons pinned by defects," *Phys. Rev. Lett.* **108** 213904 (2012)

- T. Ackemann, Y. Noblet, P.V. Paulau, C. McIntyre, P. Colet, W.J. Firth, G.-L. Oppo "Frequency and phase locking of laser cavity solitons" *contributed book chapter awaiting publication.*

Conference presentations

- C. McIntyre, A.M. Yao, F. Prati, G. Tissoni and G.-L. Oppo, "All-Optical Delay Line with a Cavity Soliton Laser," in *CLEO/Europe and EQEC 2009 Conference Digest* (Optical Society of America, 2009).

- C. McIntyre, F. Prati, G. Tissoni and G.-L Oppo, "Motion of cavity solitons in VCSELs with optical injection," in *Photon 10 Conference Digest* (Institute of Physics, 2010).

- C. McIntyre, N. Radwell, G.-L. Oppo, W.J. Firth, A.J. Scroggie and T. Ackemann, "Transient and sustained oscillations of cavity solitons in VCSELs with frequency selective feedback," in *Photon 10 Conference Digest* (Institute of Physics, 2010).

- C. McIntyre, G.-L. Oppo, W.J. Firth, A.J. Scroggie, N. Radwell and T. Ackemann, "Spatial dissipative solitons in lasers with delayed feedback: theory and experiment," at *Patterns,Nonlinear Dynamics and Applications (PANDA) meeting* (University of Bristol, 2010).

- C. McIntyre, G.-L. Oppo, N. Radwell, T. Ackamann and W.J. Firth, "Mode-locked laser cavity solitons," in *CLEO/Europe and EQEC 2011 Conference Digest* (Optical Society of America, 2011).

- M. Zajnulina, C. McIntyre, and G. Oppo, "Locking and Merging of Cavity Solitons," in CLEO/Europe and EQEC 2009 Conference Digest, (Optical Society of America, 2009).

- C. McIntyre, G.-L. Oppo, G. Tissoni and F. Prati, "Moving and merging of spatial dissipative solitons in lasers with a periodically structured background," at Complexity in Periodically Structured Systems International Workshop, (Max Planck Institute for the Physics of Complex Systems, 2010).

- C. McIntyre, G.-L. Oppo, N. Radwell, Y. Noblet, T. Ackamann, W.J. Firth and P. Paulau, "Frequency and phase locking in a cavity soliton laser," in *CLEO/Europe and EQEC 2011 Conference Digest*, (Optical Society of America, 2011).

Table of Contents

Chapter 1

Introduction

Cavity Solitons (CS) can give rise to interesting phenomena in photonic systems. These properties can also be useful for applications in optical information processing. In this chapter, we introduce the basic principles on which the work in this thesis is based. We begin with a review of laser operations, including atomic absorption and emission, semiconductor absorption and emission and general laser operations. We introduce semiconductor lasers briefly, before defining a CS and introducing the motivation behind this research.

1.1 Laser operation

In this section, we describe the basics of laser operations in general before introducing the general methods exploited by semiconductor lasers, which are used for the bulk of the research contained within this thesis.

1.1.1 Atomic absorption and emission

We begin with a brief review of quantisation of energy. The quantisation of energy principle states that the electrons in an atom cannot move freely, that they must occupy discreet energy levels. Figure 1.1 shows an example of a simple two level atom. In this example we consider an electron occupying the lowest energy level available, as indicated by the innermost ring. Providing energy to the electron can cause it to jump to a higher energy level, however the energy injected must be equal to the difference in energy between the two levels (i.e. $\Delta E = E_1 - E_0$).

The energy which is injected to excite an electron to a higher energy level can be introduced through different methods. Here we concentrate on introducing this energy through a single photon. A photon of light has an energy governed

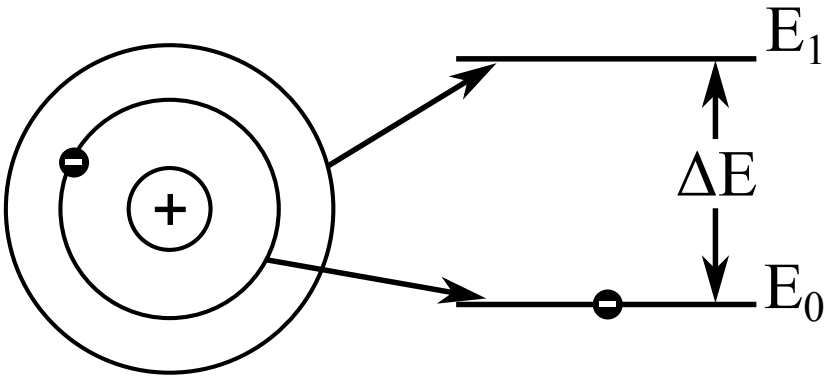

Figure 1.1: An example of the energy levels in the simple case of a two level atom. The nucleus consists of a single proton while a single electron orbits. The rings surrounding the nucleus represent discreet energy levels which the electron can occupy.

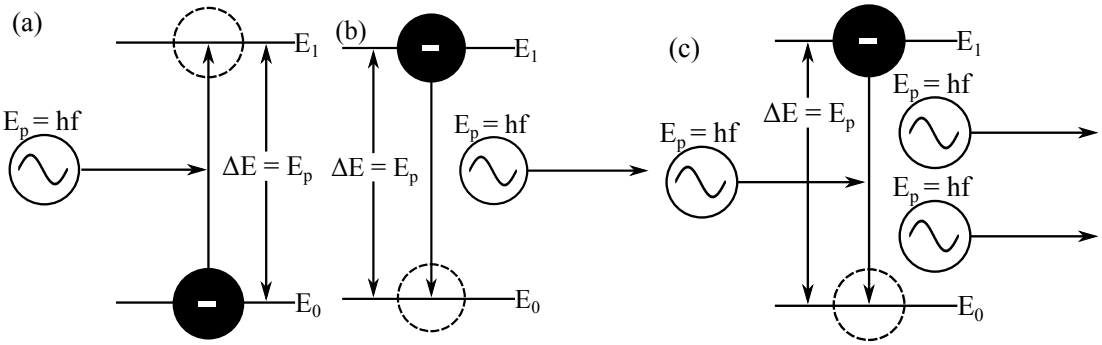

Figure 1.2: Examples of absorption and emission in an atomic model, (a) shows absorption of a photon by an electron and the corresponding jump in energy level, (b) shows spontaneous emission and the corresponding drop in energy of the electron while (c) shows stimulated emission of a photon by an excited electron with the corresponding energy loss of the electron.

by its frequency – $E_p = hf$, where E_p is the energy of the photon, f is the frequency and h is Planck's constant. By utilising a photon with the correct energy (i.e $E_p = \Delta E$), a photon can be absorbed by the electron while exciting it to a higher energy level, as shown in figure 1.2 (a).

Once the energy is stored by the electron, it can be released by one of two methods. The first is spontaneous emission, where the photon is released randomly by the electron's decay to a lower energy level. This has the disadvantage of occurring at a random time and in a random direction (see figure 1.2 (b)), which is not of much use for practical applications (such as lasers).

The final method, which is of particular interest for laser operation, is stimulated emission. This occurs when a photon of energy $E_p = \Delta E$ interacts with an electron which is already excited to a higher energy level. This causes the elec-

tron to decay to the lower energy level, while releasing a photon in the process. This has the advantage of occurring *when* the electron interacts with the photon (i.e. not at some random time) and the photon released by the decaying electron travels in the same direction as the photon which stimulated its release. Figure 1.2 (c) shows an example of this [1, 2].

1.1.2 Laser operations based on a cavity with a two level atomic medium

For laser operation, an optical cavity is generally required. The simplest (and most typical) laser cavity is a Fabry-Perot type cavity, which consists of a reflector at either end enclosing some sort of active medium (see figure 1.3) – in this case a two level atomic medium.

Figure 1.3: An example of a Fabry-Perot type cavity enclosed by a mirror (M) at either end. In this case, the cavity is filled with a two level atomic medium.

The first operation is to create an atomic population inversion. The population inversion is where the electrons of the two level atomic medium are excited from their ground state to an excited state. This is typically achieved by applying a current across the device. As the electrons begin to decay, the photons they release stimulate the decay of electrons in the surrounding atoms causing the release of more photons. As this continues, the photons bounce back and forth between the reflectors causing more photons to be released *via* stimulated emission. This allows for gain in the optical cavity by causing constructive interference of the light. A small amount of light escapes at one of the reflectors and this creates the desired laser beam [2].

1.1.3 Semiconductor absorption and emission

Absorption and emission of photons by semiconductors is, however, more complicated than that described above. When a photon is absorbed by a semiconductor medium, the energy transferred does not cause an electron to jump to a higher energy level as previously described. Rather it creates an *"electron-hole pair."*

This occurs when an electron is excited from the valence band to the conduction band and the electron and the 'hole' it leaves behind are free to travel around the semiconductor lattice, as shown in figure 1.4 (a). When the electron and hole recombine, the energy stored in the system is then released as a photon, as shown in figure 1.4 (b).

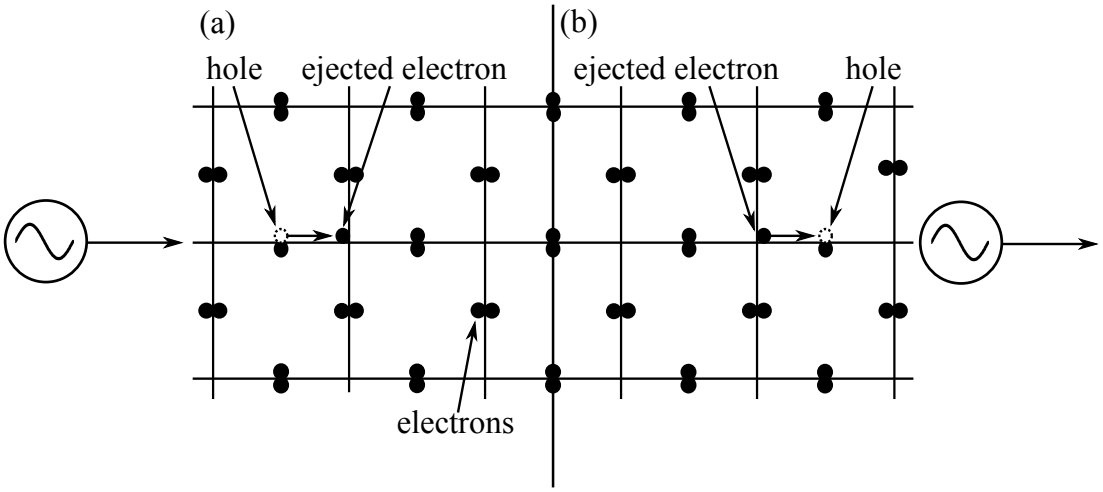

Figure 1.4: An example of absorption and emission in a semiconductor medium. When the photon is absorbed (a), an electron hole pair is created, which can move freely around the semiconductor medium. When they recombine in (b), the energy stored is released as a photon.

This process gives rise to complex effects which can affect the modelling of semiconductor laser systems [2].

1.2 Semiconductor lasers

In this section we introduce some of the different types of semiconductor lasers available. We pay particular attention to the surface emitting lasers, which are used throughout this thesis. Also discussed briefly is the edge emitting laser, which is widely available and used in many everyday products.

1.2.1 Edge emitting semiconductor lasers

The edge emitting semiconductor laser is grown in alternating layers of the desired semiconductor materials. These layers are built up until the device is formed. The active region runs parallel to these layers and the laser beam is emitted parallel to the layers, as shown in figure 1.5. The refractive index of the semiconductor material is such that enough light is reflected (typically 30%) by a plane cleaved

surface, resulting in a laser cavity without the requirement of additional reflectors at each end. Edge emitting semiconductor lasers have been around for some time and are widely used in society.

Figure 1.5: An edge emitting semiconductor laser. The active region is made of layers of semiconductor material and the laser light is emitted parallel to these layers.

1.2.2 Surface emitting semiconductor lasers

Here we introduce surface emitting semiconductor lasers. In a similar method to that used for creating the edge emitting laser, surface emitting semiconductor lasers are grown using alternating layers of the desired semiconductor. In contrast to the edge emitter, however, the laser beam is emitted perpendicular to the semiconductor layers.

Vertical cavity surface emitting laser

The Vertical Cavity Surface Emitting Laser (VCSEL) forms the basis of most of the work compiled in this thesis. A typical VCSEL schematic is shown in figure 1.6. The key challenge facing the VCSEL is that the longitudinal length of the active region is very short compared with other lasers *and* the wavelength of light it is used to produce. The total length of the active region of a VCSEL is typically $1 - 3\lambda$, where λ is the wavelength of the light being produced. This results in less gain as the photons pass fewer electron-hole pairs in the semiconductor layers which provides less stimulated emission than a typical laser.

To overcome this challenge, the reflectors on either side of the active region are replaced with Distributed Bragg Reflectors (DBR). The typical reflectivity of an edge emitting semiconductor laser is approximately 30% of the incident light. While this is sufficient for these lasers, as they have a longer active region and can generate more gain with less passes, they are not for suitable for the VCSEL. The DBRs used with the VCSELs typically reflect approximately 99% of the incident light. Further, the DBRs are also made of layers of semiconductor material. They can therefore be grown directly onto the device. The DBRs works by reflecting some of the light incident on its initial surface and transmitting

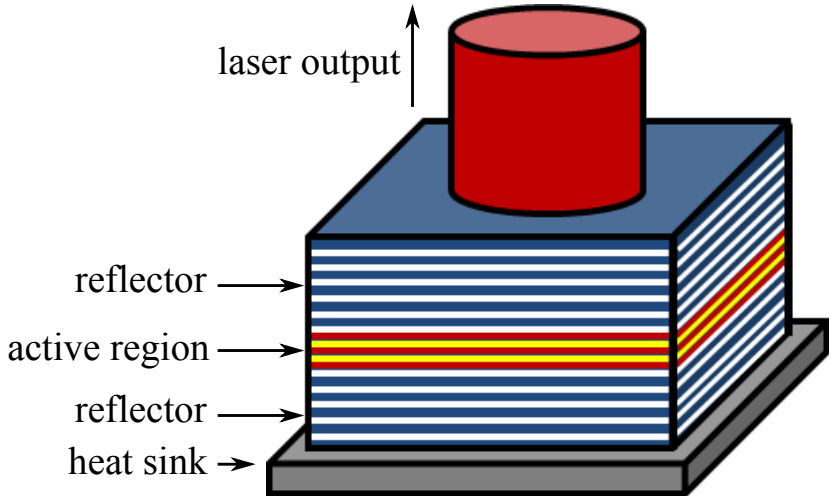

Figure 1.6: Schematic of a typical VCSEL. The active region is sandwiched between reflectors and the light is emitted perpendicular to the semiconductor plane.

some. At the boundary between the layers some more light is reflected and some transmitted. This is achieved by the change in refractive index at the boundaries between semiconductor layers. This process continues until the desired reflectivity is achieved, as shown in figure 1.7.

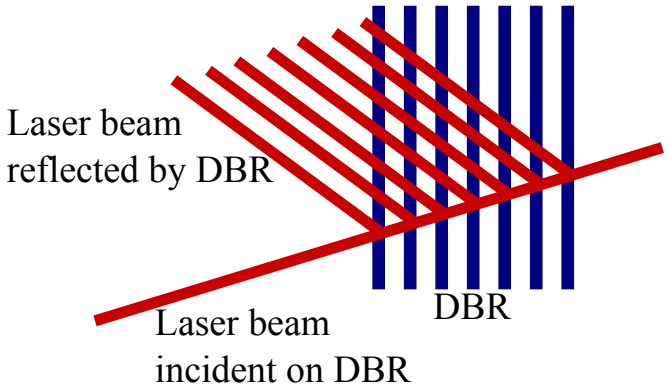

Figure 1.7: The distributed Bragg reflector. The red lines represent the laser light incident on the surfaces and the blue lines represents the boundary between the semiconductor layers making up the DBR.

Using this method allows for greater gain as more of the photons are reflected and therefore spend more time stimulating emissions in the active region.

Vertical external cavity surface emitting laser

The Vertical External Cavity Surface Emitting Laser (VECSEL) is essentially a VCSEL without one of the DBRs, as shown in figure 1.8. In place of the second DBR, an external mirror is used to enclose the optical cavity, extending the cavity

length. This has the advantage of allowing different optical media to be placed within the cavity permitting different effects to be examined. The disadvantage of course comes directly from the use of an external mirror. For this device to function properly, it must be aligned correctly. This is in contrast to the VCSEL which is a complete device and immune from the effects of external influences such as vibrations.

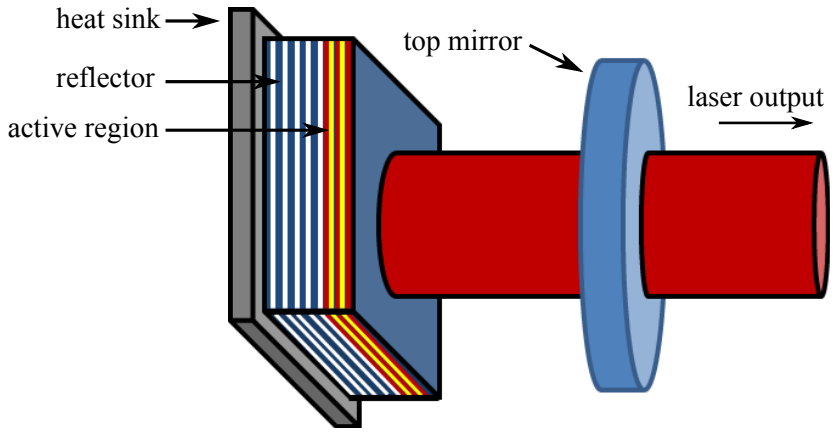

Figure 1.8: Schematic of the VECSEL. Here the top DBR is not included, rather the device is aligned with an external mirror to enclose the optical cavity.

1.3 Nonlinear dynamics of spatio-temporal systems

In this section, we introduce the nonlinear dynamics relevant to the spatio-temporal systems discussed in this thesis. We begin by introducing the saddle-node bifurcation which is at hystersis the base of bistability in hysteresis cycles and specifically the possibility of observing one of two states with the same governing parameters. We then discuss Hopf bifurcations and instabilities leading to oscillatory behaviour. Finally we introduce the Turing instability, which governs the existence of self organising patterns in various media.

1.3.1 Saddle-node bifurcations

Saddle-node bifurcations control the existence and destruction of fixed points in spatio-temporal systems. Consider a control parameter, r. As r is varied, two fixed points move towards each other before colliding. After this collision, if r is varied further, these fixed points annihilate each other. The normal form of a saddle-node bifurcation is:

$$\frac{dx}{dt} = r + x^2 \tag{1.1}$$

The parameter r remains our control parameter and the system is considered to be in a steady state (i.e. $d_t x = 0$). We can clearly see the three states as r changes from a negative to a positive quantity. Where $r < 0$, we obtain $x = \pm\sqrt{r}$ and two fixed points exist in the system. As r approaches $r = 0$, we obtain $x = 0$ and the two fixed points collide forming a singular, marginally stable fixed point. Finally, for $r > 0$ we find that $x = \sqrt{-r}$ and therefore the fixed points have vanished. Figure 1.9 shows the differences between these three states [3].

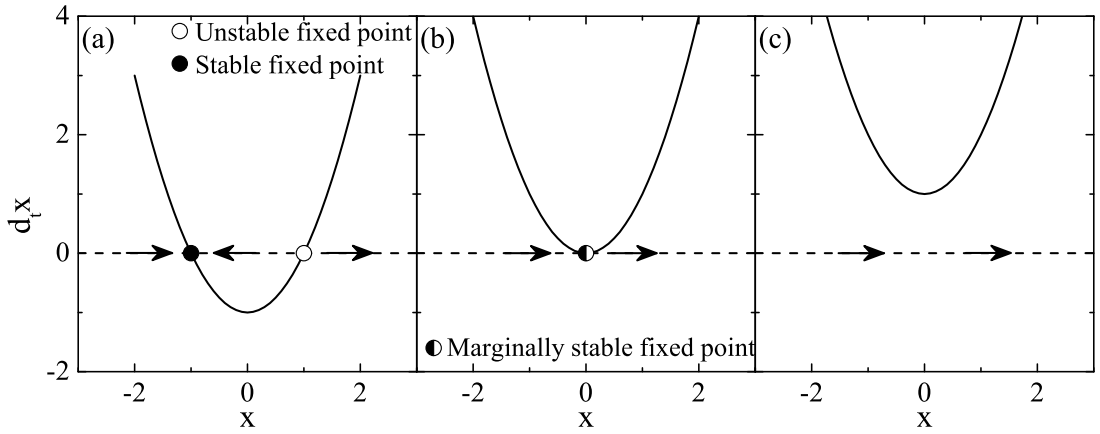

Figure 1.9: Saddle node bifurcation upon variations of a control parameter (r). In (a), $r < 0$ and two fixed points exist, in (b) $r = 0$ and the two fixed points have collided. Finally, (c) shows $r > 0$ and the two fixed points have annihilated each other.

There are several methods for plotting saddle-node bifurcations, the most conventional of which is to plot x as a function of r. This is shown in figure 1.10 (a) for equation (1.1) (left side) and for $d_t x = r - x^2$ (right side). The reasoning behind this type of bifurcation diagram is that r takes the form of an independent variable and should therefore be plotted on the horizontal axis [3]. A combination of two saddle-node bifurcations can be used to describe bistability in a hysteresis cycle. Figure 1.10 (b) shows a bistable region by combining (slight variations of) those shown in the bifurcation diagram of figure 1.10 (a). Here, the central branch is unstable and forms a separatrix between the upper and lower curve in the bistable region.

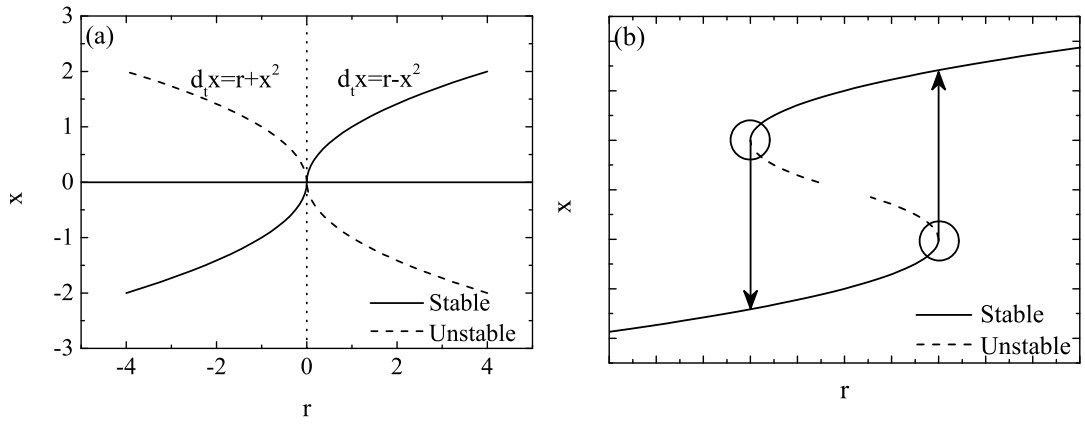

Figure 1.10: Panel (a) shows a bifurcation diagram for two cases, separated by the vertical dotted line. Stable solutions are represented by a solid line while unstable solutions are represented by a dashed line. Panel (b) shows bistability approximated by a pair of saddle-node bifurcations. The centre branch is unstable (dashed line) while the upper and lower branches are both stable (solid line). Bistability exists in the region between the two arrows.

1.3.2 Hopf bifurcations

The results for the saddle-node bifurcation can be generalised to n-dimensional systems, provided the Jacobian matrix has n distinct eigenvalues. Bifurcations occur when either a real eigenvector is zero or when two complex conjugate eigenvectors have a real part equal to zero. If only one real eigenvalue becomes positive, we have a saddle-node bifurcation (or other one dimensional bifurcations such as a transcritical or pitchfork bifurcation). However if the real part of two complex conjugate eigenvalues becomes positive, we have a Hopf bifurcation.

If we examine a two dimensional system which has a stable fixed point, the eigenvalues (λ_1, λ_2) of the Jacobian must both lie in the left half of the plane, i.e. $\mathrm{Re}\,\lambda < 0$. Since the eigenvalues satisfy a quadratic equation with real coefficients, there are two possible scenarios. Either the eigenvalues are both real and negative (figure 1.11 (a)) or they are complex conjugates (1.11 (b)). To destabilise the fixed point, we require that one or both eigenvalues cross into the right half of the plane (i.e. $\lambda > 0$) [3].

Supercritical Hopf bifurcation

For the purpose of this discussion, we will restrict ourselves to two dimensions however Hopf bifurcations can occur in phase spaces of any dimension $n \geq 2$. We begin by considering a system that relaxes to an equilibrium state through exponentially damped oscillations. This means small perturbations decay back to the

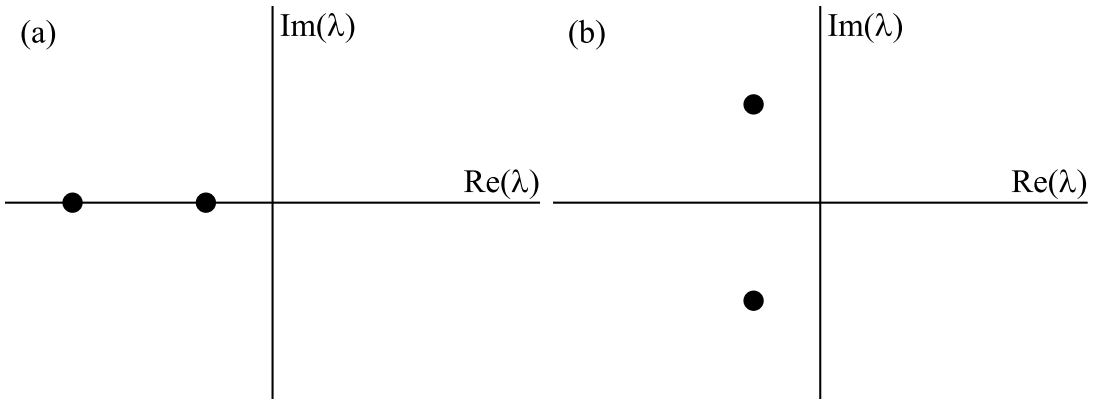

Figure 1.11: Example of the eigenvalues of the Jacobian matrix of a two dimensional system. In (a) the eigenvalues are real and negative while in (b) the eigenvalues are complex conjugates of each other with negative real parts.

equilibrium state through these oscillations. If the decay rate of the oscillations depends on some control parameter, μ, and the decay becomes slower as μ is varied before changing to growth at a critical value of the control parameter, μ_c, then the equilibrium state will lose stability when μ passes through μ_c. In many of these cases, this results in a small amplitude, sinusoidal oscillation around the former equilibrium point. Such systems are described as having undergone a supercritical Hopf bifurcation [3].

As a simple example of a supercritical Hopf bifurcation, we consider the following equations:

$$\begin{aligned} \frac{\partial r}{\partial t} &= \mu r - r^3 \\ \frac{\partial \theta}{\partial t} &= \omega + br^2. \end{aligned} \tag{1.2}$$

Here we introduce three parameters, μ controls the stability of the fixed point at the origin, ω is the frequency of the oscillations and b controls the dependence of frequency on amplitude when considering larger oscillations. When $\mu < 0$, the origin $r = 0$ is a stable spiral while the direction of rotation is controlled by the sign of ω. When $\mu = 0$, the origin remains a stable spiral however it becomes very weak. Finally for $\mu > 0$, where there is an unstable spiral at the origin and a stable, circular limit cycle with $r = \sqrt{\mu}$.

To examine the behaviour of the eigenvalues during the bifurcation, we con-

sider equations (1.2) in Cartesian coordinates:

$$\begin{aligned}\frac{\partial x}{\partial t} &= \mu x - \omega y + \text{cubic terms} \\ \frac{\partial y}{\partial t} &= \omega x + \mu y + \text{cubic terms.}\end{aligned} \tag{1.3}$$

From this, we can extract the Jacobian matrix at the origin:

$$A = \begin{pmatrix} \mu & -\omega \\ \omega & \mu \end{pmatrix} \tag{1.4}$$

which has the eigenvalues $\lambda = \mu \pm i\omega$. As expected, the eigenvalues cross the imaginary axis from left to right as μ increases from negative to positive values [3].

Of course, this example is that of an ideal case and as such has properties which are not completely accurate when examining a physical system. Firstly, the Hopf bifurcations encountered in practice have a limit cycle which is elliptical (not circular as with our example) and its shape becomes distorted as μ moves away from the bifurcation point. Secondly, in our example, the eigenvalues move horizontally as μ is increased, i.e. $\operatorname{Im}\lambda$ is independent of μ. In practice, the eigenvalues follow a curve and cross the imaginary axis with a non-zero gradient.

Subcritical Hopf bifurcation

The subcritical Hopf bifurcation is much more dramatic (and potentially dangerous in engineering applications) than its supercritical counterpart. With a subcritical Hopf bifurcation, we find that the trajectories must jump to a distant attractor, which may be a fixed point, another limit cycle, infinity or (in three or more dimensions) a chaotic attractor. Again, we limit ourselves to the two dimensional case although interesting results, such as the *Lorenz attractor* which demonstrates chaotic attractors, can be observed in three or more dimensions. We consider the example:

$$\begin{aligned}\frac{\partial r}{\partial t} &= \mu r + r^3 - r^5 \\ \frac{\partial \theta}{\partial t} &= \omega + br^2\end{aligned} \tag{1.5}$$

The important difference in this example is that the cubic term, r^3, becomes destabilising and helps to drive trajectories away from the origin. In this example, we again consider μ which controls the stability of the fixed point, ω is the

frequency of the oscillation and b determines the dependance of frequency on amplitude.

The phase portraits are shown in figure 1.12 and show two distinct cases. When $\mu < 0$, we observe two attractors – a stable limit cycle and a fixed point at the origin. Between these two stable attractors lies an unstable cycle (shown as the dashed circle in figure 1.12 (a)). As μ increases from negative to positive values, this unstable cycle shrinks around the fixed point, until it has zero amplitude, creating an unstable fixed point at the origin as $\mu = 0$. For $\mu > 0$, the stable limit cycle becomes the only attractor and as a result, the only stable solution.

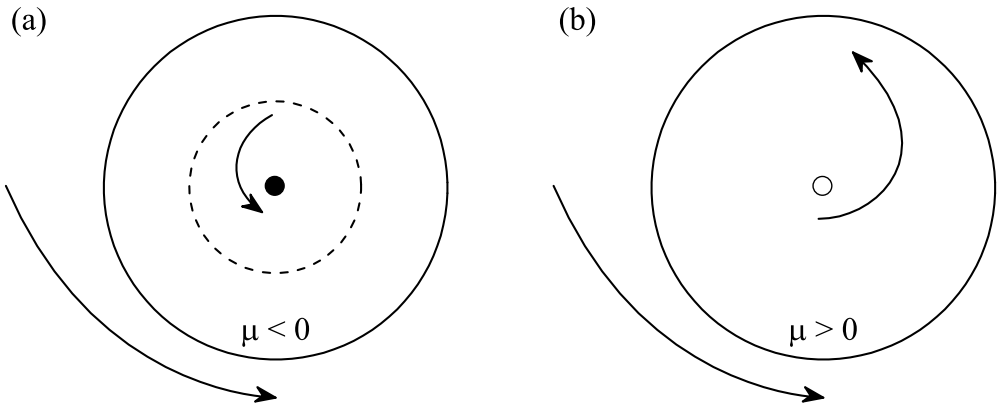

Figure 1.12: Example of a subcritical Hopf bifurcation. In (a) there is an attractive fixed point at the origin and an attractive limit cycle separated by an unstable cycle (dashed circle), for $\mu < 0$. In (b) the unstable cycle has shrunk around the origin, resulting in the limit cycle existing as the only stable attractor ($\mu > 0$.

It is important to note that this system exhibits hysteresis. Once the stable fixed point at the origin becomes unstable and solutions which used to remain near the centre are forced towards the attractive limit cycle, these solutions will not return towards the origin simply by returning μ left of the imaginary axis. The large oscillations will remain until such time that μ is decreased to a point stable and unstable cycles collide in a bifurcation known as a saddle-node bifurcation of cycles [3].

Subcritical Hopf bifurcations occur in a number of dynamical systems such as nerve cells [4], aeroelastic flutter and other vibrations of aeroplane wings [5, 6] and in instabilities of fluid flows [7].

1.3.3 Turing instabilities

Since the pioneering work of Alan Turing on chemical morphogenesis [8], it has become clear that two species diffusing at different rates and competing with each other within the same environment can spontaneously break the translational invariance (discretely) leading to the formation of regular (and irregular) spatial patterns. Although the Turing instability can be studied in linearized systems (see [9]), nonlinearity is necessary to saturate the growth of the unstable mode of the pattern. Above the Turing instability a variety of geometrical structures (stripes, squares, rhomboids, hexagons, honeycombs, etc.) can form in a 2D space, their relative stability depending on the details of the given equations and nonlinear terms. Here we examine the Turing instabilities leading to pattern formation in the presence of diffusion and diffraction, the main mechanism for spatial coupling in chemistry and photonics, respectively.

In his seminal paper on chemical morphogenesis in 1952, Alan Turing showed that the translational invariance of a homogenous solution can spontaneously break in systems with competing species (an activator and an inhibitor) with separate diffusion rates [8]. An excellent review and expansion of Turing's work is provided in [10]. Here we use a simplified 'linearized' model of the Turing instability in 1D as discussed in [9]:

$$\begin{aligned} \frac{\partial R}{\partial t} &= \alpha R - \beta I + D_1 \partial_x^2 R \\ \frac{\partial I}{\partial T} &= \gamma R - \delta I + D_2 \partial_X^2 I \end{aligned} \tag{1.6}$$

where the parameters α, β, γ , δ and the diffusion rates D_1 and D_2 are real and positive quantities. Since R (I) displays linear growth (decay), it is identified as the activator (inhibitor) variable of the two diffusing species. The homogeneous solution $R = I = 0$ is unstable to a spatially modulated perturbation of wavevector $k_c = 2\pi/\Lambda_c$ with

$$k_c^2 = \left(\frac{2\pi}{\Lambda_c}\right)^2 = \frac{1}{2}\left[\frac{\alpha}{D_1} - \frac{\delta}{D_2}\right] \tag{1.7}$$

if and only if

$$\frac{D_2}{D_1} > \frac{\delta}{\alpha} \tag{1.8}$$

Since there are no nonlinear terms in equation (1.6), the amplitude of the Turing pattern (i.e. a spatially periodic solution with wavelength Λ_c) grows in-

definitely. The main role of the nonlinear terms is in fact to counterbalance such linear growth via saturation (see [9, 10]).

In 2D the Turing instability does not prescribe a given geometry provided that the spatial periodicity is $\Lambda_c = 2\pi/k_c$. Several geometries can tile the 2D plane: stripes, squares, rhomboids, hexagons, honeycombs, etc. The saturating nonlinear terms do not affect the simultaneous existence of the separate geometries but only their relative stability. We can now summarize the necessary features of an instability leading to Turing patterns as follows [10]:

1. a clear activator-inhibitor linear dynamics and

2. specific conditions on the spatial coupling mechanism allowing or forbidding pattern formation.

Early links between Turing and optical patterns were made in a seminal paper by Lugiato and Lefever [11]. Clear activator-inhibitor dynamics, however, were not established. It was later shown that this was possible for photonic systems which display 'off-resonance' mechanism for the formation of stationary patterns. 'Off-resonance' pattern formation corresponds to the generation of periodic spatial structures whose spatial modulation is inversely proportional to the square root of the detuning between the material and cavity resonances. As an example of a photonic system which displays 'off-resonance' pattern formation, we consider the Degenerate Optical Parametric Oscillator (DOPO) [12] in the specific configuration of a nonresonated pump field. For simplicity and for comparison with that describe above for chemical systems, we restrict ourselves to one transverse spatial dimension. These results do not change for the two transverse spatial dimension case.

The equation for the electric field, E, takes the form of a Parametrically Forced Ginzburg-Landau (PFGL) equation:

$$\frac{\partial E}{\partial \tau} = QE^* - (1 + i\Delta)E - E|E|^2 + ia\partial_x^2 E \tag{1.9}$$

where Q is the real amplitude of the input pump and Δ is the detuning between the signal frequency and the closest cavity mode. By introducing the real (R) and imaginary (I) part of the signal field E, equation 1.9 becomes:

$$\begin{aligned} \frac{\partial R}{\partial t} &= (Q-1)R + \Delta I - a\partial_X^2 I - R(R^2 + I^2) \\ \frac{\partial I}{\partial t} &= -\Delta R - (1+Q)I + a(\partial_x^2 R - I(R^2 + I^2). \end{aligned} \tag{1.10}$$

The nonlinear terms of the PFGL equation have a purely saturating role for both R and I. In order to characterise the linear onset of the instability, we neglect them ($|R|$, $|I| \ll 0$). When setting the diffraction coefficient to zero ($a = 0$), the linear term structure of equation (1.10) exactly reproduces that of equation 1.6 with zero diffusion rates, under the identification of $\alpha = Q1$, $\beta = \gamma = \Delta$, $\delta = Q + 1$. In the DOPO system, then, the real (imaginary) part of the complex electric field plays the role of the activator (inhibitor). This is condition (1) of the Turing instability as established previously. Since we want to find out if DOPO spatial periodic structures belong to the same class of universality of Turing patterns, we study equation 1.10 with no nonlinear terms and with generic diffraction coefficients a1 and a2:

$$\begin{aligned} \frac{\partial R}{\partial t} &= \alpha R - \beta I - a_1 \partial_x^2 I \\ \frac{\partial I}{\partial t} &= \gamma R - \delta I + a_2 \partial_x^2 R. \end{aligned} \tag{1.11}$$

Following the method described in [10], the linear stability analysis of the homogeneous state gives:

$$\begin{aligned} 0 &= \lambda^2 + \lambda(\delta - \alpha) + h(k^2) \\ h(k^2) &= a_1 a_2 k^4 - k^2(a_1\gamma + a_2\beta) + \gamma\beta - \delta\alpha \end{aligned} \tag{1.12}$$

where λ are the stability eigenvalues. It is easy to find that the wavevector k corresponding to the minimum stability value is

$$k_c^2 = \left(\frac{2\pi}{\Lambda}\right)^2 = \frac{1}{2}\left[\frac{\beta}{a_1} + \frac{\gamma}{a_2}\right] \tag{1.13}$$

Pattern formation is certainly inhibited when both a_1 and a_2 are negative. The presence of a region in the (a_1, a_2) plane where pattern formation is forbidden satisfies condition (2) of the Turing instability as described above. In the specific case of the DOPO, $a = a_1 = a_2$ and $\beta = \gamma = \Delta$, resulting in $k_c^2 = -\Delta/a$ which is the typical condition of 'off-resonance' pattern formation (we recall that Δ is the cavity-medium detuning). We can then conclude that the 'off-resonance' mechanism leading to pattern formation in DOPO and saturable absorbers is a Turing instability and that the stationary and spatially periodic structures observed in these photonic systems are Turing patterns [13].

Finally it is important to note that pattern formation and Turing patterns are essential to the existence of spatial solitons. Solitons exist in a medium where

there is bistability between the spatially homogeneous state and the patterned state. In other words, in the desired system, the ability to observe a homogeneous state *and* a patterned state for fixed values of the parameters give rise to the formation of self-localised structures and spatial solitons.

1.4 Conservative and dissipative solitons

The soliton is a solitary wave that does not change as it propagates. It is formed by a balance of linear and nonlinear effects in the medium of propagation. Solitons were first observed in a canal near Edinburgh, Scotland by J. S. Russell in 1834 and were first described as the 'wave of translation.' Included here is Russell's description of this 'wave of translation,' as published in [14]:

"I believe I shall best introduce this phenomenon by describing the circumstances of my own first acquaintance with it. I was observing the motion of a boat which was rapidly drawn along a narrow channel by a pair of horses, when the boat suddenly stopped–not so the mass of water in the channel which it had put in motion; it accumulated round the prow of the vessel in a state of violent agitation, then suddenly leaving it behind, rolled forward with great velocity, assuming the form of a large solitary elevation, a rounded, smooth and well-defined heap of water, which continued its course along the channel apparently without change of form or diminution of speed. I followed it on horseback, and overtook it still rolling on at a rate of some eight or nine miles an hour, preserving its original figure some thirty feet long and a foot to a foot and a half in height. Its height gradually diminished, and after a chase of one or two miles I lost it in the windings of the channel. Such, in the month of August 1834, was my first chance interview with that singular and beautiful phenomenon which I have called the Wave of Translation, a name which it now very generally bears."

Russell later recreated his 'wave of translation' in a water tank. He determined that this was a fundamental mode of propagation, as an arbitrary 'heap' of water would disintegrate almost immediately and resolve itself into a primary and residual wave. His work allowed the realisation that the velocity was proportional to its height and proposed the law $c^2 = g(h + \eta)$, where g represents gravity, h is the undisturbed depth of the water and η is the maximum height of the wave, measured from the undisturbed level of the water [15].

However Russell's discovery and work was not received well by the scientific community. Questions were raised by Airy and Stokes as to whether a wave which travelled without change in shape could exist totally above water, attributing the

loss of amplitude as a sign that the wave was nonpermanent. Russell refuted these claims suggesting friction was the cause of the loss of amplitude, which turned out to be correct. Russell's work was to be finally accepted in the 1870's, when (independently) Boussinesq [16] (1872) and Rayleigh (1876) found the hyperbolic sec squared solution for the free surface. Finally, in 1895, Korteweg and deVries wrote down the equation describing waves in shallow water surfaces, independently of the work performed by both Boussinesq and Rayleigh [15].

Solitons fall into one of two broad categories. They can be either *conservative* or *dissipative*. We now attempt to define these and describe the difference between them before introducing cavity solitons, a type of spatial dissipative soliton, which are the focus of this thesis. For this purpose we consider only optical solitons, however the effects described have analogues to solitons in other media, such as water or plasma.

1.4.1 Conservative solitons

Conservative solitons, as the name suggests, are solitary waves whose energy is conserved. In other words, there is no energy lost from the system and no energy input to the system. They exist with a balance of linear (diffraction or dispersion) and nonlinear (e.g. optical Kerr effect) effects in the medium of propagation. The Kerr effect states that, in a nonlinear medium, the refractive index becomes proportional not only to the frequency of the photons passing through the medium but also to the intensity of the photons, i.e. $n = n_0 + n_2|E|^2$ where n is the refractive index, n_0 is the linear refractive index, n_2 is the optical Kerr coefficient and E is the electric field [17].

The interaction (and collisions) of conservative solitons are of particular interest. Indeed two conservative solitons which travel towards each other will pass straight through each other and emerge unaffected by the collision (with the possible exception of a phase shift). There is no transfer of momentum or energy between the two solitons during the collision. This brings us to the criteria which a conservative soliton must satisfy [18]:

1. The soliton must maintain its shape when it moves at constant velocity.

2. When a soliton interacts with another soliton, it must emerge from the collision unchanged with the possible exception of a phase shift.

1.4.2 Dissipative and cavity solitons

Dissipative solitons, in contrast to conservative solitons, exist in systems which have dissipations, i.e. systems which have a loss of energy. To counter the energy losses, a constant energy input is required. An excellent example of dissipative optical solitons are those which exist in laser systems. At the laser output there is a constant loss of energy as some of the photons exit the laser cavity. Energy input to counter the loss of energy can take many forms. In this thesis, for example, we examine systems with optical injection where a second (master) laser is used to drive the system. Dissipative solitons are formed with a balance of linear and nonlinear effects, however the energy losses of the system must also be balanced by the energy input to the system.

Of particular interest are dissipative solitons in optical cavities, which have become known as Cavity Solitons (CS). CS share many properties of spatial solitons, for example diffraction is balanced with nonlinear effects in the cavity. It is important to note that CS are not simply solitons 'in a box.' They require an optical cavity to exist and such optical cavities are essential to their survival. The balance between nonlinear and linear effects required for the existence of CS exists within the optical cavity, therefore if the cavity is removed, the soliton ceases to exist.

For CS to exist, there has to a balance of forces acting on the excitation. Firstly, the spatial components must balance. Therefore the nonlinear self-focusing that exists in the cavity must balance diffraction effects, which try and spread the CS (see figure 1.13 (a)). Secondly, we require a balance between the dissipative effects (losses at the cavity reflectors) and gain, as shown in figure 1.13 (b) [19].

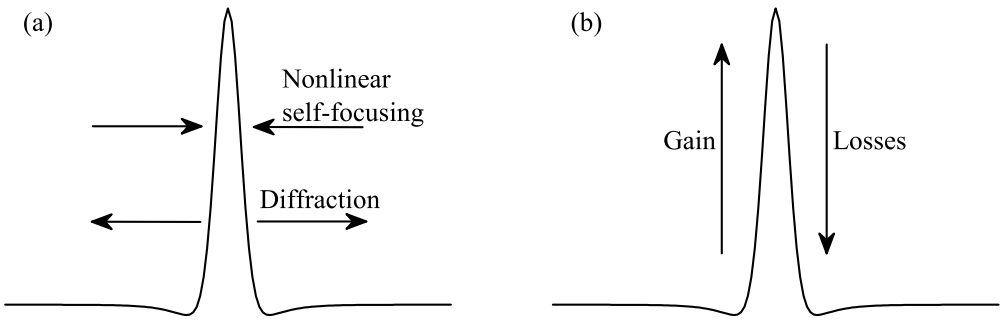

Figure 1.13: Example of a CS profile. In (a) self-focusing is shown balancing diffraction while (b) shows losses balancing gain.

At this point, we will define the criteria required for a localised structure to be considered a CS. These important points will be revisited in some of the later chapters:

1. The localised structure(s) must be bistable with the (quasi-) homogeneous background.

2. The localised structure(s) should be optically controllable.

3. Each localised structure should be independently controllable.

From point 1, the CS should be bistable with the background state. Therefore, an operator of the system should be able to write and erase the CS as they please. Point 2 stipulates that the CS should be optically controllable. The position of the CS can be adjusted by introducing optical gradients to induce motion. Finally, the CS should be individually controllable, i.e an operator should be able to switch individual CS on or off and move them using optical gradients without affecting any other CS that may have been created in the system. Note that the CS *can* interact with each other, which does not affect this final point – chapter 5 examines the effects of collisions between CS, amongst other things.

A further point to note about CS is that their dynamics are non-Newtonian. This fact is particularly useful for applications as the velocity of a CS is proportional to the applied optical gradient, in contrast to Newtonian dynamics which dictate the acceleration is proportional to the applied gradient [19].

Laser Cavity Solitons (LCS) are a further type of spatial dissipative soliton examined in this thesis. The main difference between a CS and a LCS is the freedom of an LCS to choose its own frequency and phase. CS typically exist in driven systems, where an external holding beam is required to inject energy into the system. This has the consequence of locking the frequency and phase of the CS to that of the holding beam. LCS exist in systems which do not require a holding beam to inject energy. In these systems, as there is no holding beam, the frequency and phase remain free. LCS can be considered "*micro-lasers*" in an active device with a large transverse area.

1.5 Motivation

Here we introduce some of the motivation behind the research contained within this thesis. The motivations described here are practical applications which the CS researched in this thesis may prove useful for in the future.

1.5.1 All-optical delay line

The all-optical delay line was presented in [20] for a laser with injection operating in a passive configuration and in [21], operating in an active configuration. Information can currently be transmitted along optical fibres, and such fibres can provide for much faster transmission rates than are currently available. Future networks will require information to be routed or stored optically, however such routing will require the ability to buffer data when the optical router is busy with another data stream.

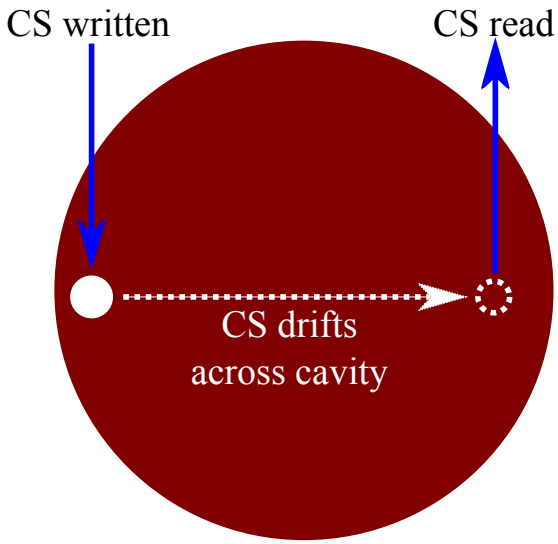

Figure 1.14: An example of an all optical delay line based on CS. The CS can be written at one point and travel on an optical gradient to a second location where the result is read.

An all-optical delay line based on CS is ideal for this purpose. CS can be created at one end of the delay line where they can travel across the transverse plane of the cavity to a second location where they can be read and subsequently erased, as shown in figure 1.14. Where a CS is received at the output a binary '1' would be read while an absence of a CS would represent a binary '0'. Further, the delay can be controlled by varying the optical gradient on which the CS finds itself [20, 21].

1.5.2 Optical memories

Optical memories could play an important part in future optical networks or even optical computers. The ability to store information as light could prove very useful. Here we highlight that CS can be used to create arrays of information. Again, we consider a CS at a specific location to represent a binary '1' and the

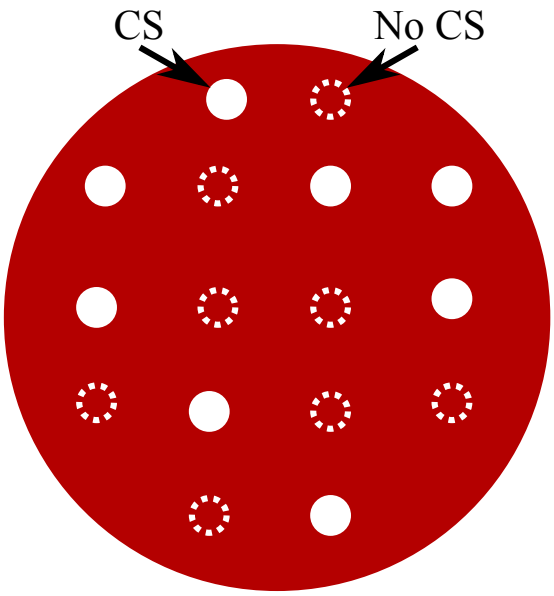

Figure 1.15: An example of an optical memory based on CS. A message can be stored as an array of CS and can be modified or erased as desired.

absence of a CS to represent a binary '0'. The ability to write and erase individual CS as desired makes them an ideal candidate for the task of optical memories. A message can be stored as a sequence of CS and can be modified or erased completely, as desired (see figure 1.15) [22].

1.6 Outline of the thesis

This thesis is organised as follows. We begin by introducing the theory and models which are required throughout. Chapter 2 derives the Maxwell-Bloch equations relevant for the studies using the VCSEL, before introducing the appropriate models for a laser with optical injection and a laser with Frequency Selective Feedback (FSF). For both these systems, we introduce some key parameters and define the range of these, over which we can expect to encounter CS. Further, for the laser with FSF, we discuss the benefits of our model over the more traditional Lang-Kobyashi approximation. This chapter concludes by introducing a simple Kerr cavity model which is also used throughout this thesis.

Chapter 3 introduces the process of writing and erasing CS in the relevant models. We begin with a general introduction to the literature on writing, before applying the writing process in our models. Chapter 4 introduces motion into our models by using phase gradients and detuning gradients, where appropriate. Chapter 5 introduces CS interactions in our models. We examine not only collisions of two or more CS but also introduce pinning defects to examine the effect

two CS have on each other in our laser with FSF. Finally, chapter 6 introduces oscillations in our model of a laser with FSF before the general conclusions in chapter 7.

Chapter 2

Theory and models of photonic devices displaying cavity solitons

2.1 Introduction

This chapter introduces the key background theory for the modelling of Cavity Solitons (CS) in photonic devices. We begin by deriving the Maxwell-Bloch equations relevant to this thesis. For this, we start by introducing Maxwell's equations, with a description of the slowly varying wave approximation. The optical Bloch equations for a two level atom follows, where we introduce the decay terms before combining Maxwell's equations with the optical Bloch equations.

After this derivation, the appropriate models are introduced. For each model, a diagram of the experimental setup is included, along with a discussion of the key parameters. For the laser with Frequency Selective Feedback (FSF), we also discuss the benefits of our model over more conventional techniques for modelling feedback. We finish with a description of the key numerical methods used to integrate the model equations. These methods allow for the successful integration of the device equations used for our models.

2.2 Maxwell-Bloch equations for lasers

2.2.1 Maxwell's Equations

We start with Maxwell's equations in a non-magnetic medium with no free charges and no free currents:

$$\begin{aligned} \nabla \cdot \tilde{\mathbf{D}} &= 0 & \nabla \cdot \tilde{\mathbf{B}} &= 0 \\ \nabla \times \tilde{\mathbf{E}} &= -\frac{\partial \tilde{\mathbf{B}}}{\partial t} & \nabla \times \tilde{\mathbf{B}} &= \mu_0 \frac{\partial \tilde{\mathbf{D}}}{\partial t} \\ \tilde{\mathbf{D}} &= \varepsilon_0 \tilde{\mathbf{E}} + \tilde{\mathbf{P}} \end{aligned} \tag{2.1}$$

where $\tilde{\mathbf{D}}$ and $\tilde{\mathbf{B}}$ are the electric and magnetic flux densities, $\tilde{\mathbf{E}}$ is the electric field, $\tilde{\mathbf{P}}$ is the medium polarisation, ε_0 and μ_0 the permittivity and permeability of vacuum. By taking the curl of the third Maxwell's equation one gets

$$\nabla \times \nabla \times \tilde{\mathbf{E}} = -\frac{\partial(\nabla \times \tilde{\mathbf{B}})}{\partial t} = -\mu_0 \frac{\partial^2 \tilde{\mathbf{D}}}{\partial t^2} = -\mu_0 \frac{\partial^2 (\varepsilon_0 \tilde{\mathbf{E}} + \tilde{\mathbf{P}})}{\partial t^2}$$

i.e.

$$\nabla \times \nabla \times \tilde{\mathbf{E}} + \frac{1}{c^2} \frac{\partial^2 \tilde{\mathbf{E}}}{\partial t^2} = -\frac{1}{\varepsilon_0 c^2} \frac{\partial^2 \tilde{\mathbf{P}}}{\partial t^2}$$

where $c = (\mu_0 \varepsilon_0)^{-1/2}$ is the speed of light in the vacuum. By using the vector calculus equality

$$\nabla \times \nabla \times \tilde{\mathbf{E}} = \nabla(\nabla \cdot \tilde{\mathbf{E}}) - \nabla^2 \tilde{\mathbf{E}}$$

and considering that the directional derivative (first term in the r.h.s) is zero for plane waves and negligibly small in the slowly varying amplitude approximation (see later), one obtains:

$$-\nabla^2 \tilde{\mathbf{E}} + \frac{1}{c^2} \frac{\partial^2 \tilde{\mathbf{E}}}{\partial t^2} = -\frac{1}{\varepsilon_0 c^2} \frac{\partial^2 \tilde{\mathbf{P}}}{\partial t^2} \,.$$

Note also that the magnitude of $\tilde{\mathbf{P}}$ is much smaller than that of $\tilde{\mathbf{E}}$ so that the first Maxwell's equation gives $\nabla \cdot \tilde{\mathbf{D}} \approx \nabla \cdot \tilde{\mathbf{E}} \approx 0$ in agreement with the approximation made above. We consider now a wave that propagates in the vacuum with frequency ω and wave-vector k such that $k = \omega/c$. Such wave impinges on our medium along the z direction. By introducing the slowly varying complex

amplitudes E and P via:

$$\tilde{\mathbf{E}} = \left[Ee^{-i(kz-\omega t)} + c.c.\right]\vec{z} \qquad \tilde{\mathbf{P}} = \left[Pe^{-i(kz-\omega t)} + c.c.\right]\vec{z}$$

where $c.c.$ is the complex conjugate, one obtains:

$$\begin{aligned} &-\nabla_\perp^2 E - \left[\frac{\partial^2 E}{\partial z^2} - 2ik\frac{\partial E}{\partial z} - k^2 E\right] + \frac{1}{c^2}\left[\frac{\partial^2 E}{\partial t^2} + 2i\omega\frac{\partial E}{\partial t} - \omega^2 E\right] \\ &= -\frac{1}{\varepsilon_0 c^2}\left[\frac{\partial^2 P}{\partial t^2} + 2i\omega\frac{\partial P}{\partial t} - \omega^2 P\right] \end{aligned}$$

where $\nabla_\perp^2$ is the Laplacian operator in the plane perpendicular to the direction of propagation $\vec{z}$.

Slowly Varying Amplitude Approximation

Since we are dealing with frequencies and wavelengths in the optical domain

$$\left|\frac{\partial^2 E}{\partial t^2}\right| \ll \omega\left|\frac{\partial E}{\partial t}\right| \qquad \left|\frac{\partial^2 E}{\partial z^2}\right| \ll k\left|\frac{\partial E}{\partial z}\right| \qquad \left|\frac{\partial^2 P}{\partial t^2}\right| \ll \omega\left|\frac{\partial P}{\partial t}\right|$$

are very well satisfied. The slowly varying amplitude approximation leads to:

$$-\nabla_\perp^2 E + 2ik\left[\frac{\partial E}{\partial z} + \frac{1}{c}\frac{\partial(E + P/\varepsilon_0)}{\partial t}\right] = \frac{\omega^2}{\varepsilon_0 c^2}P \tag{2.2}$$

where we have used the vacuum dispersion relation $k = \omega/c$. Note that for a medium with a linear response

$$P = \varepsilon_0 \chi^{(1)} E$$

where $\chi^{(1)}$ is the linear susceptibility, the wave equation becomes

$$-\nabla_\perp^2 E + 2i\left[k\frac{\partial E}{\partial z} + \frac{\omega(1+\chi^{(1)})}{c^2}\frac{\partial E}{\partial t}\right] + \left(k^2 - \frac{\omega^2}{c^2}\right)E = \frac{\chi^{(1)}\omega^2}{c^2}E\,.$$

The dispersion relation in the medium now becomes:

$$k^2 = (1+\chi^{(1)})\frac{\omega^2}{c^2} = \frac{n^2\omega^2}{c^2}$$

where we have defined the refractive index as $n = \sqrt{1+\chi^{(1)}}$. Under this definition the wave equation in a linear medium becomes:

$$-\nabla_{\perp}^2 E + 2i\left[k\frac{\partial E}{\partial z} + \frac{ck(1+\chi^{(1)})}{nc^2}\frac{\partial E}{\partial t}\right] = -\nabla_{\perp}^2 E + 2ik\left[\frac{\partial E}{\partial z} + \frac{n}{c}\frac{\partial E}{\partial t}\right] = 0\,. \tag{2.3}$$

2.2.2 The Optical Bloch Equations

To describe the wave propagating in the medium we consider atoms with two energy levels and appropriate wavefunctions

$$\begin{aligned} H_0|1> &= E_1|1> & H_0|2> &= E_2|2> \\ <1|1> &= <2|2> = 1 & <1|2> &= <2|1> = 0 \end{aligned}$$

where the first two equations are the time independent Schrödinger equations for the two energy levels separated by the energy $\hbar\omega_A$ while the third and fourth are the orthonormality conditions of the wavefunctions. We introduce the raising $|2><1|$ and lowering $|1><2|$ operators and express the Hamiltonian H_0 and the interaction Hamiltonian H_I as

$$\begin{aligned} H_0 &= E_1|1><1| + E_2|2><2| \\ H_I &= \hbar\left(g|1><2|e^{i\omega t} + g^*|2><1|e^{-i\omega t}\right) \end{aligned}$$

where ω is the frequency of the incoming laser beam while g is the Rabi frequency defined as:

$$g = E_0\frac{e}{2\hbar}\int <1|D_{E_0}|2>\, d\vec{r} = \frac{\mu_{12}}{2\hbar}E_0 \tag{2.4}$$

with E_0 being the amplitude of the incident beam, D_{E_0} is the component of the electric atomic dipole in the beam direction and μ_{12} is the magnitude of the electric dipole moment provided by the appropriate matrix element in (2.4). The time dependent Schrödinger equation for the full system is:

$$\begin{aligned} i\hbar\frac{\partial}{\partial t}|\Psi_s> &= (H_0 + H_I)\,|\Psi_s> \\ &= \left[E_1|1><1| + E_2|2><2| + \hbar\left(g|1><2|e^{i\omega t} + g^*|2><1|e^{-i\omega t}\right)\right]|\Psi_s> \end{aligned} \tag{2.5}$$

where $|\Psi_s>$ is the system wavefunction in the Schrödinger representation. It is then convenient to move into the interaction representation via the transforma-

tion:

$$|\Psi>= e^{iH_0 t/\hbar}|\Psi_s>$$

where the time dependent Schrödinger equation takes the convenient form

$$i\hbar\frac{\partial}{\partial t}|\Psi>= H_I|\Psi>= \hbar\left(g|1><2|e^{i\Delta t}+g^*|2><1|e^{-i\Delta t}\right)|\Psi>$$

where $\Delta=\omega-\omega_A$ is the field-atom frequency detuning and H_I is now in the interaction representation. We can finally introduce the density matrix $\rho=|\Psi><\Psi|$ and rewrite the Schrödinger equation as:

$$\frac{\partial}{\partial t}\rho=-\frac{i}{\hbar}[H_I,\rho]$$

where $[\cdot,\cdot]$ is the commutator.

The decay terms: the Lindblad form

The interaction of the system with the environment (including the vacuum) is described by a coupling with a heat bath in the Markov (short memory) approximation. It is then possible to obtain decay terms for the dynamics of the density matrix in the Lindblad form

$$\begin{aligned}\frac{\partial}{\partial t}\rho=&-\frac{i}{\hbar}[H_I,\rho]+\sum_{ij}q_{ij}|j><i|\rho|i><j|-\frac{1}{2}\sum_{ij}q_{ij}|i><i|\rho\\&-\frac{1}{2}\rho\sum_{ij}q_{ij}|i><i|\end{aligned}$$

where i,j take the values $1,2$ and q_{ij} are numbers that specify the decays due to the coupling with the external heat bath. For our medium formed by two-level atoms the specific form of the Bloch equations is:

$$\begin{aligned}\frac{d\rho_{11}}{dt}&=-i\left(g^*\rho_{21}e^{i\Delta t}-g\rho_{12}e^{-i\Delta t}\right)+q_{21}\rho_{22}\\\frac{d\rho_{12}}{dt}&=-ig^*\left(\rho_{22}-\rho_{11}\right)e^{i\Delta t}-\frac{1}{2}\left(q_{11}+q_{21}+q_{22}\right)\rho_{12}\\\frac{d\rho_{21}}{dt}&=-ig\left(\rho_{11}-\rho_{22}\right)e^{-i\Delta t}-\frac{1}{2}\left(q_{11}+q_{21}+q_{22}\right)\rho_{21}\\\frac{d\rho_{22}}{dt}&=-i\left(g\rho_{12}e^{-i\Delta t}-g^*\rho_{21}e^{i\Delta t}\right)-q_{21}\rho_{22}\,.\end{aligned}$$

It is convenient to remove the explicit dependence of the Bloch equation from time by introducing the variables $R_{ii} = \rho_{ii}$ and

$$R_{12} = \rho_{12} e^{i\Delta t} \qquad R_{21} = \rho_{21} e^{-i\Delta t}$$

to obtain

$$\begin{aligned}
\frac{dR_{11}}{dt} &= -i\left(g^* R_{21} - g R_{12}\right) + q_{21} R_{22} \\
\frac{dR_{12}}{dt} &= -ig^*\left(R_{22} - R_{11}\right) - \left[\frac{1}{2}\left(q_{11} + q_{21} + q_{22}\right) + i\Delta\right] R_{12} \\
\frac{dR_{21}}{dt} &= -ig\left(R_{11} - R_{22}\right) - \left[\frac{1}{2}\left(q_{11} + q_{21} + q_{22}\right) - i\Delta\right] R_{21} \\
\frac{dR_{22}}{dt} &= -i\left(g R_{12} - g^* R_{21}\right) - q_{21} R_{22}\,.
\end{aligned}$$

We consider that no other energy levels are involved in the dynamics so that the sum of the probabilities of occupancy of level 1 and level 2 is certainty, i.e. one. This translates into $\rho_{11} + \rho_{22} = R_{11} + R_{22} = 1$ and makes the system non-homogeneous. We can reduce the number of relevant equations by considering the population inversion variable $n = \rho_{22} - \rho_{11} = R_{22} - R_{11}$. A further reduction comes from the fact that the off diagonal terms are the complex conjugate of each other. The Bloch equations are then reduced to:

$$\begin{aligned}
\frac{dR_{21}}{dt} &= -\left(\gamma_\perp - i\Delta\right) R_{21} + igN \\
\frac{dn}{dt} &= -\gamma_\parallel (n+1) - 2i(gR_{21}^* - g^* R_{21})
\end{aligned}$$

where we have introduced the traditional decay rates

$$\gamma_\perp = \frac{1}{2}\left(q_{11} + q_{21} + q_{22}\right) \qquad \gamma_\parallel = q_{21}\,.$$

Note that $\gamma_\perp \geq \gamma_\parallel/2$. The equation for N shows that with no incident field there is no population inversion since N relaxes to -1 (all atoms in the ground state). In a laser, however, the equilibrium state is in a population inversion state with $n = 1$ due to the pumping:

$$\frac{dR_{21}}{dt} = -\left(\gamma_\perp - i\Delta\right) R_{21} + igN \tag{2.6a}$$

$$\frac{dn}{dt} = -\gamma_\parallel (n-1) + 2i(g^* R_{21} - gR_{21}^*)\,. \tag{2.6b}$$

The combination of Bloch and Maxwell's equations.

We introduce now new macroscopic variables in equations (2.6) connected to the complex amplitudes E and P of the propagation Maxwell's equation (2.2):

$$N = n_a n \qquad P = n_a \mu_{12} R_{21} e^{-ikz} \qquad E = E_0 e^{-ikz}$$

to obtain:

$$\begin{aligned}
\frac{\partial E}{\partial z} + \frac{1}{c}\frac{\partial (E + P/\varepsilon_0)}{\partial t} &= -\frac{i}{2k}\nabla_\perp^2 E - \frac{i\omega^2}{2k\varepsilon_0 c^2} P \\
\frac{\partial P}{\partial t} &= \gamma_\perp \left[-(1 - i\Delta) P + \frac{i\mu_{12}^2}{2\hbar\gamma_\perp} EN \right] \\
\frac{\partial N}{\partial t} &= -\gamma_\parallel \left[N - n_a + \frac{i}{\hbar\gamma_\parallel}(E^* P - E P^*) \right]
\end{aligned}$$

where we have normalised the detuning Δ by $\gamma_\perp$ to make it adimensional. To follow the literature we rewrite these equations for the complex conjugate field $F = E^*$ and conjugate polarisation $Q = P^*$:

$$\begin{aligned}
\frac{\partial F}{\partial z} + \frac{1}{c}\frac{\partial (F + Q/\varepsilon_0)}{\partial t} &= \frac{i}{2k}\nabla_\perp^2 F + \frac{ik}{2\varepsilon_0} Q \\
\frac{\partial Q}{\partial t} &= \gamma_\perp \left[-(1 + i\Delta) Q - \frac{i\mu_{12}^2}{2\hbar\gamma_\perp} FN \right] \\
\frac{\partial N}{\partial t} &= -\gamma_\parallel \left[N - n_a - \frac{i}{\hbar\gamma_\parallel}(F Q^* - F^* Q) \right] .
\end{aligned}$$

A final normalization of the variables

$$E = \frac{\mu_{12}}{\hbar\sqrt{\gamma_\parallel \gamma_\perp}} F \qquad P = \frac{2i}{\mu_{12} n_a}\sqrt{\frac{\gamma_\perp}{\gamma_\parallel}} Q \qquad D = \frac{N}{n_a}$$

casts the equations in the standard Maxwell-Bloch form:

$$\frac{\partial E}{\partial z} + \frac{1}{c}\frac{\partial (E - 2i\alpha P/k)}{\partial t} = \frac{i}{2k}\nabla_\perp^2 E + \alpha P \tag{2.7a}$$

$$\frac{\partial P}{\partial t} = \gamma_\perp \left[-(1 + i\Delta) P + ED \right] \tag{2.7b}$$

$$\frac{\partial D}{\partial t} = -\gamma_\parallel \left[D - 1 + \frac{1}{2}(E P^* + E^* P) \right] \tag{2.7c}$$

where:

$$\alpha = \frac{\mu_{12}^2 n_a k}{4\hbar\varepsilon_0 \gamma_\perp} .$$

Finally, by considering the variables αP and αD one obtains:

$$\frac{\partial E}{\partial z} + \frac{1}{c}\frac{\partial (E - 2iP/k)}{\partial t} = \frac{i}{2k}\nabla_{\perp}^{2} E + P \tag{2.8a}$$

$$\frac{\partial P}{\partial t} = \gamma_{\perp}\left[-\left(1 + i\Delta\right)P + ED\right] \tag{2.8b}$$

$$\frac{\partial D}{\partial t} = -\gamma_{\parallel}\left[D - \alpha + \frac{1}{2}(EP^{*} + E^{*}P)\right]. \tag{2.8c}$$

Equations (2.8a-2.8c) are the Maxwell-Bloch equations for a laser based on a two-level atom model as derived by L. Lugiato and L.M. Narducci in [23] apart from the polarisation term in the l.h.s. of equation (2.8a). We note that in the case of an absorbing medium, the sign of P and D is reversed and that upon reversing the equilibrium value of the population variable in the absence of an incident field, one obtains exactly the equations given by A. Scroggie in his PhD thesis [24].

2.2.3 Mean Field Limit

The Maxwell-Bloch equations derived above, describe the propagation of an electromagnetic wave in a two-level medium prepared in a state of population inversion, within the slowly varying amplitude approximation. We now extend these equations to the case of a medium of length L in a ring optical cavity of length $\mathcal{L}$. For clarity we focus our attention on the field equation (2.7) since the mean field limit introduces conditions on the parameter α:

$$\frac{\partial E}{\partial z} + \frac{n}{c}\frac{\partial E}{\partial t} = \frac{i}{2k}\nabla_{\perp}^{2} E + \alpha P \tag{2.9}$$

where in the l.h.s. we have considered the first order (linear) contribution of the polarisation to the wave speed through the refractive index as described in (2.3). We set $z = 0$ at the entrance of the crystal and write the longitudinal boundary condition as

$$E(x, y, 0, t) = e^{\mathcal{D}}\, E\left(x, y, L, t - \frac{\mathcal{L} - L}{c}\right) + \sqrt{T} E_{IN}(x, y) \tag{2.10a}$$

$$\mathcal{D} = ln\sqrt{R_j} - i\delta_j + (\mathcal{L} - L)\frac{i}{2k}\nabla_{\perp}^{2} \tag{2.10b}$$

$$\delta = \frac{\omega_c - \omega}{c}\mathcal{L} \qquad T = 1 - R, \tag{2.10c}$$

where $R(T)$ is the mirror reflectivity (transmittivity), for the field, E_{IN} is the input field (if any) at frequency ω, while ω_c is the frequency of the longitudinal

cavity mode closest to ω. In the following we will use the transmittivity of the output mirror as a small parameter, i.e.

$$\sqrt{T} = \varepsilon \ll 1 \,.$$

In order to force the boundary condition (2.10) into the propagation equation (2.9), the usual Mean Field Limit (MFL) transformation is entered

$$z' = z \tag{2.11a}$$

$$t' = t + \left[\frac{\mathcal{L} - L}{c}\right] \frac{z}{L} \,. \tag{2.11b}$$

Under the condition (2.11), we obtain

$$\partial_z = \partial_{z'} + \left[\frac{\mathcal{L} - L}{cL}\right] \partial_{t'} \qquad \partial_t = \partial_{t'}$$

$$\partial_z + \frac{n}{c}\, \partial_t = \partial_{z'} + \left[\frac{\mathcal{L} - L}{cL}\right] \partial_{t'} + \frac{n}{c}\, \partial_{t'} = \partial_{z'} + \left[\frac{\mathcal{L} + (n-1)L}{cL}\right]\, \partial_{t'} \,.$$

Note that the usual MFL transformation of the time variable leaves a refractive index dependence in the coefficient of $\partial_{t'}$; we will see its consequences later.

By introducing the new field variable F such that

$$F = \Gamma E + \sqrt{T} E_{IN} \frac{z}{L} \quad \text{with} \quad \Gamma = \exp\left(\mathcal{D}\frac{z}{L}\right)$$

we obtain

$$\begin{aligned}
&\partial_{t'} F + \frac{cL}{\mathcal{L} + (n-1)L} \quad \partial_{z'} F \\
&\quad = \frac{cL}{\mathcal{L} + (n-1)L} \left[\frac{\mathcal{D}}{L}\left(F - \sqrt{T} E_{IN} \frac{z}{L}\right) + \Gamma\left(\partial_z E + \frac{n}{c}\, \partial_t E\right) + \sqrt{T} E_{IN} \frac{1}{L}\right] \\
&\quad = \frac{cL}{\mathcal{L} + (n-1)L} \left[\frac{\mathcal{D}}{L}\left(F - \sqrt{T} E_{IN} \frac{z}{L}\right) + \Gamma\left(\frac{i}{2k}\nabla_\perp^2 E + \alpha P\right)\right. \\
&\quad \left. + \sqrt{T} E_{IN} \frac{1}{L}\right] .
\end{aligned}$$

The longitudinal boundary conditions (2.10) are now transformed into

$$F(x, y, 0, t') = F(x, y, L, t') \tag{2.12}$$

i.e. the field is periodic at the same time t'. The standard MFL conditions are

$$\begin{aligned} &\varepsilon \ll 1; && \delta = O(\varepsilon) \ll 1; \\ &\alpha = O(\varepsilon) \ll 1; && (\mathcal{L} - L)/2k = O(\varepsilon) \ll 1 \end{aligned}$$

one obtains:

$$\mathcal{D} \approx -\frac{T}{2} - i\delta + i\frac{\mathcal{L} - L}{2k}\nabla_\perp^2 \qquad \Gamma \approx 1 + \frac{\mathcal{D}}{L}z$$

since

$$\ln\sqrt{R} = \ln\sqrt{1-T} \approx \ln\left(1 - \frac{T}{2}\right) \approx -\frac{T}{2}\,.$$

At the first order in ε one gets:

$$\begin{aligned} &\partial_{t'}F + \frac{cL}{\mathcal{L} + (n-1)L}\ \partial_{z'}F \\ &\quad = -\frac{c\,T/2}{\mathcal{L} + (n-1)L}\ F - i\frac{c\,\delta}{\mathcal{L} + (n-1)L}\ F + i\frac{c\mathcal{L}}{2k[\mathcal{L} + (n-1)L]}\nabla_\perp^2 F \\ &\quad + \frac{c\,\sqrt{T}}{\mathcal{L} + (n-1)L}\ E_{IN} + \frac{c\,L}{\mathcal{L} + (n-1)L}\ \alpha P. \end{aligned}$$

By introducing the new convenient parameters

$$\tau = \frac{\mathcal{L} + (n-1)L}{c}; \qquad \gamma = \frac{T}{2}; \qquad a = \frac{\mathcal{L}}{2k}\,,$$

one obtains:

$$\tau\ \partial_{t'}F + L\ \partial_{z'}F = -\gamma F - i\delta F + ia\nabla_\perp^2 F + \alpha L P + \sqrt{2\gamma}E_{IN}\,.$$

Since the new longitudinal boundary condition (2.12) is now synchronous and periodic, one can use an expansion in longitudinal Fourier modes. Under the MFL conditions, however, only the longitudinal mode closest to ω has components different from zero. This mode corresponds to a zero longitudinal frequency so that $\partial_{z'}F = 0$ so that we finally obtain:

$$\begin{aligned} \tau\ \partial_{t'}F &= -\gamma F - i\delta F + ia\nabla_\perp^2 F + \alpha L P + \sqrt{2\gamma}E_{IN} \\ \partial_{t'}F &= \kappa\left[-(1+i\theta)F + i\hat{a}\nabla_\perp^2 F + \mu P + E_I\right] \end{aligned}$$

where

$$\kappa = \frac{\gamma}{\tau} = \frac{\gamma c}{\mathcal{L} + (n-1)L}$$
$$\theta = \frac{\delta}{\gamma} = \frac{(\omega_c - \omega)\mathcal{L}}{c\gamma}$$
$$\hat{a} = \frac{a}{\gamma} = \frac{\mathcal{L}}{2k\gamma}$$
$$\mu = \frac{\alpha L}{\gamma} = \frac{\mu_{12}^2 n_a k L}{4\hbar\varepsilon_0\gamma_\perp\gamma}$$
$$E_I = \sqrt{\frac{2E_{IN}}{\gamma}}$$

Going now back to the Maxwell-Bloch equations (2.8a-2.8c) after $P = \mu P$ and $D = \mu D$ we obtain

$$\frac{\partial E}{\partial t} = \kappa\left[E_I + P - (1 + i\theta)E + i\nabla^2 E\right] \tag{2.13a}$$
$$\frac{\partial P}{\partial t} = \gamma_\perp\left[ED - (1 + i\Delta)\,P\right] \tag{2.13b}$$
$$\frac{\partial D}{\partial t} = \gamma_\parallel\left[\mu - D - \frac{1}{2}(EP^* + E^*P)\right] \tag{2.13c}$$

where we have normalised the spatial variables x, y by dividing them by $\sqrt{\hat{a}}$.

2.3 Semiconductor laser with injected signal.

In this section, the experimental setup and model equations for a laser with optical injection are introduced. Here, a Vertical Cavity Surface Emitting Laser (VCSEL) is used. We also examine the key parameters of the model to define the region where stable CS are located.

2.3.1 Experimental setup

The experimental setup of a VCSEL with optical injection is shown in figure 2.1. The beam from the master laser is split by a beam splitter, with the first branch providing the holding beam and the second being used to create the localised addressing beam. These two branches are recombined and injected into the VCSEL [25].

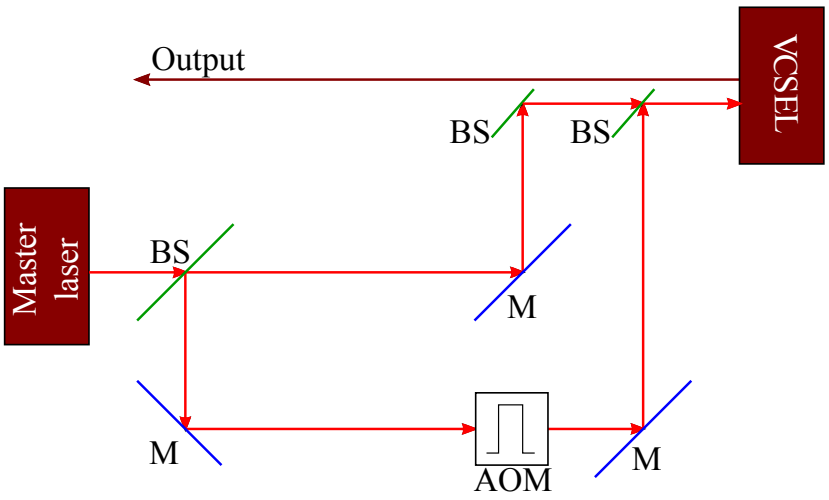

Figure 2.1: The experimental setup of a VCSEL with optical injection. VCSEL is a vertical cavity surface emitting laser, BS are the beam splitters, M are the mirrors and AOM is an acousto-optic modulator used to create the localised addressing beam.

2.3.2 Theoretical model

The theoretical model, also described in [25], is introduced here. This model, based on the Maxwell-Bloch equations derived in section 2.2, includes a dynamical variable for the polarisation. This is important as, above the lasing threshold, the model can produce unphysical results without such term.

To begin, the equation for the polarisation must be modified to include the peculiar behaviour of the susceptibility (and gain) in semiconductor lasers. In [26] for example equations (2.13) are modified into:

$$\frac{\partial E}{\partial t} = \varepsilon \left[E_I + P - (1 + i\theta)E + i\nabla^2 E \right] \tag{2.14a}$$

$$\frac{\partial P}{\partial t} = \xi(D) \left[(1 - i\alpha)ED - P \right] \tag{2.14b}$$

$$\frac{\partial D}{\partial t} = \gamma \left[J - D - \frac{1}{2}(EP^* + E^*P) \right] \tag{2.14c}$$

where α is the renown linewidth enhancement factor, $\varepsilon = \kappa/\gamma_\perp$, $\gamma = \gamma_\parallel/\gamma_\perp$ and

$$\xi(D) = \Gamma(D)(1 - i\alpha) + i\delta(D) \tag{2.15a}$$

$$\Gamma(D) = 0.276 + 1.016D \qquad \delta(D) = 0.169 + 0.216D \tag{2.15b}$$

where $\delta(D)$ representing the detuning between the reference frequency and the peak of the gain curve, E and P are the dynamical cavity field and polarisation terms respectively, E_I is the optical injection, θ is the detuning between the

injection and VCSEL fields, $ia\nabla^2 E$ is diffraction with a the diffraction parameter, ξ is the susceptibility of the semiconductor material, D is the carrier distribution, J is the pump current and $d\nabla^2 D$ is the carrier diffusion with d the diffusion coefficient. Note that the value of this coefficient is such that diffusion effects are negligible and henceforth ignored ($d = 0.052$) [25].

Further ε is the is the decay rate of the field and γ is the decay rate of the carriers. Time is scaled to the dephasing rate, τ_d, of the microscopic dipoles and the decay rates are defined as $\varepsilon = \tau_d/\tau_p$ and $\gamma = \tau_d/\tau_c$, where τ_p and τ_c are the photon lifetime and carrier recombination time respectively.

2.3.3 Homogeneous stationary solutions and bistability conditions

From [26], the dynamical equations (2.14) admit the plane wave stationary solution $E = E_S$, $P = P_S$ and $D = D_S$. Introducing $x = |E_S|^2$ and $y = |E_I|^2$ the equation that links the output intensity x to the input intensity y is

$$y = x\left[\left(1 - \frac{J}{1+x}\right)^2 + \left(\theta + \frac{\alpha J}{1+x}\right)^2\right]. \tag{2.16}$$

The shape of the stationary curve depends on the parameters J, α and θ. The stationary curve can be bistable, with a negative slope branch that extends between the two turning points x_A and x_B. Figure 2.2 shows the bistability domains in the plane (x, θ) for $\alpha = 3.0$ and different values of the pump parameter J. The intersections of the bistability domain with the horizontal line corresponding to a certain value of θ give the turning points x_A and x_B for that value of θ. All the x values between the turning points belong to the negative slope branch.

The equation for the boundaries of the bistability region is:

$$\theta_{\pm}(x, \alpha, \theta) = -\frac{J\alpha \pm \sqrt{J^2x^2\left(1+\alpha^2\right) - \left[(1+x)^2 - J\right]^2}}{(1+x)^2} \tag{2.17}$$

so that one can derive the exact expression for coordinates (x_C, θ_C) of the rightmost point of bistability domain:

$$x_C = -1 + \frac{J\sqrt{1+\alpha^2} + \sqrt{J\left[J\left(1+\alpha^2\right) - 4\left(\sqrt{1+\alpha^2} - 1\right)\right]}}{2} \tag{2.18a}$$

$$\theta_C = -\frac{J\alpha}{(1+x_C)^2} \tag{2.18b}$$

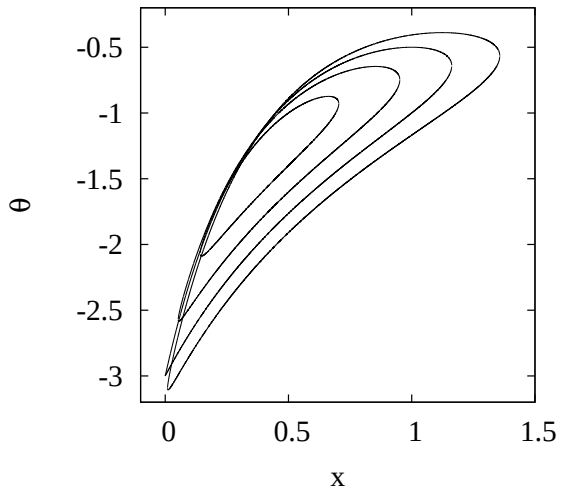

Figure 2.2: Bistability domain for $\alpha = 3$. From the larger to the smaller domain J takes the values of 1.05, 1.00, 0.95 and 0.90.

Clearly, bistability is possible only if x_C is real and positive, and this sets a lower limit to the pump parameter

$$J_{min} = 4\frac{\sqrt{1+\alpha^2}-1}{1+\alpha^2} \tag{2.19}$$

For $J = J_{min}$ the bistability domain shrinks to the point of coordinates $x' = 1 - 2/\sqrt{1+\alpha^2}$ (positive only for $\alpha > \sqrt{3}$) and $\theta' = -(\sqrt{1+\alpha^2}+1)/\alpha$. For $\alpha = 3.0$ we have $J_{min} = 0.8649$, $x' = 0.3675$ and $\theta' = -1.387$.

If the VCSEL is close to threshold ($J \approx 1$) and $\alpha > \sqrt{3}$, approximated expressions can also be found for the lower and upper extrema θ_{min} and θ_{max} of the bistability domain:

$$\theta_{min}(\alpha, J) \approx -\alpha - \frac{\alpha^2+1}{\alpha \pm \sqrt{3}}(J-1) \tag{2.20a}$$

$$\theta_{max}(\alpha, J) \approx \frac{(\alpha^2-9)^2 - 108}{8\alpha^3} + \frac{(\alpha^2+9)^2(\alpha^2+1)}{8\alpha^3(\alpha^2-3)}(J-1) \tag{2.20b}$$

In equations (2.20) the upper (lower) sign holds for $J > 1$ ($J < 1$). For $J = 1$ we have exactly $\theta_{min} = -\alpha$. In general, θ must be negative and smaller in absolute value than α in order to have bistability. In our model $\varepsilon(\theta + \alpha)$ represents the frequency of plane wave emission for the solitary laser, while the zero frequency is that of the injected field. The fact that bistability requires $\theta + \alpha > 0$ means that the injected field must be red detuned with respect to the solitary laser.

2.3.4 Turing instability

We now study the stability of the homogeneous solution against perturbations of the form $\delta X \exp(\lambda\tau + i\mathbf{K}\cdot\mathbf{x})$, with $X = E, P, D$. Two types of instability are possible. Here we examine the first of these, the Turing instability ($\mathrm{Re}(\lambda) > 0$ and $\mathrm{Im}(\lambda) = 0$) [13, 26].

In the absence of carrier diffusion ($d = 0$), an analytic expression of the stability eigenvalues can be found

$$\lambda_{\pm} = -\left[1 - \frac{J}{(1+x)^2}\right] \pm \sqrt{\frac{J^2x^2\left(1+\alpha^2\right)}{(1+x)^4} - \left[K^2 + \theta + \frac{J\alpha}{(1+x)^2}\right]^2} \tag{2.21}$$

The positive eigenvalue is responsible for the instability and the spatial wavevector K_{max} that maximizes it is given by

$$K_{max}^2 = -\frac{J\alpha}{(1+x)^2} - \theta \tag{2.22}$$

The boundaries of the Turing instability domain in the plane (x, K^2) are

$$K_{T\pm}^2 = \theta_{\pm}(x, \alpha, J) - \theta \tag{2.23}$$

where the values of $\theta_{\pm}$ are given by equation (2.17). The instability domain is therefore simply the bistability domain shifted vertically by an amount $-\theta$, and it crosses the axis $K = 0$ in correspondence with the turning points x_A and x_B of the stationary curve. This is related to the fact that the negative slope branch is unstable even in the plane wave limit ($K = 0$). Equation (2.23) shows that a variation of θ simply causes a rigid translation of the instability domain in the vertical direction. In this translation the position of the turning points x_A and x_B varies but the right extremum x_C of the instability domain remains unchanged. Hence, by varying θ we can vary the extension of the unstable part of the upper branch. In order to have bistability and instability on the upper branch it must be $\theta_{min} < \theta < \theta_C$ with θ_{min} given by (2.20a) and x_C and θ_C given by (2.18). An example of the Turning instability domain is shown in figure 2.3 for $J = 1.05$, $\alpha = 3.0$ and $\theta = -2.3$. The upper branch of the stationary curve is Turing unstable from the turning point x_B to x_C [26].

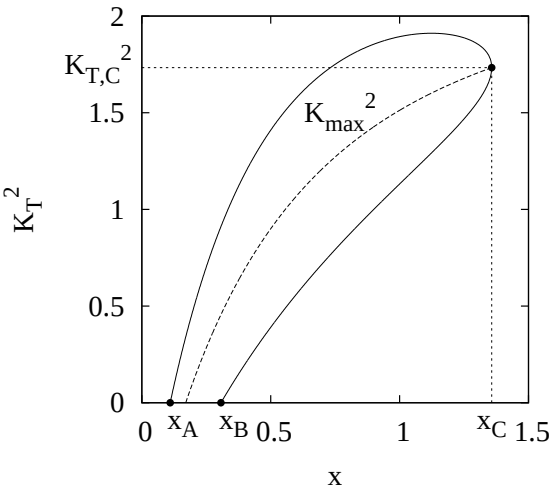

Figure 2.3: Turing instability domain for $J = 1.05$, $\alpha = 3.0$, $\theta = -2.3$ and $d = 0$. The dashed line is the wavevector that maximises the unstable eigenvalue according to equation (2.22)

2.3.5 Hopf instability

The second type of instability is the Hopf instability ($\mathrm{Re}(\lambda) > 0$ and $\mathrm{Im}(\lambda) \neq 0$). The Hopf instability is the region before the slave laser, in this case the VCSEL, locks its frequency and phase to that of the master laser (i.e. the optical injection) [3, 26]. A simple expression for the boundary of the instability domain can be obtained by neglecting terms of order γ:

$$\begin{aligned} \varepsilon K_{H\pm}^2 = {} & \delta_S \left(2 - D_S\right) + \alpha\Gamma_S \left(D_S - 1\right) + \varepsilon \left(\frac{\delta_S D_S}{\Gamma_S} - \theta - \alpha D_S\right) \\ & \pm \left(\Gamma_S + \varepsilon\right) \sqrt{\left(D_S\right)\left(\alpha^2 D_S + 1 - \frac{2\alpha D_S \delta_S}{\Gamma_S}\right) + \left(\frac{D_S \delta_S}{\Gamma_S}\right)^2} \end{aligned} \tag{2.24}$$

where $\Gamma_S = \Gamma(D_S)$, $\delta_S = \delta(D_S)$ and $D_S = J/(1 + x)$ is the stationary value of D in the homogeneous solution. The instability domain (both exact and the approximated one) is shown in figure 2.4, for $J = 1.05$, $\alpha = 3.0$, $\theta = -2.3$, and $\varepsilon = 0.04$.

The homogeneous solution is unstable up to the injection locking point, which is $x \approx J - 1$, ($D_S \approx 1$). This has a clear physical meaning. As stated above, the solitary laser and the injected field oscillate at different frequencies, $\varepsilon(\theta+\alpha)$ and 0, respectively. The two frequencies compete giving rise to an oscillatory behaviour as long as the injected field is not strong enough to impose its frequency. This happens when the intensity of the driven laser equates that of the solitary laser, i.e. when $x \approx J - 1$.

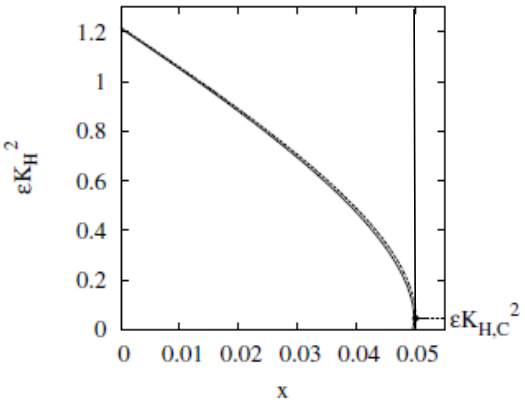

Figure 2.4: Hopf instability domain for $J = 1.05$, $\alpha = 3.0$, $\theta = -2.3$ and $\varepsilon = 0.04$. The solid line represents the exact boundary, the dashed line is the approximated expression given by equation (2.24).

This picture remains valid even in the plane wave limit ($K = 0$). The inclusion of diffraction modifies it under two respects. First, the critical transverse wavevector $K_{H,C}$, which can be obtained from equation (2.24) setting the square root equal to zero and approximating D_S with 1, is given by:

$$\varepsilon K_{H,C}^2 \approx \delta(1) - \varepsilon\,(\alpha + \theta) \tag{2.25}$$

This result can be interpreted considering that $\delta(1)$ is the peak of the gain curve for $D_S = 1$ and $\varepsilon(\alpha + \theta)$ is the frequency of the solitary laser when it emits on-axis. Hence the right hand member of the above equation is an effective "atomic" detuning Δ, and the equation expresses the well-known result that for positive Δ the tilted wave with $K = \sqrt{\Delta/\varepsilon}$ has maximum gain. The second analytic result that can be obtained from equation (2.24) concerns the bandwidth of the unstable transverse wavevectors, which is maximum for $x = 0$, where it is given approximately by:

$$\varepsilon K_H^2(0) \approx \Gamma(J)\left[\sqrt{(\alpha^2 J + 1)\,(J - 1)} + \alpha\,(J - 1)\right] \tag{2.26}$$

The results of the stationary homogeneous solution and its stability are summarised in figure 2.5 which shows the homogeneous stationary curve for $J = 1.05$, $\alpha = 3.0$ and $\theta = -2.3$ as a function of y. The lower branch is Hopf unstable up to the injection locking point. The negative slope branch is unstable as usual. The upper branch is unstable from the upper turning point to the critical point which is beyond the right margin of the figure. The part of the lower branch from the injection locking point to the lower turning point, however, is stable. Stationary

CS with stable backgrounds exist in that region, and their peak intensity is also shown in figure 2.5 [26].

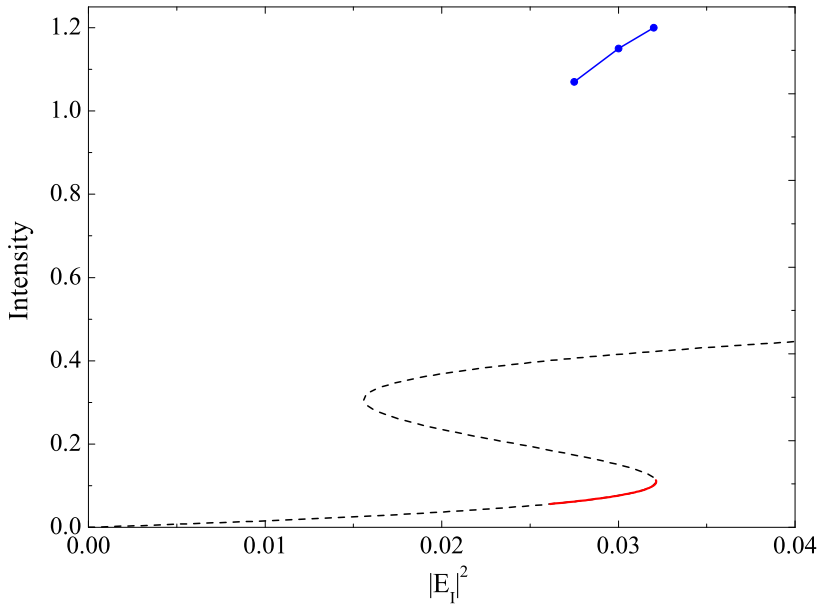

Figure 2.5: Homogeneous stationary states as a function of $|E_I|^2$. The dashed line represents the unstable solutions. The only stable part is the portion between the injection locking point and the lower turning point, shown by the solid red line. The circles indicate the peak intensity of the CS that exist in correspondence with the stable part of the lower branch. Parameters are $J = 1.05$, $\alpha = 3.0$, while $\theta = -2.3$.

2.3.6 Reduced equations

The model described in equations 2.14 is however, numerically stiff to integrate. This stiffness arises directly from the introduction of the dynamical polarisation variable. The resulting model exists with all the dynamical variables evolving on different time scales ($E \implies$ 10ps, $P \implies$ 100fs and $D \implies$ 1ns). To overcome this problem, we introduce two new models and discuss the positive and negative aspects of each. The first includes a simple adiabatic elimination of the polarisation and re-normalisation of the time scales as shown in equations (2.27) [21, 26].

$$\frac{\partial E}{\partial \tau} = \frac{E_I - i\left(\alpha + \theta\right) E + i\nabla^2 E}{\sqrt{\varepsilon}} + \left(1 - i\alpha\right) WE \tag{2.27a}$$

$$\frac{\partial W}{\partial \tau} = \sigma\left[J - \left(1 + \sqrt{\varepsilon}W\right)\left(1 + |E|^2\right)\right] \tag{2.27b}$$

Where $\tau = \varepsilon^{3/2}t$, $D = 1 + \sqrt{\varepsilon}W$ and $\gamma = \sigma\varepsilon^2$.

The second reduction procedure was reported in [27] and reviewed in [21]. This reduction used perturbative methods based on Centre Manifold theory to reduce the number of dynamical variables, allowing for a significant portion of the numerical stiffness to be removed. This model, shown in equations (2.28), accurately reproduces the results of equations (2.14), but with a reduction of computational overhead of approximately 100.

$$\frac{\partial E}{\partial \tau} = \frac{E_I - i\left(\alpha+\theta\right)E + ai\nabla^2 E}{\sqrt{\varepsilon}} + \left(1-i\alpha\right)WE + \sqrt{\varepsilon}\left(1-i\alpha\right)\left(1+\sqrt{\varepsilon}W\right)\left(\mathcal{L}E+Z\right) \tag{2.28a}$$

$$\frac{\partial W}{\partial \tau} = \sigma\left\{J - \left(1+\sqrt{\varepsilon}W\right)\left(1+|E|^2\right) - \varepsilon\,\mathrm{Re}\left[\left(1-i\alpha\right)E^*\left(\mathcal{L}E+Z\right)\right] + d\varepsilon^{3/2}\nabla^2 W\right\} \tag{2.28b}$$

$$\mathcal{L} = -\frac{i\nabla^2}{\xi(1)+i\varepsilon\nabla^2} \tag{2.28c}$$

$$Z = -\frac{1}{\xi(1)}\left[E_I - i\left(\alpha+\theta\right)E + \sqrt{\varepsilon}\left(1-i\alpha\right)WE\right] \tag{2.28d}$$

Where $D = 1+\sqrt{\varepsilon}W$. Note that the operator $\mathcal{L}$ has not been expanded further in ε for numerical convenience. Equations (2.27) can be easily obtained by only keeping terms up to order ε^0 in the equation for E and order $\varepsilon^{3/2}$ in the equation for W. This corresponds to a standard adiabatic elimination of the variable P.

2.4 Semiconductor laser with frequency selective feedback

Here, we introduce the setup and model for a laser with FSF, using a VCSEL as the semiconductor laser. Further, we define some key parameters of these equations and their role in establishing both a stable model and Laser Cavity Solitons (LCS).

2.4.1 Experimental setup

The experimental setup of the VCSEL with FSF is shown in figure 2.6. The output of the VCSEL is coupled to an external, self-imaging cavity which is enclosed by a Volume Bragg Grating (VBG). The VBG provides feedback over a narrow frequency range which is injected back into the VCSEL. The Fresnel reflection from an uncoated glass surface is used to couple out light for detection. LCS are written in this system with an incoherent, pulsed addressing beam which

is applied through the VBG.

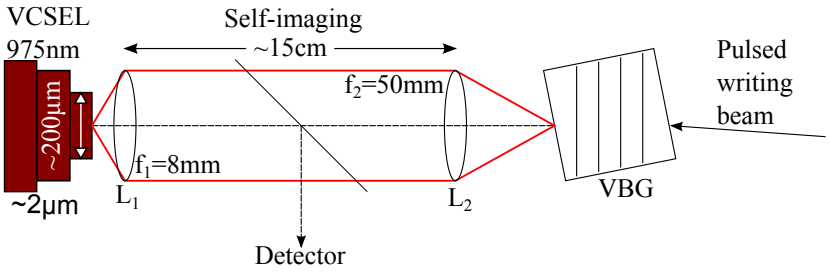

Figure 2.6: Experimental setup for the VCSEL with FSF. VCSEL is a vertical cavity surface emitting laser, BS is the beam splitter used to couple out the light for detection and VBG is the volume Bragg grating. Addressing is provided by the pulsed writing beam which is applied through the VBG.

2.4.2 Theoretical model

To model the experimental setup of figure 2.6, separate descriptions of the VCSEL device and the VBG are required. The latter provides the FSF, lowering the laser threshold over a narrow frequency range around the peak of the Bragg reflection. Away from this frequency the feedback is negligible, as most light is transmitted by the VBG.

The temporal dynamics of semiconductor lasers with optical feedback has been modelled for some time (see for example [28]). The present experimental setup however, requires the inclusion of transverse-space degrees of freedom, including diffraction, and also a high reflectivity of the feedback mirror. We combine all these elements in a single model that can be compared with the experimental realisations and does not restrict to purely temporal regimes and/or introduce restrictions in the magnitude of the feedback [29].

Our model for the intra-VCSEL optical field, E, and carrier distribution, N, is based on that used for the study of CS in optical amplifiers [22, 30, 20]. The holding beam is, however, replaced by the external cavity field at the VCSEL output mirror, F. The complete system is described by the following system of equations [29]:

$$\frac{\partial E}{\partial t} = -\left(1+i\theta\right)E + i\nabla^2 E - i\sigma\left(\alpha+i\right)\left(N-1\right)E + \frac{2\sqrt{T_1}}{\left(T_1+T_2\right)}F \tag{2.29a}$$

$$\frac{\partial N}{\partial t} = -\gamma\left[N - J + |E|^2\left(N-1\right) + D\nabla^2 N\right] \tag{2.29b}$$

$$F(t) = e^{-i\delta\tau_f}\hat{G}\left(t-\frac{\tau_f}{2}\right)\left[-r_1 F\left(t-\tau_f\right) + t_1 E\left(t-\tau_f\right)\right] \tag{2.29c}$$

where θ is the detuning of the VCSEL cavity with respect to the chosen reference frequency, σ is a coupling constant, α is the linewidth enhancement factor, T_1 and T_2 are the transmittivities of the VCSEL mirrors and J represents the injection current, normalised to the value at transparency. Time is scaled to the VCSEL cavity lifetime, and γ is the ratio of cavity lifetime to carrier response time in the VCSEL. The term $i\nabla^2 E$ describes diffraction in the VCSEL cavity, while $D\nabla^2 N$ describes the carrier diffusion. It should be noted that the coefficient for the carrier diffusion, D, is considered small and therefore carrier diffusion effects are henceforth omitted.

The external cavity round-trip time and its detuning to the reference frequency are denoted by τ_f and δ respectively, while r_1 and t_1 are the (real) amplitude reflection and transmission coefficients of the VCSEL output mirror (i.e. $T_1 = t_1^2 = 1 - r_1^2$: for a detailed description of the external cavity, see [31]). The operator $\hat{G}$ describes the frequency selective operation of the VBG on the field envelope and is given by:

$$\hat{G}(t)[h(t)] = \frac{r_g}{2\beta} \int_{t-2\beta}^{t} e^{i\Omega_g(t'-t)} h(t')dt' \tag{2.30}$$

in the time domain, or equivalently,

$$\hat{G}(\omega)[h(\omega)] = r_g e^{-i\beta(\Omega_g-\omega)} sinc(\beta(\Omega_g - \omega))h(\omega) \tag{2.31}$$

in the frequency domain. The frequency $1/\beta$ determines the bandwidth of the VBG while Ω_g is the central frequency (henceforth referred to as the Bragg frequency) relative to the reference (carrier) frequency. The parameter r_g is an overall reflection coefficient. Note that in the description we neglect the transverse wavevector dependence of the reflector response. We have also ignored transverse effects of free-space propagation (i.e. diffraction) in the external cavity, since in the corresponding experiment the VCSEL output coupler is imaged directly onto the VBG (see figure 2.6).

The validity of equation 2.29 extends to regimes of high reflectivity of the feedback mirrors that cannot be investigated with the more usual Lang-Kobayashi (L-K) approximation for lasers with external feedback [28, 32, 33, 34], in which the effects of multiple round trips in the external cavity are neglected. The model (2.29), however, describes operational regimes of CS lasers with arbitrarily high reflectivities of the frequency-selective feedback mirror and captures the physical status of the feedback loop as a true optical cavity [31]. From the simulation point of view, the inclusion of multiple round trips is accomplished with essentially no

additional computational overhead with respect to the L-K approximation [29]. LCS have been initially described in this model in [29].

2.4.3 External cavity model vs. Lang-Kobayashi approximation

Here, we examine in more detail, the advantages of the full external cavity model shown in equations (2.29) compared to the more common L-K approximation, which is generally used to model lasers with external feedback (see, e.g. [28, 32, 33, 34, 35, 36, 37]). In the latter, the effects of multiple round trips in the external cavity are neglected, giving rise to a VCSEL feedback field which is simply a scaled delayed version of the VCSEL output. This can be justified only if the external cavity finesse is sufficiently small to neglect multiple-interference effects. The model given in equations (2.29) describes operational regimes of CS lasers with arbitrarily high reflectivities of the FSF mirror [38]. It also recovers the L-K approximation by setting the VCSEL external reflection coefficient to zero, thus allowing for a quantitative comparison.

Figure 2.7 compares the full external cavity and L-K models for two different external cavity finesses, controlled by altering the reflection coefficient r_g of the VBG. Figure 2.7 (a)-(d) show there are some quantitative and qualitative differences which become more pronounced as r_g is increased. This is not unexpected. The key point, however, is illustrated in figures 2.7 (b) and (d) which plot the threshold current as a function of frequency. For an external reflectivity of as low as $r_g = 0.25$, the laser threshold current in the L-K model is almost equal to the transparency current ($J = 1$). For an external reflectivity of $r_g = 0.81$, which corresponds approximately to experimental conditions [38], the L-K laser threshold is well below transparency, indicating that lasing is predicted to occur even without a population inversion, which is unphysical.

The source of the problem lies in the failure of the L-K approximation to conserve energy through its one-sided neglect of the reflectivity of the VCSEL output coupler. As examination of equations (2.29) shows, this can lead to a feedback strength which exceeds the VCSEL cavity losses, and hence to unphysical linear gain even when the laser gain medium is absorbing rather than amplifying. Numerical simulation of the system under these conditions does indeed lead to rapid blowup of the optical field E.

In contrast, a more physical treatment of the feedback loop as a true optical cavity [31] avoids this problem by observing the boundary conditions and conserving energy at the VCSEL output coupler. Moreover, this regularisation

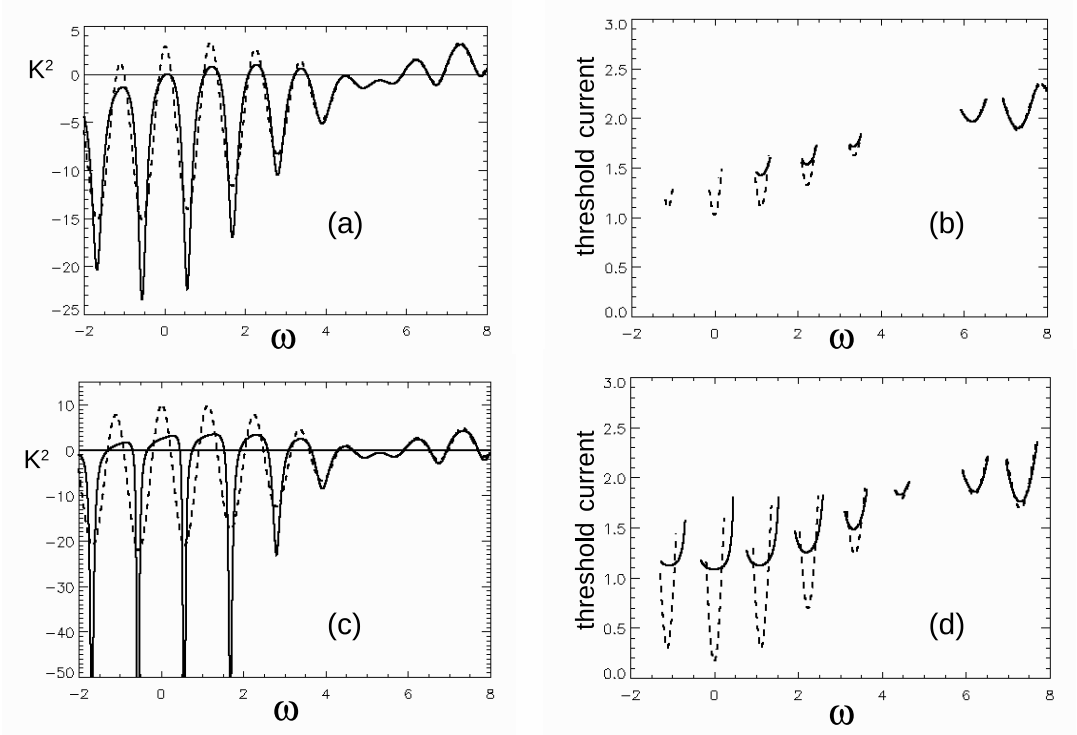

Figure 2.7: Comparison between the external-cavity model (solid line) and the Lang-Kobyashi model (dashed line). (a) and (c) Plane-wave modes $K^2(\omega)$ for the laser with FSF, for $r_g = 0.5$ and $r_g = 0.9$, respectively. Only portions of each curve above the line $K^2 = 0$ are physically relevant. (b) and (d) Threshold current versus ω for the modes in (a) and (c), respectively. (d) Depicts threshold currents below the transparency value of $J = 1$ for the Lang-Kobyashi approximation, indicating lasing even when the laser medium is not amplifying. Parameters: $\alpha = 9$, $\theta = -3$, $\sigma = 0.9$, $\gamma = 0.01$, $T_1 = 0.008$, $T_2 = 0.0002$, $\beta = 1.0$, $\delta = 0$, and $\tau_f = 50$. Image reproduced with permission [29].

is accomplished with essentially no additional computational overhead [31]. As equations (2.29) show, only one extra addition and multiplication are required per time step with respect to the L-K approximation, while storage requirements for fields at earlier times are the same in both the L-K and external-cavity approaches.

2.4.4 Travelling-wave modes

The calculation of travelling-wave modes was reported in [29]. Here we discuss the consequences of these travelling-wave modes on the bistability of the system. Examples of the laser modal spectrum are shown in figure 2.8, along with the corresponding mode thresholds. The small scale oscillations in figure 2.8 reflect the narrow mode spacing of the external cavity, while the larger-scale modulation

is due to the response of the VBG. There is clearly a set of modes grouped around the grating frequency ($\omega = 0$) and other modes coming into effect around the VCSEL lasing frequency, with a frequency gap in between. The former modes owe their existence to the strong feedback provided by the VBG in the region of $\omega = 0$ and, as a result, have the lowest thresholds. The latter modes exist where the feedback is small and so can be termed VCSEL modes, although the influence of the external cavity is still apparent.

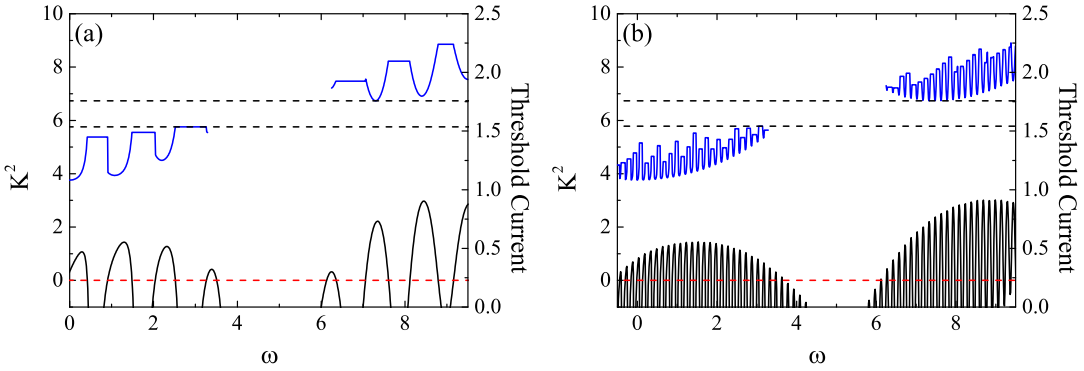

Figure 2.8: Plots of the threshold current as a function of frequency, close to the central frequency of volume Bragg grating in the laser with FSF. (a) Shows the threshold current for $\tau_f = 0.05$ns while (b) shows the threshold current for $\tau_f = 0.41$ns. The gap indicated between the two horizontal (dashed) lines indicates the region where both the patterned and homogeneous steady state is stable. Other parameters are $\alpha = 9$, $\theta = -1$, $\sigma = 0.9$, $\gamma = 0.01$, $T_1 = 0.008$, $T_2 = 0.0002$, $\beta = 0.6$, $\delta = 0$ and $r_g = 0.9$.

The separation of grating-determined modes and VCSEL modes is accomplished through the detuning between the VCSEL and grating frequencies. Suitable operating conditions will also create a threshold gap between the highest-threshold VBG modes and where the lowest-threshold VCSEL-determined modes exist (i.e., the system can lase) but where the laser off state is also stable (i.e., the system can also not lase). In this region there is therefore bistability between lasing and nonlasing states, and the possibility of observing localised lasing on a zero-field background: in other words, LCS [29, 39, 40].

2.5 Kerr cavity

For the Kerr cavity, we consider a ring cavity containing a Kerr medium. The Kerr medium provides the nonlinear self-focusing effect required for the existence of CS. The ring cavity, shown in figure 2.9, consists of four mirrors, two orthogonal to the axis of propagation with a distance L and transmission coefficient $T \ll 1$,

and two orthogonal to the transverse plane, with distance b and transmission coefficient $T = 0$.

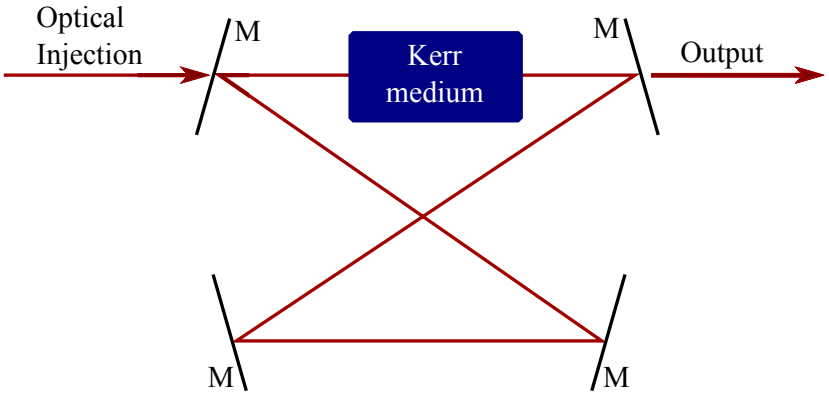

Figure 2.9: Setup of a ring cavity containing a Kerr medium. Here, M represents the mirrors enclosing the cavity and the solid line represents the path an injected signal takes.

The self-focusing effect of the Kerr medium is based on the well established fact that the refractive index, n, is proportional to the intensity of the field propagating through the medium, as shown in equation (2.32).

$$n(\omega, I) = n_0(\omega) + n_2(\omega)I \tag{2.32}$$

Where n_0 is the (linear) refractive index, n_2 is the Kerr coefficient and I is the intensity of the field propagating through the medium. Presuming the cavity is driven by a coherent, stationary plane-wave pump, E_I, the dynamics of the electric field E can be described in the mean field approximation by a perturbed nonlinear Schrödinger equation, given in equation (2.33).

$$i\frac{\partial E}{\partial t}E + \frac{\partial^2}{\partial x^2}E + |E|^2E = i\varepsilon(-E - i\theta E + E_I) \tag{2.33}$$

Where $\varepsilon > 0$ such that the right side of the equation becomes a sum of losses and gains within the cavity, with θ representing the frequency detuning. The first and second term on the left side make the *linear* Schrödinger equation, while the term $|E|^2E$ represents the Kerr nonlinearity.

By assuming $\varepsilon = 1$, the equation described above reduces to the well established Lugiato-Lefever equation:

$$\frac{\partial E}{\partial t} = E_I - (1 + i\theta)E + i|E|^2E + i\frac{\partial^2}{\partial x^2}E \tag{2.34}$$

where E is the dynamical field variable, E_I is the injected field, θ is the detuning

and $\partial^2/\partial x^2$ represents diffraction. In making the assumption $\varepsilon = 1$, it is implied that time becomes scaled to the decay time of the field [11].

2.6 Numerical Integration

Here we detail the methods of performing numerical integration, which will be used to integrate the device equations detailed in this chapter. First we introduce the split-step method, which is used to integrate the linear terms spectrally and integrate the nonlinear terms using either a second- or fourth-order Runge-Kutta method.

2.6.1 The split-step method

Consider equations of the form

$$\frac{\partial E}{\partial t} = \hat{\mathcal{L}} E \tag{2.35}$$

where $\hat{\mathcal{L}}$ is an operator which contains no explicit time-dependence. Equation (2.35) can be formally integrated to give E at some time $(t + dt)$ in terms of its value at an earlier time:

$$E\left(t + dt\right) = e^{dt\hat{\mathcal{L}}} E(t). \tag{2.36}$$

Now assume that $\hat{\mathcal{L}}$ can be rewritten as the sum of two terms

$$\hat{\mathcal{L}} = \hat{\mathcal{L}}_1 + \hat{\mathcal{L}}_2 \tag{2.37}$$

and further assume that the error introduced by neglecting $\left[\hat{\mathcal{L}}_1, \hat{\mathcal{L}}_2\right]$ is of high enough order that we can write equation (2.36) as

$$E(t + dt) \approx e^{(dt)\hat{\mathcal{L}}_1} e^{(dt)\hat{\mathcal{L}}_2} E(t). \tag{2.38}$$

In fact, it can be shown that the error introduced by neglecting $\left[\hat{\mathcal{L}}_1, \hat{\mathcal{L}}_2\right]$ can be reduced if rewrite (2.36) as

$$E(t + dt) \approx e^{(dt/2)\hat{\mathcal{L}}_1} e^{(dt/2)\hat{\mathcal{L}}_2} E(t). \tag{2.39}$$

$E(t+dt)$ is now calculated in three steps. We first calculate E' as the solution at $t = dt/2$ of the equation

$$\frac{\partial F}{\partial t} = \hat{\mathcal{L}}_2 F \tag{2.40}$$

with initial condition $F(0) = E(t)$. Then we solve for E'' given by $F(dt)$ where

$$\frac{\partial F}{\partial t} = \hat{\mathcal{L}}_1 F \tag{2.41}$$

and $F(0) = E'$. Finally, $E(t+dt)$ is given by solving (2.40) at time $t = dt/2$ with an initial condition given by E''.

To calculate $E(t+ndt)$ the above procedure is carried out repeatedly. Thus

$$E(t) = e^{(dt/2)\hat{\mathcal{L}}_2} e^{(dt)\hat{\mathcal{L}}_1} e^{(dt)\hat{\mathcal{L}}_2} \dots e^{(dt/2)\hat{\mathcal{L}}_2} e^{(dt)\hat{\mathcal{L}}_1} e^{(dt)\hat{\mathcal{L}}_2} E(0). \tag{2.42}$$

The motivation behind such method is to find a splitting of $\hat{\mathcal{L}}$ such that equations (2.40) and (2.41) can be solved fairly easily. The equations studied in this thesis take the form

$$\frac{\partial E}{\partial t} = a\nabla^2 E + b(E) \tag{2.43}$$

where b is a nonlinear function, containing no spatial dependence and a is a complex number. This gives an obvious splitting, reducing equations (2.40) and (2.41) to

$$\frac{\partial E}{\partial t} = a\nabla^2 E \tag{2.44a}$$

$$\frac{\partial E}{\partial t} = b(E) \tag{2.44b}$$

respectively.

Equation (2.44a) can be solved spectrally. This is easily achieved by using fast Fourier transforms to move into the frequency domain and by taking the inverse to move back to the time domain, a process which is $O(dx^N)$ where dx is the space step and N is the dimension of the grid. [24, 41, 42]. Since equation (2.44b) has no spatial dependence, it can be solved at each point of the numerical grid using a standard technique for solving ordinary differential equations [24, 41, 42]. In section 2.6.2 we describe both the second- and fourth-order Runge-Kutta methods, used to solve the nonlinear terms of the models described in this chapter.

2.6.2 The Runge-Kutta method

The Euler method is defined as:

$$y_{n+1} = y_n + hf(x_n, y_n). \tag{2.45}$$

This method advances the solution from x_n to $x_{n+1} \equiv x_n + h$. This formula is, however, unsymmetrical. It advances the solution through an interval h, but uses derivative information from the beginning of the interval only. As a result, the step's error is only one power of h smaller than the correction, i.e., $O(h^2)$ added to equation (2.45). An example is shown in figure 2.10.

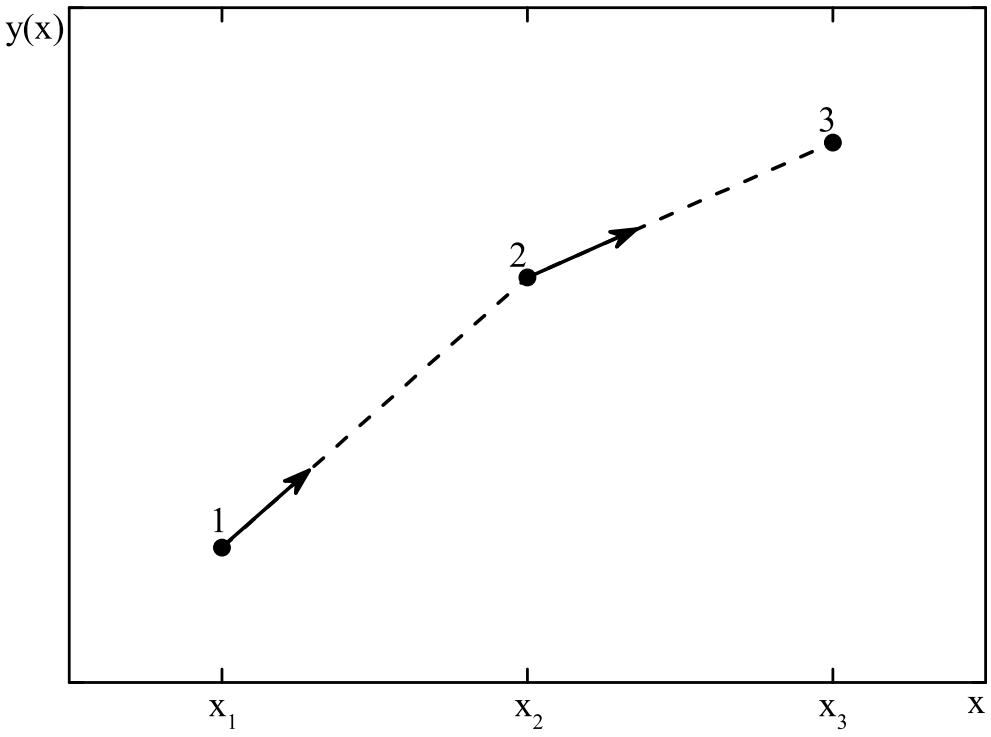

Figure 2.10: Example of the Euler method. A full step is taken on the first evaluation.

$$\begin{aligned} k_1 &= hf(x_n, y_n) \\ k_2 &= hf(x_n + \frac{1}{2}h, y_n + \frac{1}{2}k_1) \\ y_{n+1} &= y_n + k_2 \end{aligned} \tag{2.46}$$

The second-order Runge-Kutta method utilises a step similar to that shown in equation (2.45) to take a trial step to the midpoint between the intervals. We then

use the values at the midpoint to compute the real step across the full interval. An example of this is given in equations (2.46) and shown in figure 2.11. This symmetrisation cancels out the first-order error term resulting in a second order error of $O(h^3)$ [41, 42].

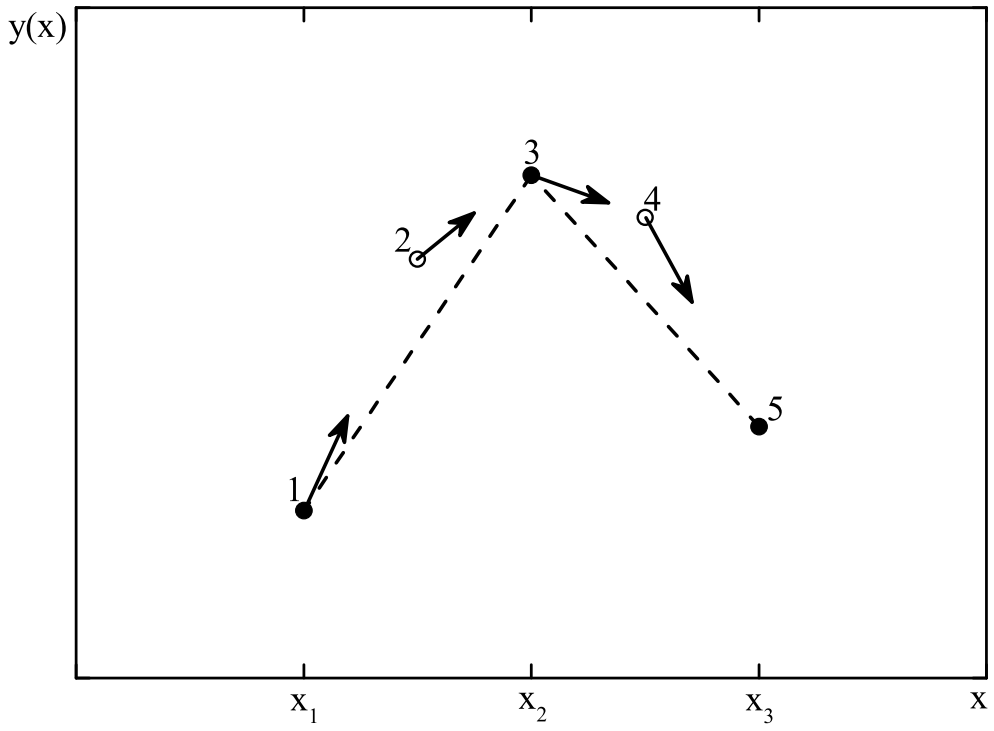

Figure 2.11: Example of the second-order Runge-Kutta method. A trial step is taken before evaluating the full step.

$$\begin{aligned} k_1 &= hf(x_n, y_n) \\ k_2 &= hf(x_n + \frac{1}{2}h, y_n + \frac{1}{2}k_1) \\ k_3 &= hf(x_n + \frac{1}{2}h, y_n + \frac{1}{2}k_1) \\ k_4 &= hf(x_n + h, y_n + k_3) \\ y_{n+1} &= y_n \frac{1}{6}k_1 + \frac{1}{3}k_2 + \frac{1}{3}k_3 + \frac{1}{6}k_4 \end{aligned} \tag{2.47}$$

This method can of course be generalised further, however the most common methods are the *second-* and *fourth-* order Runge-Kutta methods. Further, for the numerical integration of the device equations detailed in this chapter, we utilise either a second- or fourth- order method. The fourth-order Runge-Kutta method is shown in equations (2.47) and in figure 2.12. Here each step (h) requires

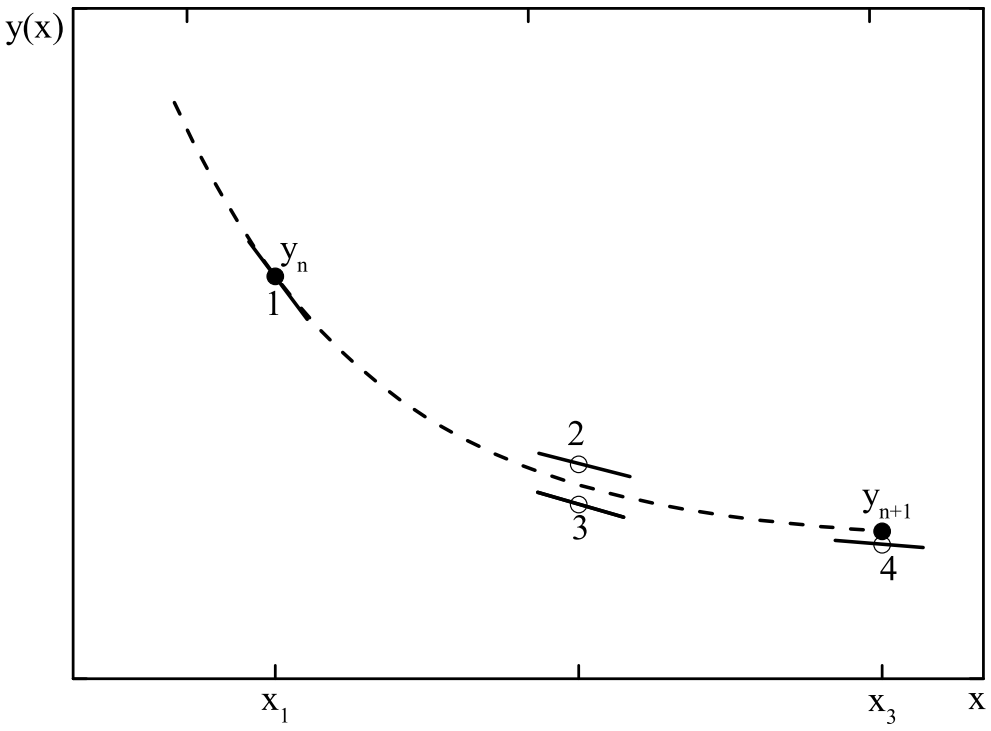

Figure 2.12: Example of the fourth-order Runge-Kutta method. A derivative is evaluated four times for each full step: once for the initial point, twice at trial midpoints and once at a trial endpoint. The final value of the function is then calculated from these derivatives.

four evaluations, resulting in an error $O(h^5)$ [41, 42]. For the models described in this chapter, the step size takes the range $0.01 \leq h \leq 0.1$, with the laser with optical injection model using the value $h = 0.002$, the laser with FSF model using the value $h = 0.01$ and the Kerr cavity model using the value $h = 0.001$.

Chapter 3

Writing cavity solitons in photonic devices

3.1 Introduction

In chapter 1, a set of criteria was introduced which can be used to determine if a localised structure is indeed a Cavity Soliton (CS). In this chapter, an examination of the first criterium is presented. In order to be considered a CS, localised states must coexist with a stable background state over the parameter range of their existence. The background can be homogeneous or quasi-homogeneous and should be linearly stable against weak perturbations. This implies that CS can be present or absent under the same conditions of operation, i.e. they exhibit bistability between "off" and "on" states.

A CS is a stable, self-localised optical excitation sitting on a uniform or quasi-uniform background, and substantially independent of transverse boundary conditions. In this introductory discussion we sketch some basic features which follow from these properties for practical applications, both for single isolated and multiple CS.

We begin by considering the existence, stability and excitation of a single CS. By assumption, for any suitable externally-controlled parameter, Q, there is a range of values over which both the CS 'on' state and CS 'off' states are stable. For clarity, small values of Q are defined to correspond to a weak nonlinearity. Since a CS is an intrinsically nonlinear object, there will be a minimum value, say Q_A, below which no CS exists. We also expect that there will be some maximum value, Q_B, above which the CS either does not exist or becomes unstable. Since all CS in a given system are identical, and distinguishable from the background, we must be able to define a "power" measure P, such that a single CS has power

P_1, and n CS have power nP_1. We have set the background "power" to zero, which may exist naturally in a system or can be achieved by subtraction. We will assume P_1 to be positive, since in this thesis we consider only bright solitons. We thus arrive at a schematic P vs Q diagram, shown in figure 3.1, consisting of a set of parallel lines, spaced by intervals P_1 and extending from Q_A to Q_B, the first rung corresponding to a single CS, the second to two, and so on. In a real system, of course, the rungs would be neither exactly horizontal nor exactly straight, but that is not important in the present context of a qualitative discussion.

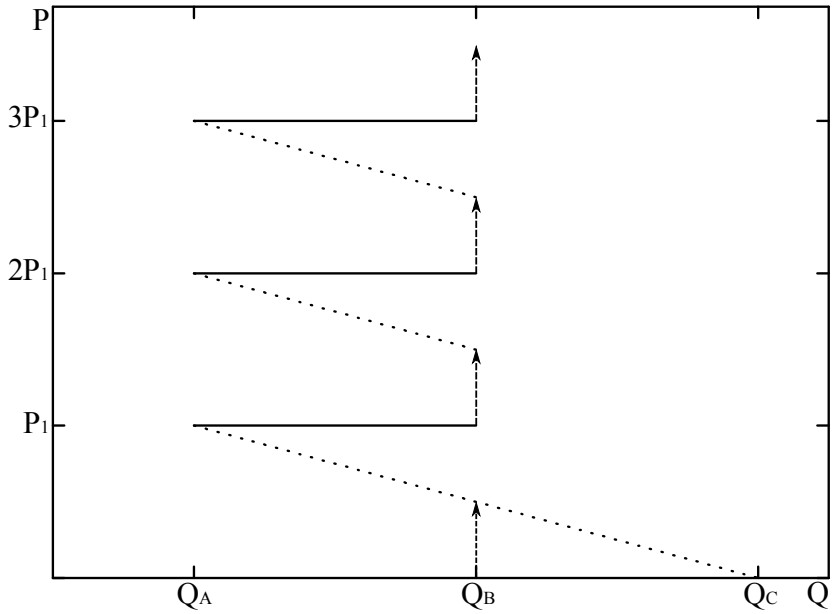

Figure 3.1: Schematic power (P) vs. control parameter (Q – see text) for the excitability of CS in photonic systems. Solid lines correspond to stable structures, dotted lines show the separatrix between the basins of attraction and the dashed arrow shows the minimum perturbation required to excite a CS within the range of stability and existence. Figure adapted with permission and thanks from [43].

We now consider, with reference to figure 3.1, the dynamics of excitation (writing) and erasure of CS, beginning with the former. In order to write one (or more) CS in such a system, a perturbation is required to increase the power locally such that $P > P_S$. The value P_S, represented in figure 3.1 by the diagonal dotted lines, separates the basins of attractions for the "off" and "on" states and can therefore be considered a separatrix between the two states. It is also important to note that the dotted lines represented by P_S also correspond to a third state, although this state is unstable. Hence, when an appropriate perturbation is applied, the system power is increased beyond the separatrix and the CS is switched on.

Physically, this is done with a spatially localised writing beam which adds

energy to the system for a specific amount of time, after which the writing beam is switched off [44]. With such a localised writing beam factors such as the width of the writing beam, amplitude and the duration that the writing beam is active are key to the successful creation of a single CS. If these parameters are incorrectly set, a multi-peaked structure can form which can separate into two (or more) distinct and separate CS. Alternatively, the separatrix may not be crossed with insufficient values and the CS would not switch on. If the perturbation to the system is great enough to cross the separatrix, the CS switches on and if not then the system returns to the background state.

Such writing beams can be coherent or incoherent with respect to the VCSEL output frequency, and each has its advantages and disadvantages. A coherent beam requires a system where the frequency and phase are locked by an external optical pump. In such systems, quicker writing times are achieved compared to similar systems using an incoherent writing beam [45]. In contrast, in systems where the phase is not locked to that of an external beam, it is impossible to achieve a completely coherent writing beam. Therefore, the only solution is to use an incoherent writing beam. Although this allows us to perturb the system without the need for an optical pump, this method is (in general) slower for writing times, as the energy input is not converted into an optical excitation as efficiently.

We examine now the erasure process, introduced in figure 3.2. Since the conditions which support the existence of CS require $Q \geq Q_A$, a small negative perturbation to its power will cause it to decay when Q is only just above Q_A. At any value of Q within the region where stable CS exist, it is possible to find the minimum perturbation necessary to destroy the CS. Since the required negative perturbation is small at Q_A, but increases with Q as the CS becomes more stable, this switch off power curve will have the general form of the dotted line falling away from the rungs of the "ladder" in figure 3.2. The dotted line in figure 3.2, again, tracks a separatrix between the basins of attraction of the no CS and one (or more) CS states. As such, we again define this dotted line to be P_S. By applying a negative perturbation, with sufficient magnitude to cross the separatrix, the CS will return to the "off" state.

Physically, this is can be achieved in number of ways. A localised erasing beam can be utilised if the phase of the CS is known. This is easily achieved in systems where the phase is locked to an external holding beam. Where the phase is not known, an optical pulse can be used to interfere with the carrier distribution [46], exciting the carriers in the region where the CS is located and inhibiting

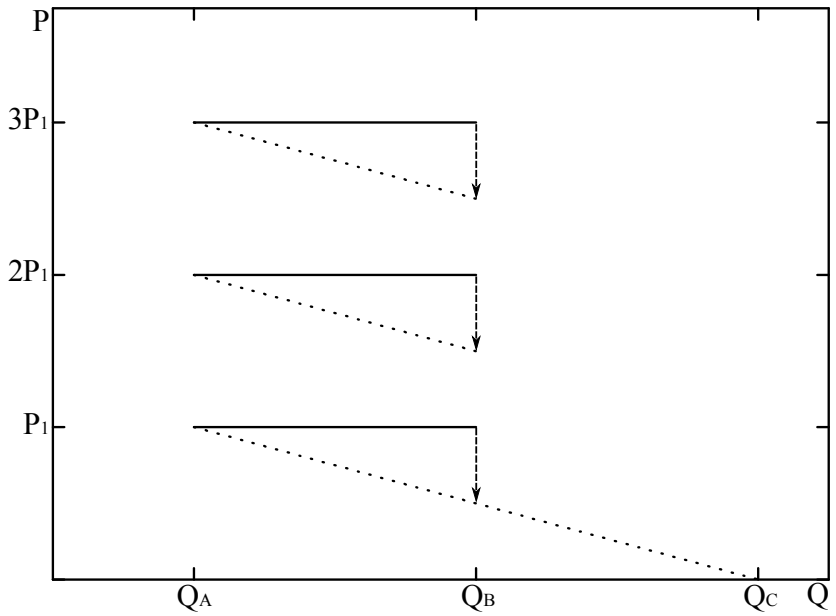

Figure 3.2: Schematic power (P) vs. control parameter (Q – see text) for the de-excitability of CS in photonic systems. Solid lines correspond to stable structures, dotted lines show the separatrix between the basins of attraction and the dashed arrow shows the minimum perturbation required to switch a CS off within the range of stability and existence. Figure adapted with permission and thanks from [43].

the stimulated emission in the region. This can be used to cause the magnitude of the CS to drop until it crosses the separatrix and switches "off". Another method is to take advantage of localised defects in the device structure. This is particularly useful in semiconductor devices, where localised defects develop during the epitaxial growth process. One can exploit a region where CS are stable in a localised defect and simply erase them by pulling them out of the defect and into a region where the CS is no longer stable.

This chapter is structured as follows. In section 3.2 we examine the writing and erasing process in lasers with optical injection. In this example, a coherent writing beam is used both to create and erase the CS in the device. The coherent writing beam is created by splitting the holding beam from the master laser, as detailed in section 2.3.1 and shown in figure 2.1. In particular, attention is drawn to the advantages of the laser configuration over passive configurations using this setup. Section 3.3 provides details on writing and erasing CS in lasers with frequency selective feedback. In this system there is no readily accessible coherent source which can be used to provide the writing beam, therefore the injection of energy to perturb the system has to be drawn from an incoherent source. This, coupled with the fact the CS in this system are free to choose their

own phase and frequency provides a challenge for the erasing procedure. This can be overcome by perturbing the lasers carrier distribution to the point where the CS is switched off. Physically, this can be provided by means of a localised external optical pulse injected to the system. Finally, section 3.4 introduces the writing process in a simplified Kerr cavity model. This is achieved by a coherent address beam, in a similar manner to that described for the laser with optical injection.

3.2 Writing and erasing cavity solitons in lasers with optical injection

In order to write and erase CS in lasers with optical injection, a coherent, pulsed input signal is injected and the energy is transferred into CS. The simulations and results from this section were obtained using the models described in chapter 2.3.6 and rewritten here for convenience after the adiabatic elimination of the polarisation using the application of the Centre Manifold theory [27], with equations (3.1) referring to the reduction using the perturbative method based on Centre Manifold theory, as sketched in [27] and equations (3.2) referring to standard adiabatic elimination of the polarisation.

$$\begin{aligned}
\frac{\partial E}{\partial \tau} &= \frac{E_I - i\left(\alpha+\theta\right)E + ai\nabla^2 E}{\sqrt{\varepsilon}} + \left(1-i\alpha\right)WE \\
&\quad + \sqrt{\varepsilon}\left(1-i\alpha\right)\left(1+\sqrt{\varepsilon}W\right)\left(\mathcal{L}E+Z\right) \\
\frac{\partial W}{\partial \tau} &= \sigma\left\{J - \left(1+\sqrt{\varepsilon}W\right)\left(1+|E|^2\right) - \varepsilon\,\mathrm{Re}\left[\left(1-i\alpha\right)E^*\left(\mathcal{L}E+Z\right)\right]\right\} \\
\mathcal{L} &= -\frac{i\nabla^2}{\xi(1)+i\varepsilon\nabla^2} \\
Z &= -\frac{1}{\xi(1)}\left[E_I - i\left(\alpha+\theta\right)E + \sqrt{\varepsilon}\left(1-i\alpha\right)WE\right]
\end{aligned} \tag{3.1}$$

If we neglect ε^0 terms in the field equation and $\varepsilon^(1/2)$ terms in the carrier distribution equation, one obtains a simpler set of equations:

$$\begin{aligned}
\frac{\partial E}{\partial \tau} &= \frac{E_I - i\left(\alpha+\theta\right)E + i\nabla^2 E}{\sqrt{\varepsilon}} + \left(1-i\alpha\right)WE \\
\frac{\partial W}{\partial \tau} &= \sigma\left[J - \left(1+\sqrt{\varepsilon}W\right)\left(1+|E|^2\right)\right]
\end{aligned} \tag{3.2}$$

Where E is the electric field, W the rescaled carrier density, E_I the optical injection, α the linewidth enhancement factor, θ the detuning between the optical injection and the VCSEL and J the pump current. Time is scaled to cavity decay rate ε, with $\sigma = \gamma/\varepsilon^2$, where γ is the decay rate of the carriers. Diffraction is described in two transverse dimensions by the Laplacian operator $\nabla^2 E$ and in one transverse dimension by $\partial_x^2 = (\partial^2/\partial x^2)$.

Since the reference frequency in (3.1) and (3.2) is that of the injected field, E_I can be considered a real amplitude. The writing beam is then created by simply adding a perturbation, say $U(x,t)$, to the optical injection which takes the form $E_I = E_{I0} + U(x,t)$, over a finite spatial range and for a finite duration. This creates the spatially localised writing beam, with width l and active for duration t. In figure 3.3, we show the system before, during and after the writing process with one transverse spatial dimension and figure 3.4 shows the same process with two transverse spatial dimensions.

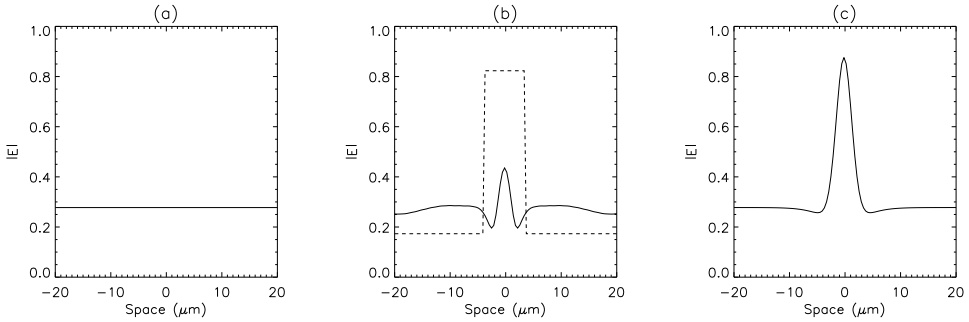

Figure 3.3: Writing process of a CS in a VCSEL with optical injection where (a) shows the system immediately prior to the application of the writing beam (the "off" state), (b) shows the system during the writing process, with the writing beam ($U(x)$) overlayed for clarity and (c) shows the system immediately after the writing beam is discontinued. Parameters are: $J = 1.05$, $\varepsilon = 0.04$, $\gamma = 10^{-4}$, $|E_I|^2 = 0.03$, $\theta = -2.3$ and $\alpha = 3.0$.

Figure 3.5 shows the intensity, phase and carrier distributions of a steady state CS in both 1D and 2D for parameter values where the lower homogeneous steady–state is stable.

Note that the peak intensity of the 2D CS is higher than that of the 1D case because of the well-known larger self-focusing effect in two transverse dimensions. When writing CS, various parameters can affect the time required to fully establish and in particular, we consider here the amplitude and the duration of the writing beam.

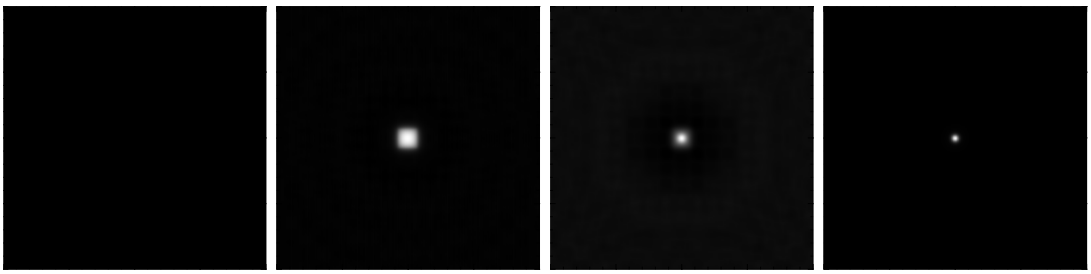

Figure 3.4: Writing process of a CS in a VCSEL with optical injection in two transverse dimensions, where (a) shows the system immediately prior to the application of the writing beam (the "off" state), (b) shows the system during the writing process, with the writing beam (U(x,t)) overlayed (dashed line)for clarity and (c) shows the system immediately after the writing beam is discontinued. Parameters are: $J = 1.05$, $\varepsilon = 0.04$, $\gamma = 10^{-4}$, $|E_I|^2 = 0.03$, $\theta = -2.3$ and $\alpha = 3.0$.

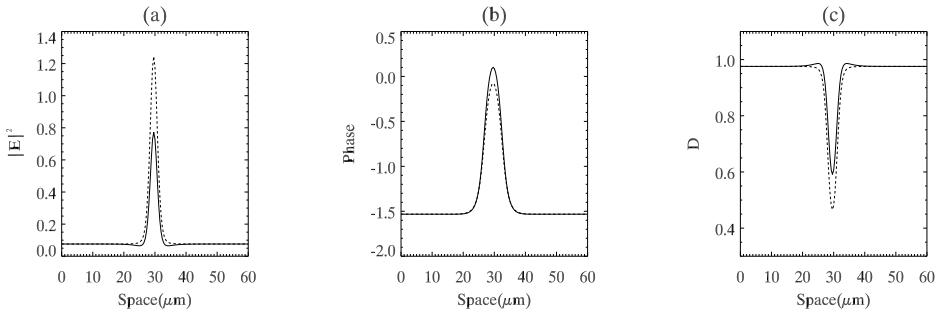

Figure 3.5: Spatial distributions of (a) the intensity, (b) phase and (c) carrier density of a CS in a VCSEL with optical injection. Solid (dashed) lines are for the 1D (2D) case. Parameters are: $J = 1.05$, $\varepsilon = 0.04$, $\gamma = 10^{-4}$, $|E_I|^2 = 0.03$, $\theta = -2.3$ and $\alpha = 3.0$.

3.2.1 Writing cavity solitons in a laser with optical injection

Writing dissipative solitons in cavity media with optical injection has been accomplished both experimentally and theoretically (see e.g. [25, 47]) in passive and laser configurations. The advantage of the laser configuration over the passive configuration lies with the response time of the system. Indeed, in the passive system, the response to a coherent writing beam can be significantly slower. In figure 3.6, we show a qualitative comparison between the passive configuration (amplifier $J = 0.96$, red, dashed curve) and the laser configuration ($J = 1.05$, black, solid curve). It is clear from figure 3.6 that the minimum injection time decreases with increasing amplitude of the writing beam in both cases. The passive configuration, however, requires a pulse length approximately four times longer than that of the laser configuration. This provides a clear advantage for

the laser configuration when considering applications of CS to delay lines [20, 21] and optical memories [26, 48].

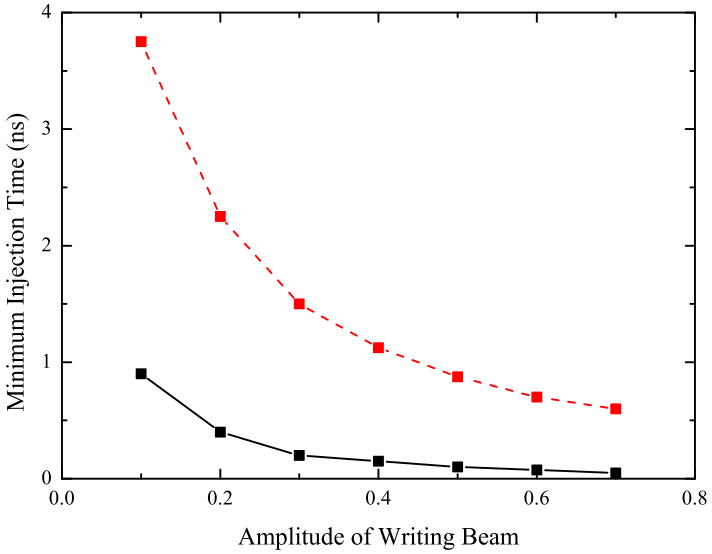

Figure 3.6: Qualitative comparison between the minimum injection time required to write a CS in the VCSEL (black/solid line, $J = 1.05$) and amplifier (red/dashed line, $J = 0.96$) cases for varying amplitudes of the address beam. Similar results have been obtained for the 2D case. Other parameters for the lasing case are fixed to the values given in figure 3.5. The parameters for the amplifier are: $E_I = 0.61$, $\theta = -2.25$ and $\alpha = 4.5$.

The minimum injection time for writing a CS is, however, not necessarily the optimum one because of the switch-on dynamics of the generated CS. In figure 3.7 we show that for a fixed value of the amplitude of the writing beam ($U_0 = 0.65$) an increase in the address beam duration from 0.15ns to 0.20ns leads to a considerably faster establishment of the CS, from around 5ns for the former to around 1ns for the latter. Further increases of the duration of the writing beam however do not further reduce the CS establishing time. Figure 3.7 shows, for example, that for an address pulse duration of 0.5ns (dot-dash line) the establishment of the CS takes around 1.8ns. This is typical of the critical behavior of CS switching as originally described and observed in a liquid crystal light valve [43, 44].

3.2.2 Erasing cavity solitons in lasers with optical injection

In order to erase CS in lasers with optical injection, an erasing beam can be used. To create the erasing beam, we use the same coherent writing beam, but introduce a phase shift of π. Again, since the reference frequency of equations (3.1) and

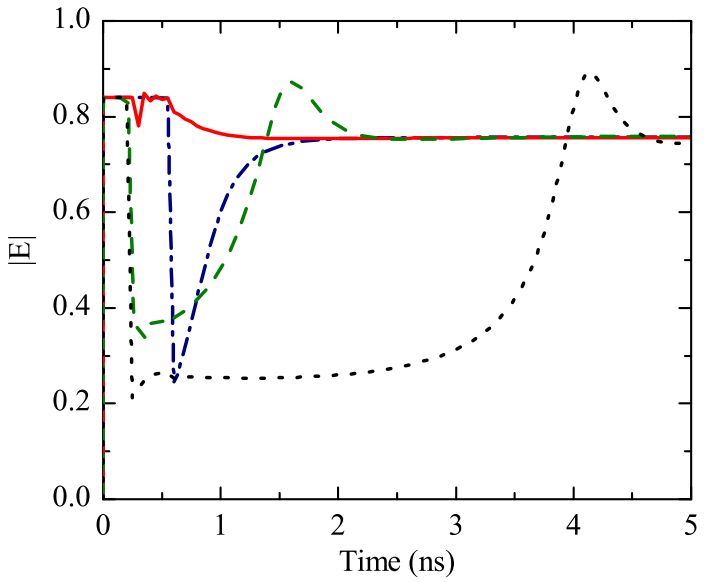

Figure 3.7: CS peak intensity during and after writing via an address beam of amplitude $A_0 = 0.65$ and various durations. Dotted line (black): duration = 0.15ns; dash line (green): duration = 0.16ns; solid line (red): duration = 0.20ns; dot-dash line (blue): duration = 0.50ns. Parameters are those of figure 3.5.

(3.2) is exactly that of the injected field, we can consider the erasing beam to be a real amplitude. The erasing beam is then created by introducing a localised negative perturbation in the optical injection, $U(x,t)$, which now takes the form $E_I = E_{I0} - U(x,t)$. This process decreases the amplitude of the electric field of the CS, in a similar way to that described in section 3.1. By using an amplitude and pulse duration sufficient to decrease the amplitude to the point where it crosses the separatrix, the CS can be easily switched to the "off" state. Figure 3.8 shows an example of a 1D CS in a laser with optical injection being erased using this method. The ability to erase these localised structures is important when considering the applications discussed in chapter 1. We will also revisit the issue of erasing in chapter 5, where we will examine another method of erasing CS based on collisions and merging.

Finally, an important point to note is that both the writing and erasing process can be performed at precise locations in the transverse plane of the VCSEL cavity. The ability to write and erase at precise locations is of vital importance when implementing applications based on this photonic system, and forms the first and third criterium, set out in chapter 1 for a localised structure to be considered a CS.

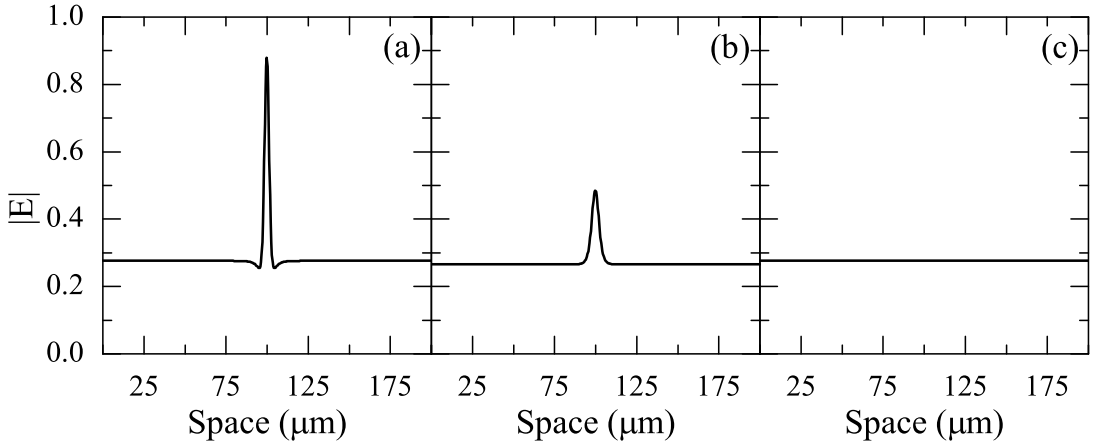

Figure 3.8: Example of a CS being erased in a VCSEL with optical injection. In (a) we show the fully established CS at time $t = 0$ns, (b) shows the amplitude decay towards the homogeneous state at $t = 5.5$ns and (c) shows the CS is completely erased and the homogeneous (or "off") state has been recovered at $t = 78.0$ns. Amplitude of the erasing beam, $A_0 = 0.1$ and the pulse duration is $t = 0.5$ns

3.3 Writing and erasing cavity solitons in a laser with frequency selective feedback

We now present and discuss the results of numerical simulations of the model described chapter 2.4, and rewritten here, for convenience.

$$\begin{aligned}
\frac{\partial E}{\partial t} &= -\left(1+i\theta\right)E + i\nabla^2 E - i\sigma\left(\alpha+i\right)\left(N-1\right)E + \frac{2\sqrt{T_1}}{\left(T_1+T_2\right)}F \\
\frac{\partial N}{\partial t} &= -\gamma\left[N - J + |E|^2\left(N-1\right)\right] \\
F(t) &= e^{-i\delta\tau_f}\hat{G}\left(t-\frac{\tau_f}{2}\right)\left[-r_1 F\left(t-\tau_f\right) + t_1 E\left(t-\tau_f\right)\right] \\
\hat{G}(t)\left[h(t)\right] &= \frac{r_g}{2\beta}\int_{t-2\beta}^{t} e^{i\Omega_g(t'-t)}h(t')dt'
\end{aligned} \tag{3.3}$$

Where E is the electric field, N the carrier density, F describes the electric field in the external cavity, θ the detuning between the VCSEL frequency and the chosen reference frequency, σ is a coupling constant, α is the linewidth enhancement factor, T_1 and T_2 are the transmittivities of the VCSEL mirrors, J is the current, δ is the detuning between the feedback field and the chosen reference frequency, τ_f is the external cavity round-trip time and r_1 and t_1 are the amplitude reflection and transmission coefficients of the VCSEL output mirror (i.e. $T_1 = t_1^2 = 1 - r_1^2$). The operator $\hat{G}$ describes the frequency selective operation at the volume Bragg

grating on the field envelope. Time is scaled to the VCSEL cavity lifetime, and γ is the ratio of the cavity lifetime to the carrier response time.

At difference with the VCSEL with optical injection, a VCSEL with Frequency Selective Feedback (FSF) is free to choose its own frequency and phase. We then investigate the effect of using a writing beam which is detuned with respect to the VCSEL output and draw attention to the spectral dynamics during the writing process.

3.3.1 Writing cavity solitons in a laser with frequency selective feedback

We have investigated in detail the Laser CS (LCS) writing process in the model (3.3). As described in the previous section, a coherent beam was readily available in the VCSEL with optical injection for use as a writing beam as the frequency and phase of the VCSEL is locked to that of the optical injection. In contrast, as the VCSEL with FSF does not have homogeneous holding beam and its frequency and phase are free, it becomes much more difficult to create an effective coherent writing beam. We then consider an incoherent writing beam, where we initiate a LCS through the application of a spatially-localised rectangular writing pulse $A(x,t)$ of the form

$$A(x,t) = A_0 \exp\left(-\frac{x^2}{\eta^2} - i\omega_p t\right) \mathrm{rect}\left(\frac{t}{\tau_p}\right). \tag{3.4}$$

where A_0 is the amplitude of the writing beam, η controls the width, ω_p is the frequency with respect to the chosen reference frequency and τ_p is the duration the writing beam is active. All of these parameters can be varied independently. Computationally, the writing beam is added to VCSEL field equation of (3.3). In the simulations the writing beam parameters are dimensionless. In order to make a qualitative comparison with the experiment we consider a typical cavity decay time of 10ps. Figure 3.9 shows the intensity, phase and carrier distribution of a steady state LCS, in a VCSEL with FSF, where the homogeneous steady state solution is also stable.

In [29] a fixed width and frequency ($\omega_p = 0$) of the address pulse was used to map a region of successful LCS initiation in the plane of amplitude, A_0, and duration, τ_p. Here, instead, we first investigate the effect of the frequency ω_p on the minimum amplitude A_0 necessary for the initiation of a LCS. We fix the value of the address pulse duration at around 50 round trips of the external cavity (i.e. around 20ns). Figure 3.10 (a) shows that there is an optimal frequency shift of

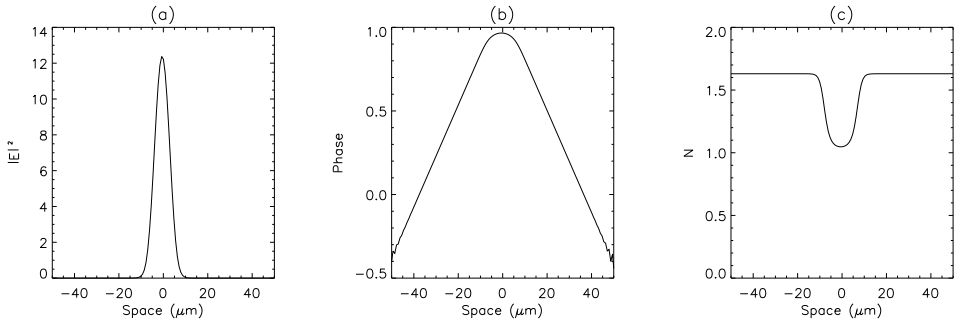

Figure 3.9: Spatial distributions of (a) the intensity, (b) phase and (c) carrier distribution of a LCS in a VCSEL with FSF. Parameters are $\alpha = 9$, $\theta = -1$, $\sigma = 0.9$, $\gamma = 0.01$, $T_1 = 0.008$, $T_2 = 0.0002$, $\beta = 0.6$, $\delta = 0$, $r_g = 0.9$ and $\tau_f = 0.05$ns.

around 3.5 (corresponding to around 55GHz or 0.18nm in experimental values) for which the lowest-amplitude address pulses can generate a LCS. This detuning value is in qualitative agreement with the experimental finding. Our finding that a blue-detuned frequency is optimal for writing of LCS in VCSEL systems with FSF is also in agreement with the results of [49] which utilise a diffraction grating and also with [29], where figure 6(b), and the associated discussion, demonstrates that the lowest-amplitude LCS for a given current has higher frequency than the stable LCS.

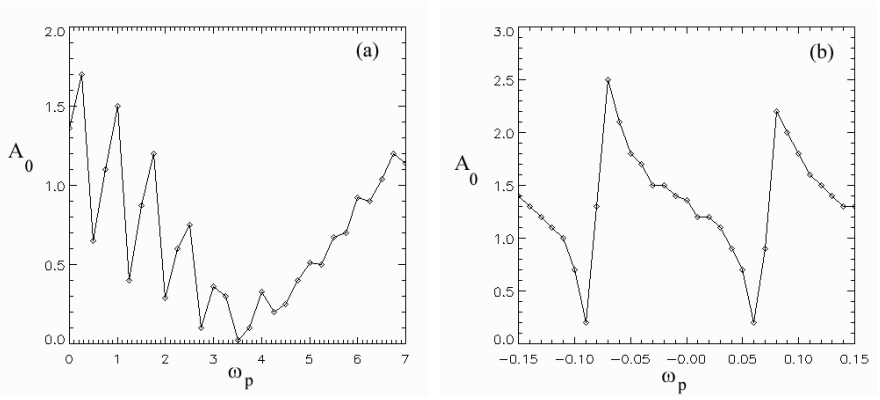

Figure 3.10: Minimum value of the address beam amplitude A_0 versus its frequency shift ω_p. Parameters are: $\alpha = 9$, $\theta = -1$, $\sigma = 0.9$, $\gamma = 0.01$, $T_1 = 0.008$, $T_2 = 0.0002$, $\beta = 0.6$, $r_g = 0.8$, $\delta = 0$, $\tau_f = 41$, $\eta = 5$, and $\tau_p = 2000$. Panel (b) is a continuation and magnification of panel (a) to show the details of the resonances with the cavity mode frequencies.

The envelope of the threshold characteristic presented in figure 3.10 (a) is quite jagged. Although this figure is affected by undersampling of the frequency scale, the existence of peaks and troughs is due to the external mode structure. For example, figure 3.10 (b), obtained with a higher frequency resolution, shows that

when scanning ω_p there are clear resonances with the frequencies of the external cavity modes which affect the optimal operation of the switching-on process.

We next fix the frequency shift, ω_p, to the lowest optimal value (the minima of figure 3.10) and proceed to determine the minimum value of the amplitude A_0 as a function of the writing beam duration τ_p. Figure 3.11 shows that there are two distinct regions in an amplitude *vs* duration diagram: for pulse lengths below about 15ns, the minimum address amplitude increases as the address pulse shortens, while above 15ns the minimum amplitude remains constant. The constant minimum address power for long address pulses translates into a direct proportionality between the pulse energy Q and its duration τ_p as shown in the inset of figure 3.11.

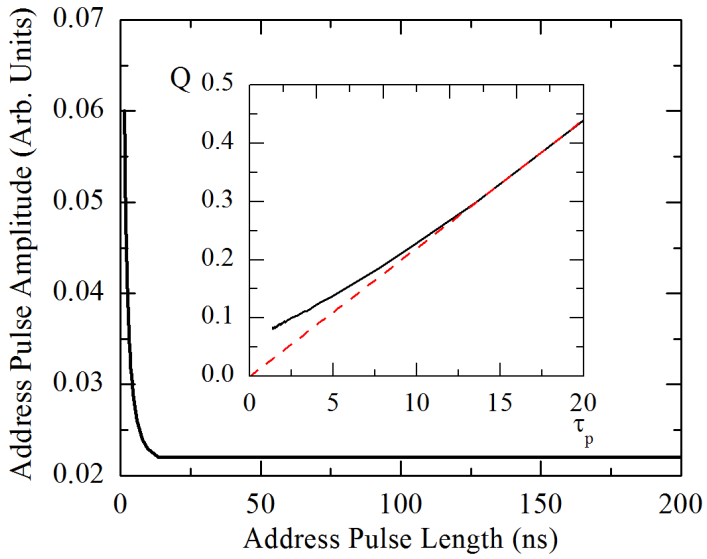

Figure 3.11: Minimum address beam amplitude A_0 for successful switching versus its duration τ_p. Parameters as in Fig. 3.10 apart from $\omega_p = 3.5$. The solid line in the inset displays the threshold energy Q of the address beam versus the address pulse length τ_p. The linear behavior observed at large pulse lengths (dashed line) extends to 200ns. Note that no LCS is generated for pulse lengths below 1.5ns.

In figure 3.12, the experimental results [50] from a similar exploration to find the minimum writing beam amplitude as a function of the pulse length is shown for comparison with the numerical results of figure 3.11. The experiment is the one described in section 2.4. When comparing the results of figure 3.11 with those of figures 3.12 (a) and (b), there is a good qualitative agreement between the numerical simulations and the data from the VCSEL with FSF experiment. The cross-over between the two regimes occurs at different values of the pulse

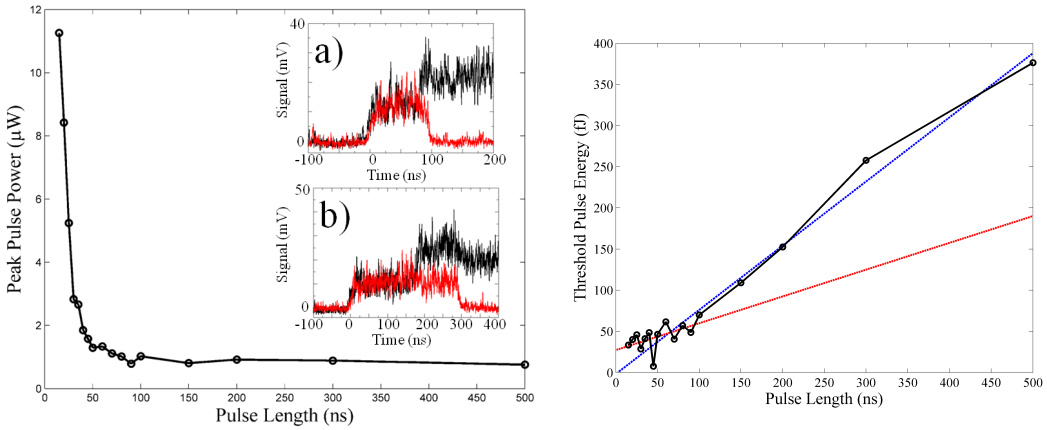

Figure 3.12: Experimental results for comparison, the left panel shows the minimum peak pulse power required to switch on a LCS for varying pulse lengths and the right panel shows the minimum energy required to switch a LCS on for varying pulse lengths. The lower linear fit (red) is for all pulses shorter than and including 100ns, the upper linear fit (blue) is for all pulses longer than and including 100ns. Inset: Time trace of switch-on events for 100ns pulse (a), 300ns pulse (b). The red line corresponds to the WB pulse and the black line shows the response of the LCS. Images reproduced with permission.

duration for the experiment and for the numerical simulations. Note that the latter were performed at the optimum frequency for the writing of LCS. Better agreement is, however, found for other values of the pulse frequency ω_p. For example, in the simulations of [29], the cross-over occurred at pulse durations of around 70ns for $\omega_p = 0$, i.e. closer to the experimental observation.

Typical behaviours from numerical simulation of the LCS switching in the two regions identified in figure 3.11 are shown in figure 3.13 (a) and (b), respectively. For short durations of the writing beam, τ_p, the address amplitude A_0 is higher at threshold than the case of longer τ_p. Away from threshold (upper traces in figure 3.13 (a) and (b)), delays between the switch on of the LCS and the writing beam pulse are strongly reduced. This is in agreement with the results obtained for the VCSEL with optical injection, and presented in section 3.2 (e.g. see figure 3.7). Figure 3.14 shows the LCS peak intensity as a function of time, obtained from experimental results of the FSF system. There is again good agreement between the experimental observations of figures 3.14 where the delay reduction is most noticeable at longer writing beam durations, and the numerical results of figure 3.13.

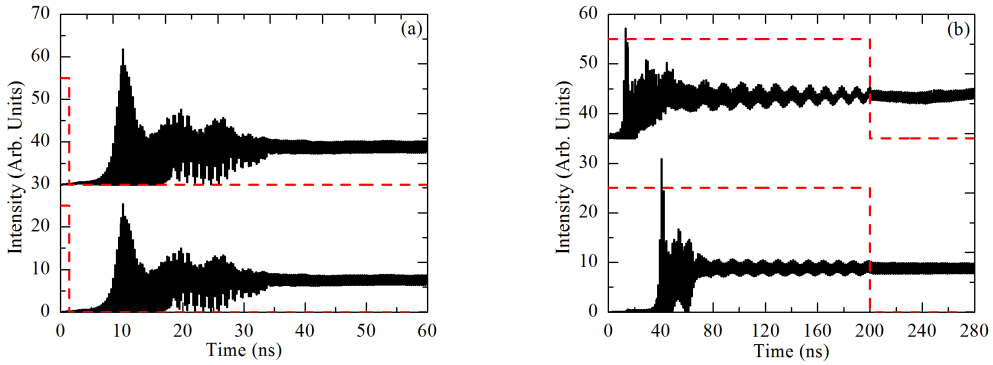

Figure 3.13: Time evolution of the peak output intensity of the LCS for (a) τ_p =1.5ns, $A_0 = 0.06$ (lower trace) and $A_0 = 0.6$ (upper trace); (b) τ_p =200ns, $A_0 = 0.022$ (lower trace) and $A_0 = 0.22$ (upper trace). The other parameters as in Fig. 3.10 apart from $\omega_p = 3.5$. The (red) dashed lines display the peak intensity of the address WB and is accurate in position and duration but rescaled in amplitude.

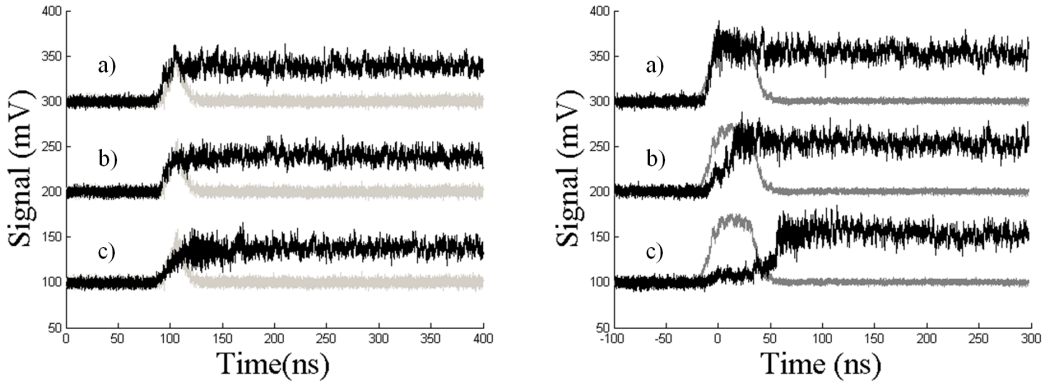

Figure 3.14: Experimental time series of pulse (grey) and LCS response (black) for comparison, (left panel) for three 15ns long pulses with power (a) 3.4, (b) 1.6, (c) 1 (normalised to threshold power) and (right panel) for three 50ns long pulses with power (a) 11.8, (b) 4.2, (c) 1. Curves are offset by 200mV for clarity. WB pulse traces are indicative of position and length but not amplitude. Traces taken using a cavity round trip time of 1.05ns.

3.3.2 Transient spectral dynamics

The successful addressing of LCS in VCSELs with FSF appears to be accompanied by transient oscillations. This was first experimentally observed in [49] and later confirmed in the numerical simulations of [29]. Here we present numerical and experimental evidence in the spectral domain, demonstrating that a considerable number of external cavity modes are involved during these transient oscillations. Only a single mode, perhaps with sidebands, remains in the final LCS state.

The numerical integration of the model (3.3) provides temporal data on the dynamics of the LCS switching. From this data we have evaluated frequency spectra as displayed in figure 3.15. We compute the spectrum of $E(x = 0, t)$ (the peak of the CS) for each round-trip and then plot the evolution of such spectrum over a slower time scale.

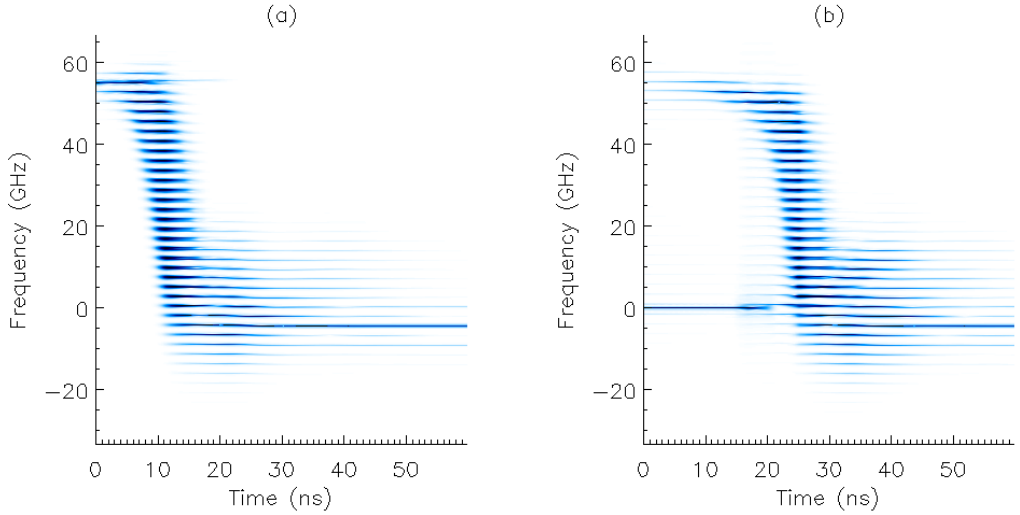

Figure 3.15: Time evolution of the frequency spectrum evaluated every round trip. Parameters are the same as in figures 3.10 but with $\tau_p = 20$ns and $\omega_p = 55$GHz (a) and $\omega_p = 0$GHz (b). Each frequency spectrum is normalized such that the highest intensity corresponds to dark blue, to avoid the dominance of the final peak.

Figure 3.15 (a) shows the transient spectral dynamics when the writing beam has a duration of $\tau_p = 20$ns and is blue-shifted from the grating frequency by around 55GHz corresponding to the minimum writing beam amplitude as determined previously. Before the end of the address pulse, multi-mode operation sets in. At $t = 10$ns from the beginning of the simulation, around 30 external cavity modes are present. This regime of frequency spreading is followed by a fast (around 5ns) sweeping of the frequency spectrum, accompanied by a narrowing to only about 15 modes. Then slower spectral evolution leads to a further narrowing

of the spectrum and to the final state of the LCS, which has one strong mode and a few weak side-modes.

Surprisingly, very similar spectral dynamics take place when the writing beam frequency is close to that of the final LCS (figure 3.15 (b)). In this case, the writing beam corresponds to $\omega_p = 0$ and yet one still observes the same three distinct dynamical regimes: creation of a band of modes close to 55GHz (3.5 in the units of figure 3.10), followed by a fast spectral broadening and frequency sweep, and finally a slower spectral narrowing to a quasi-single-mode LCS emission state. the similarity of the spectral evolution in figures 3.15 (a) and (b) suggests the existence of a globally attractive, yet unstable, oscillatory state that is initially approached, independent of the frequency of the writing beam. Note that this state still corresponds to spatial localization, since the LCS is well defined during the entire duration of the transient. Another interesting feature of figure 3.15 is that the first frequency response of the system takes place around the blue-detuned position of the minimum determined in figure 3.10 (a) independently of the frequency shift ω_p of the writing beam. This seems to correspond to the unstable low-amplitude LCS state typically found in CS laser models [29, 32, 33], which is likely to behave like a separatrix in LCS switch-on. The multiple external cavity modes present an extra complication, not just because there is a pair of LCS associated with each of many such modes, but also because there seems to be multi-mode LCS. These were theoretically described in [29] as multi-frequency final states, and it is likely that the above-mentioned globally-attractive intermediate state is also multi-mode.

It is important to note that the spectral features presented in figure 3.15 are intrinsically related to the use of an external cavity for the FSF. The frequency sweeping, in particular, has no counterpart in the VCSEL with optical injection or the Kerr cavity. More generally, a CS laser without holding beam has the freedom to change frequency. Similar phenomena might exist in the schemes relying on saturable absorption [51, 52] due to phase-amplitude coupling.

3.4 Writing cavity solitons in Kerr cavities

The process of writing CS in a Kerr cavity is similar to that used for their creation in a VCSEL with optical injection. A coherent writing beam is used at the same frequency of the holding beam, which is possible as the output frequency and phase of the Kerr cavity are locked to that of the optical injection. Therefore, a localised perturbation, $U(x,t)$ is created in the Kerr cavity field by use of a holding

beam which takes the form of $E_I = E_{I0} + U(x,t)$. In figure 3.16 we show the intensity and phase distribution of a one dimensional steady state CS in a Kerr cavity after switching off the writing beam. Note in contrast to that shown for the VCSEL with optical injection, the Kerr CS has spatial modulations in its tails. For example, modulated tails of bright CS have been observed in semiconductor microresonators well below lasing threshold [53].

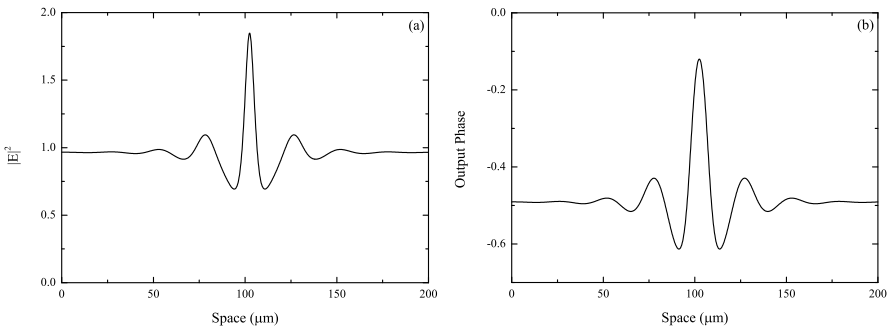

Figure 3.16: Intensity (a) and phase profile (b) for a typical, steady state, single peaked 1D CS in a Kerr cavity. Parameters are $\theta = 1.5$ and $|E_I|^2 = 1.114$.

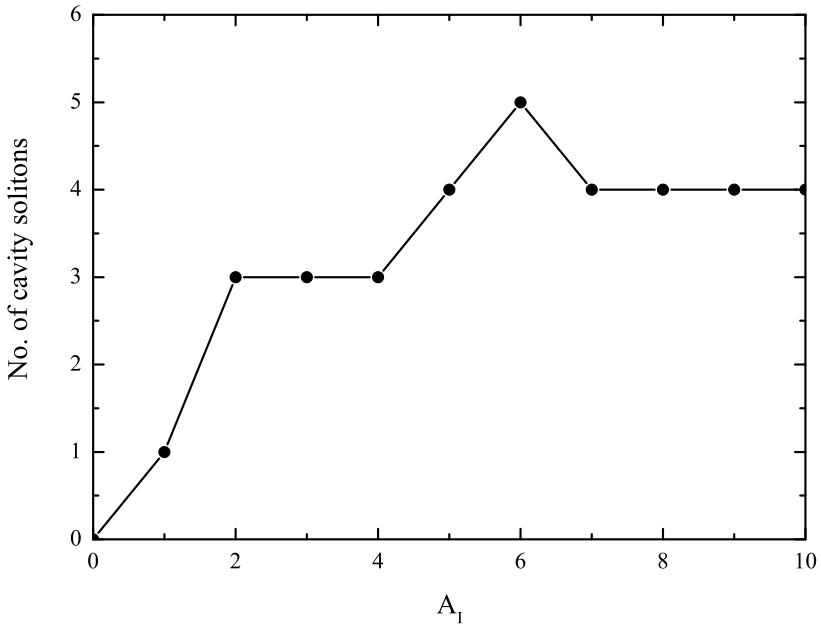

Figure 3.17: Number of solitons created as a function of writing beam amplitude, $U(x,t)$, and a fixed width of the writing beam. Parameters are those of figure 3.16.

By using a fixed (large) width of the writing beam, and increasing the amplitude $U(x,t)$ of the writing beam, we find that the number of CS created increases, as shown in figure 3.17. We can clearly see that the number of CS increases from one peak at $U = 1.0$ to five peaks at $U = 6.0$. As the amplitude increases further,

the number of peaks created returns, and remains at, four CS. This behaviour suggests that the three and four peaked structures correspond to a more stable branch of multi-CS existence while the one and five peaked structures correspond to less stable solutions.

3.5 Conclusions

In this chapter we have investigated the writing process in various photonic systems. Beginning with a VCSEL with optical injection, it has been shown that a localised coherent writing beam can be used to establish CS. In particular, when the laser configuration is compared the passive configuration below threshold, faster reaction times are observed. This leads to the CS establishing quicker for shorter pulses than possible below threshold.

The VCSEL with FSF provides an additional challenge in that it is not possible to use a coherent writing beam to create CS. However, we show that an incoherent beam is effective, and when using an incoherent beam in this system that a frequency detuning of the writing beam can provide a faster response time. Indeed, it is shown that for a writing beam frequency close to that of the final CS frequency, the initial response of the system is closer to this optimum frequency, probably corresponding to an unstable low-amplitude laser CS.

Finally, in the Kerr cavity, we show that by increasing the amplitude of the localised writing beam, multiple peaked CS can be switched on.

Of particular importance in all of these systems is the use of a *localised* writing beam. These localised beams are essential for creating single structured peaks. Additionally, the localised writing beam can be moved around the transverse plane of the VCSEL. This is essential as it provides the ability to locate the CS in precise location which will be required in later chapters and is essential for applications.

Chapter 4

Motion of cavity solitons in photonic devices

4.1 Introduction

Motion on local gradients forms part of the criteria for the existence of Cavity Solitons (CS) in photonic devices and is therefore well established in the literature. For a localised structure to be considered a CS, it is a requirement that the structure is optically controllable. In this chapter, we aim to briefly review the key established points of the motion of CS in photonic devices before presenting and discussing the results based on the numerical simulations of the models described in chapter 2.

Motion was described in optical bullet holes in one and two dimensions in a system based on a driven optical cavity with a saturable absorber in [54]. Here phase gradients of the injected field, of the form given in equation (4.1) were considered for the purpose of inducing motion.

$$E_I = E_{I0} \exp(iKx) \tag{4.1a}$$

$$E_I = E_{I0} \exp[i\varphi(x, y)] \tag{4.1b}$$

where K is a constant vector. With respect to equation (4.1a) the time derivative becomes a convective derivative, therefore stationary solutions which exist for $K = 0$ move with a velocity $v = 2aK$, where a is the diffraction parameter. This indicates that travelling CS are solutions of the equation. This procedure was then generalised to the two dimensional case in equation (4.1b), where a periodic modulation is considered. Under this local gauge transformation the damping and detuning coefficients develop a spatial dependence, and the drift velocity

becomes $v = 2a(\nabla\varphi)$. Using this method (a periodic phase modulation of the injection) has the consequence of creating a velocity with the optical bullet hole moving towards the local maxima of the phase landscape, $\varphi(x, y)$.

CS can also be self-propelled in optical cavities. In [55], a semiconductor microcavity consisting of a driven VCSEL which can act either as an absorber or an amplifier is presented. In this case, an examination of the spontaneous transition from stationary to moving CS in one a two transverse dimensional systems, is investigated through a bifurcation of the system. In the model described in [55], the detuning is not a parameter, but rather a dynamical variable which is dependant on the local temperature and is capable of spontaneous spatial variations. The movement can be thought of as arising from an instability of the stationary CS which, for an amplifier, has a temperature minimum at its centre. When the peak of the CS is displaced from the temperature minimum, it lowers the temperature at its new location but also moves on the detuning gradient on which it finds itself. In this case, when the motion is slow, the CS establishes itself at a new location and becomes fixed. However if the motion is faster, the CS keeps moving, while the temperature relaxes behind it. This process maintains the detuning gradient, allowing the motion to continue. This process holds for 'bright' CS in an active device and 'dark' CS in a passive system.

Reversible motion of CS can be described in a variety of nonlinear systems [56]. Here it is shown that, for a sinusoidal modulation of wavevector K, the soliton velocity is proportional to a function of K the spatial Fourier transform of a function related to the unperturbed CS. Therefore, when the sign of the Fourier transform changes upon variations of a control parameter, the direction in which the CS travels is also reversed. Further, at frequencies when the Fourier transform becomes zero, the CS remain stationary. This allows CS to move either towards a modulation maximum, towards a modulation minimum, or to remain stationary in spite of the background phase gradient. This was shown to hold true for systems as different as a degenerate optical parametric oscillator, a two level atomic medium and more generic models based on the Swift-Hohenberg equation and the parametrically driven Ginzburg-Landau equation.

Here we present results based on periodic modulations of the detuning and, where appropriate, of phase modulations of an injected field. We propose periodic modulations as an ideal method to induce motion for the purpose of applications in optical memory arrays. When implementing the applications described in chapter 1, it can be useful to build arrays within a single device. As such, by using periodic modulations, an array of, for example, all-optical delay lines can be

established using a single device. Further, in the next chapter, we use the periodic modulation to induce motion in two or more CS towards a common point, which allows us to examine collisions of multiple CS.

This chapter is organised as follows. In section 4.2, we introduce a range of techniques to induce motion of a CS in a VCSEL with optical injection. In particular, we use various types of periodic modulation of the phase of the optical injection and examine the effects on the CS velocity. We also consider sinusoidal modulations of the detuning and the effect on the carrier dynamics. Section 4.3 introduces motion in a laser with Frequency Selective Feedback (FSF). Here, as there is no optical injection to manipulate, we concentrate on inducing motion using periodic modulations of the detuning. Again this induces motion for the CS of this system and explains why CS are often found trapped by inhomogeneities of the background that alter the local value of the cavity resonance. Finally, section 4.4 introduces motion of CS in a Kerr cavity. Here we concentrate on inducing motion by using linear phase gradients and triangular modulations of the optical injection.

4.2 Cavity soliton motion in a laser with optical injection

When CS have been written in a VCSEL with optical injection their motion is affected by the dynamics of the background. In fact, depending on the parameters (in particular, the pumping current), CS can either have a stable background (similar to the case below threshold) or they can sit on a rapidly oscillating irregular background [25]. Here we induce CS motion by a modulation of the phase of the injected signal and by introducing a modulation of the VCSEL detuning in the regime where the background is stable.

For convenience, we rewrite the relevant model equations here.

$$\begin{aligned}
\frac{\partial E}{\partial \tau} &= \frac{E_I - i\left(\alpha+\theta\right)E + ai\nabla^2 E}{\sqrt{\varepsilon}} + \left(1-i\alpha\right)WE \\
&\quad + \sqrt{\varepsilon}\left(1-i\alpha\right)\left(1+\sqrt{\varepsilon}W\right)\left(\mathcal{L}E+Z\right) \\
\frac{\partial W}{\partial \tau} &= \sigma\left\{J - \left(1+\sqrt{\varepsilon}W\right)\left(1+|E|^2\right) - \varepsilon\,\mathrm{Re}\left[\left(1-i\alpha\right)E^*\left(\mathcal{L}E+Z\right)\right]\right\} \\
\mathcal{L} &= -\frac{i\nabla^2}{\xi(1)+i\varepsilon\nabla^2} \\
Z &= -\frac{1}{\xi(1)}\left[E_I - i\left(\alpha+\theta\right)E + \sqrt{\varepsilon}\left(1-i\alpha\right)WE\right] \qquad (4.2) \\
\frac{\partial E}{\partial \tau} &= \frac{E_I - i\left(\alpha+\theta\right)E + i\nabla^2 E}{\sqrt{\varepsilon}} + \left(1-i\alpha\right)WE \\
\frac{\partial W}{\partial \tau} &= \sigma\left[J - \left(1+\sqrt{\varepsilon}W\right)\left(1+|E|^2\right)\right] \qquad (4.3)
\end{aligned}$$

Where E is the electric field, W the rescaled carrier density, E_I the optical injection, α the linewidth enhancement factor, θ the detuning between the optical injection and the VCSEL and J the pump current. Time is scaled to cavity decay rate ε, with $\sigma = \gamma/\varepsilon^2$, where γ is the decay rate of the carriers. Diffraction is described in two transverse dimensions by the Laplacian operator $\nabla^2 E$ and in one transverse dimension by $\partial_x^2 = (\partial^2/\partial x^2)$.

4.2.1 Cavity soliton motion induced by periodic phase modulation of the optical injection

Spatially periodic modulations of the phase of the injected field provide a versatile and effective method for building arrays of CS for the desired application in multiple delay lines with a single device. Periodic modulations of the injected phase extend over a wide range of parameters where both the system and CS remain stable. This contrasts with the case of modulating injected amplitudes which easily make the CS unstable. Here we examine the one and two dimensional cases of inducing motion by spatially modulating the phase of the injected field.

Sinusoidal phase modulation of the optical injection

The simplest form of a periodic phase modulation is a sinusoidal modulation of the injected phase. The injected field term, E_I of equations (4.2) and (4.3) is now

defined as:

$$E_I = E_{I0} \exp\left[i\mu \sin(k_x x + \varphi_x)\right] \tag{4.4}$$

where E_{I0} is the amplitude of the injected field, μ is the amplitude of the sinusoidal phase modulation, k_x is the transverse wavevector of the injected phase and φ_x is an arbitrary phase shift. Figure 4.1 shows an example of a CS travelling towards the peak of a local phase maxima for this case.

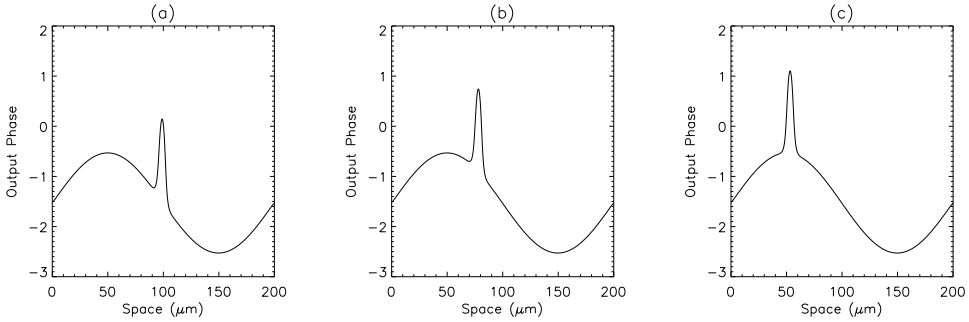

Figure 4.1: Motion of a CS induced by sinusoidal modulation of the injected phase. The output phase of the VCSEL is plotted as a function of transverse spatial coordinate, with time $t = 0.0$ns (a), $t \approx 400$ns (b) and $t \approx 1000$ns (c). Parameters are $\mu = 1.0$, $k_x = 0.036$ and other parameters are those of figure 3.5.

By varying the amplitude of the phase modulation, μ, it is possible to control the spatial gradient applied to the CS and hence its velocity. Further, by control of the wave vector, k_x, we can control the number of peaks in the modulation in a given amount of space. This is useful when considering applications built on arrays of CS. In figure 4.2, we show how the velocity of the CS varies as it moves towards a local phase maxima.

Triangular phase modulation of the optical injection

While a sinusoidal modulation of the injected phase is a simple and effective solution for inducing motion in CS and building arrays of these localised structures, the results provide a velocity which is constantly changing as the CS progresses to the nearest maximum. This is due to the fact that the applied gradient is nonlinear combined with the non-Newtonian dynamics discussed in section 1.4.2. For example, for a CS written near a minimum, the velocity increases until it is approximately halfway to the peak – the point where the gradient is at its largest. From this point the CS velocity is constantly slowing until it finally arrives at the modulation maximum, where the velocity tends to zero. For the purpose of

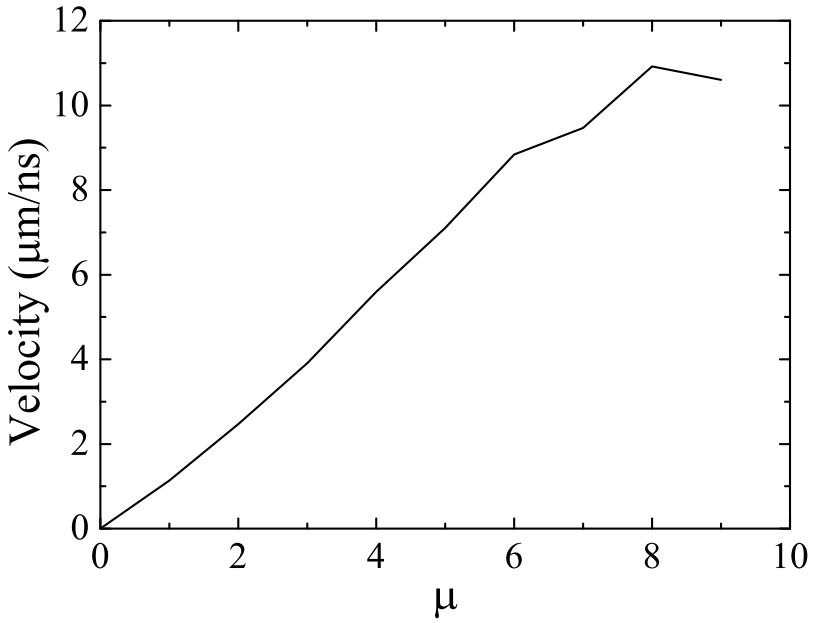

Figure 4.2: CS velocity as a function of injected phase amplitude, μ, in a VCSEL with a sinusoidally phase modulated optical injection. Here, $\gamma = 10^{-3}$, $k_x = 0.036$ and other parameters are those of figure 3.5.

applications, this can cause problems with unwanted interactions before the CS reaches the nearest maximum.

To solve this issue, a triangular modulation of the injected phase has been considered. In this case, the optical injection term, E_I in equations (4.2) and (4.3) takes the form of equation (4.5).

$$E_I = E_{I0} \exp\left\{ i \frac{2}{\pi} \mu \sin^{-1}\left[\sin(k_x x + \varphi_x)\right] \right\} \tag{4.5}$$

Again, we consider a system with one transverse dimension, with E_{I0} the amplitude of the optical injection, μ the amplitude, k_x the transverse wavevector of the injected field and φ_x an arbitrary phase shift. In this case the term $2/\pi$ is a normalisation factor. An example of the motion of a CS in a VCSEL with triangular modulation of the injected phase is shown in figure 4.3.

In a similar way to the previous case of sinusoidal phase modulation, by controlling the amplitude, μ, we can control the velocity of the CS and by controlling the transverse wave vector of the injected phase, k_x, we can control the number of peaks in a given amount of space, allowing us to build arrays of the desired CS application (e.g. all-optical delay line) in a single device. Figure 4.4 shows how the velocity varies as the amplitude, μ is increased.

The possibility exists for the realisation of these modulations in experiments.

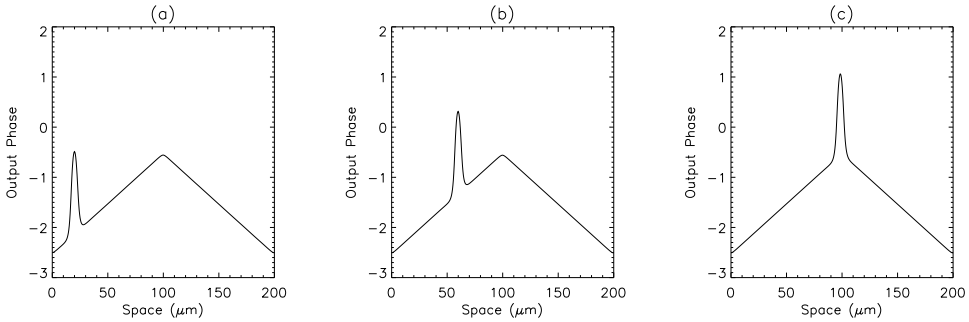

Figure 4.3: Motion of a CS induced by a triangular modulation of the injected phase, in a VCSEL with optical injection. The output phase of the VCSEL is plotted as a function of transverse spatial coordinate, x. Here, (a) is at time $t = 0.0$ns, (b) $t \approx 400$ns and (c) $t \approx 1000$ns. Parameters are $\mu = 1.0$ and $k_x = 0.036$, with other parameters as figure 3.5.

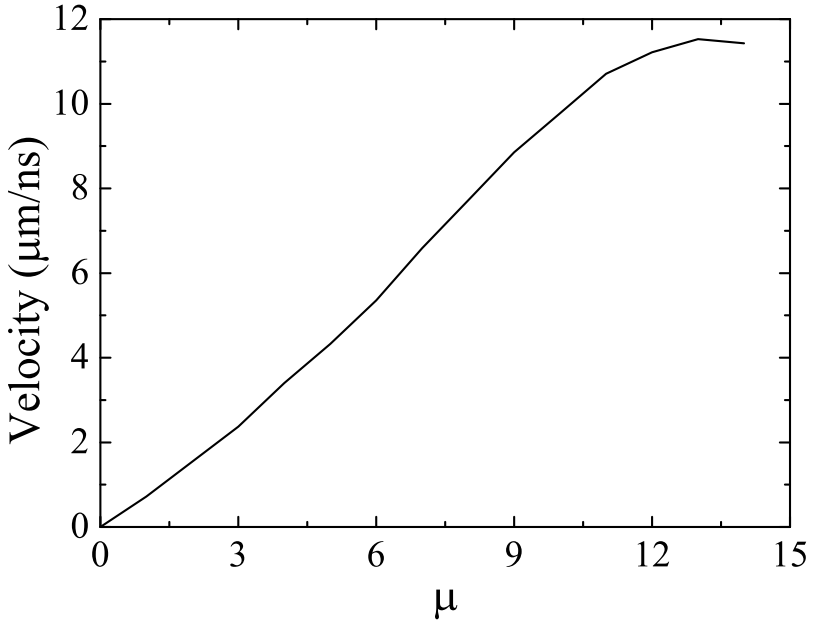

Figure 4.4: CS velocity as a function of the amplitude, μ of the injected phase, for a system with triangular phase modulation of the optical injection. Here, $\gamma = 10^{-3}$, $k_x = 0.036$ and other parameters are those of figure 3.5.

A phase mask can be introduced with the desired modulation in a similar method to described in [57]. Here CS are stabilised using a phase mask. Further, it is shown that their position can be manipulated, resulting in an square array of CS pinned by the local phase distribution [57].

Two dimensional conical phase modulation of the optical injection

With two transverse spatial dimensions, the situation becomes a little more complicated. A sinusoidal type modulation is again the simplest option but, as discussed previously, it provides a velocity which is constantly changing as the CS approaches the nearest maxima. Therefore we suggest that either a pyramid or a conical structure would provide a better solution. It should be noted that, although the pyramid structure provides a constant gradient and therefore constant velocity as the CS approaches the maxima, by introducing the soliton at different locations on a specific side, we vary the distance from the maximum, as shown in figure 4.5.

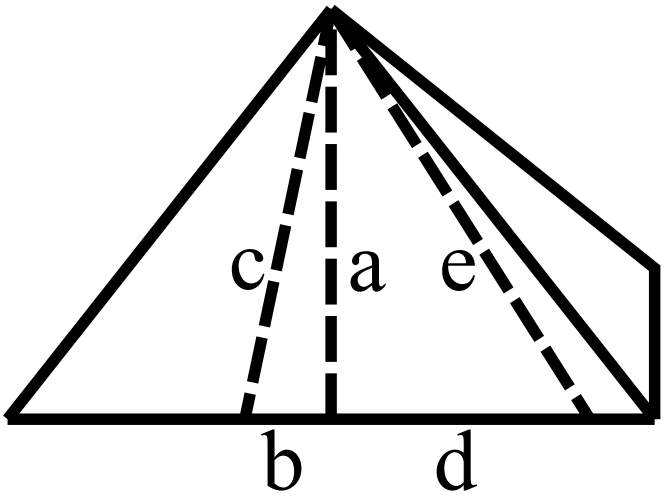

Figure 4.5: Example showing the drawback of using a pyramid structure in the phase of the optical injection. By writing CS in different locations, we can vary the distance from the nearest peak.

From figure 4.5, we can show quite simply that the two distances from the writing position and the maximum (c and e) are different. It is clear that the two lengths become $c = \sqrt{a^2 + b^2}$ and $e = \sqrt{a^2 + d^2}$. Since the length a is constant in both cases, if $b \neq d$, then $c \neq e$ must also hold true.

In this instance, a conical phase modulation is then chosen. This has the advantage of having a linear gradient between the peak and the trough, while avoiding any unnecessary velocity variations incurred when considering sinusoidal

phase modulations. To this end, we consider the optical injection, E_I to take the form:

$$E_I = E_{I0} \exp\left\{ i\frac{2}{\pi}\mu \sin^{-1}\left[\sin(k_x x + \varphi_x)\sin(k_y y + \varphi_y)\right]\right\} \tag{4.6}$$

where E_{I0} is the amplitude of the optical injection, μ is the amplitude of the phase modulation, while k_x and k_y are the transverse wave vectors of the injected phase. The constant $2/\pi$ is for normalisation and φ_x and φ_y are arbitrary phase shifts in the x and y direction, respectively. We present an example of a two dimensional CS moving towards the nearest maxima, in the presence of a conical phase modulation of the optical injection in figure 4.6.

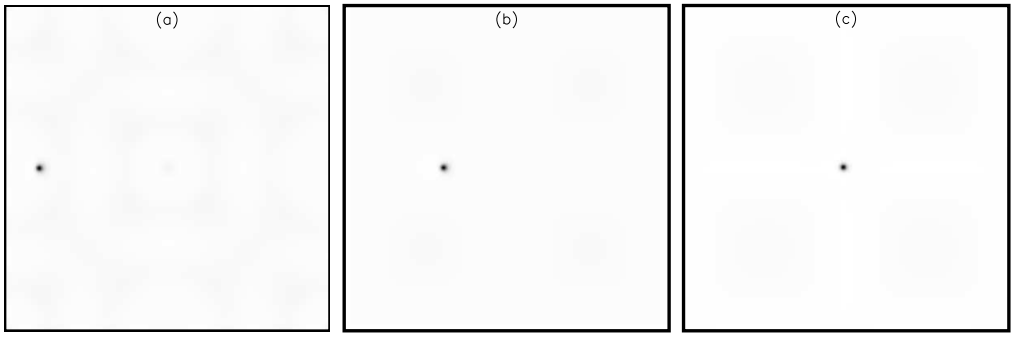

Figure 4.6: CS moving towards the local phase maxima of the optical injection in a two dimensional simulation of a VCSEL with conical modulation of the optical injection. Here, (a) is taken at time $t = 0.0$ns, (b) at $t \approx 60$ns and (c) at $t \approx 150$ns. Parameters are $\mu = 9.0$ and $k_x = k_y = 0.036$ with other parameters as shown in figure 3.5.

Again, the velocity of the CS can be controlled by varying the amplitude, μ, while the number of peaks in a given amount of space can be controlled by varying the transverse wave vectors of the phase modulation, k_x and k_y. Figure 4.7 shows how the velocity of the CS varies as the amplitude μ increases.

Comparison between the different methods of inducing motion

Here we briefly compare the advantages and disadvantages of the different methods described in inducing motion of CS, and also present results obtained with the full model. For convenience, we present in figure 4.8 (a) the three plots shown in figures 4.2, 4.4 and 4.7, along with a comparison obtained with the full model using a triangular modulation.

We note that the peak velocity of a CS on a sinusoidal phase modulation is greater than that achieved with the triangular modulation. This is due to the fact that the CS experiences a steeper gradient during parts of its journey to the

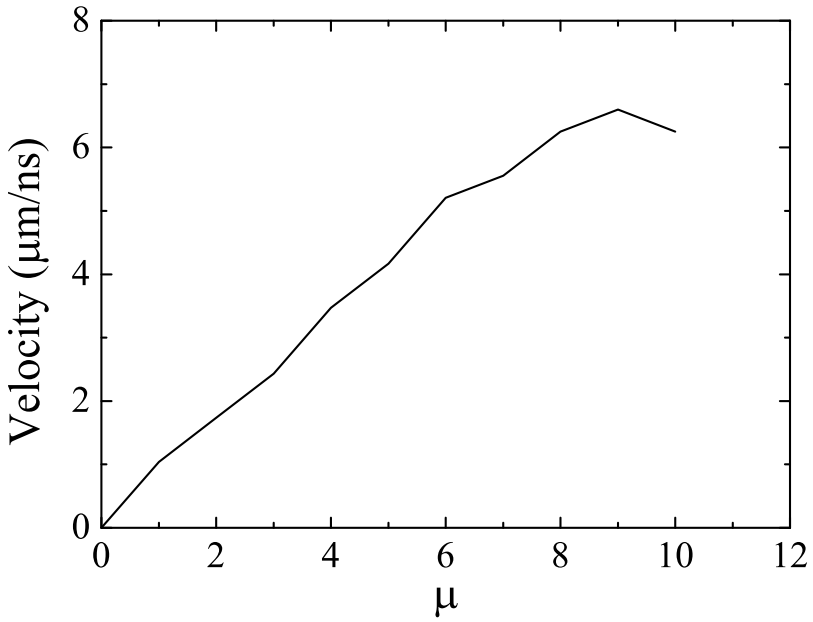

Figure 4.7: Velocity of a CS, taken from 2D simulations, as a function of the amplitude, μ, of the injected phase. Parameters are $\gamma = 10^{-3}$, $k_x = k_y = 0.036$ and other parameters are those of figure 3.5.

maxima. This, however, does not necessarily mean that the sinusoidal modulation is the best choice, as unwanted interactions can occur as the CS slows while approaching a maximum. We also note that the results obtained from the full model show excellent agreement with those obtained from the reduced models.

Varying the carrier decay rate, γ, provides another method for controlling the velocity of the CS [20], while keeping both μ and k constant. The increase in velocity is basically inversely proportional to the decay time of the carriers (see figure 4.8 (b) for 1D simulations). If γ is too small, however, the system does not support CS while if it is too large localised structures will begin to form randomly across the cavity width. Note that the range of existence and stability of the CS upon variations of γ is reduced by an order of magnitude in our active VCSEL in comparison with operation below lasing threshold where CS have a more stable background [20].

One dimensional sawtooth phase modulation of the optical injection

By introducing a sawtooth modulation of the injected phase, we observe a number of new phenomena, which are dependent on the applied gradient and the size of the phase discontinuity. Figure 4.9 introduces an example of a one "toothed" sawtooth modulation of the injected phase.

By increasing the 'amplitude' (μ, as defined in figure 4.9), and therefore the

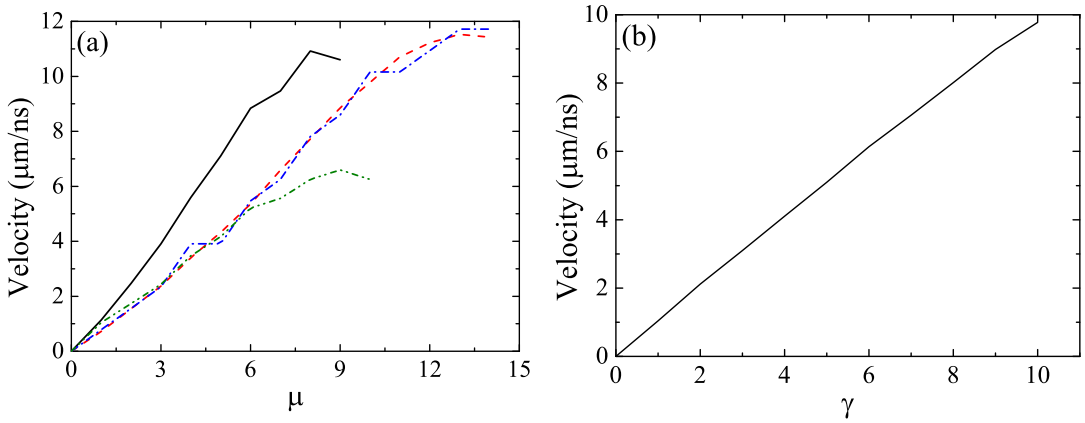

Figure 4.8: CS velocity as a function of the amplitude of the phase modulation of the injected field (a) and as a function of the decay rate of the carriers, γ (b). In (a), the motion induced by a sinusoidal modulation is shown by the solid (black) line while the motion induced by a triangular modulation is shown by the dashed (red) line in 1D and by the dot-dash-dot (green) line in 2D. Further, the dot-dashed (blue) line shows the velocity calculated using the full model (2.14) and a triangular phase modulation. Here $\gamma = 10^{-3}$, $k = 0.036$ and other parameters are those of figure 3.5. is velocity vs. In (b), $\mu = 10$, $k = 0.036$ and other parameters are those of figure 3.5.

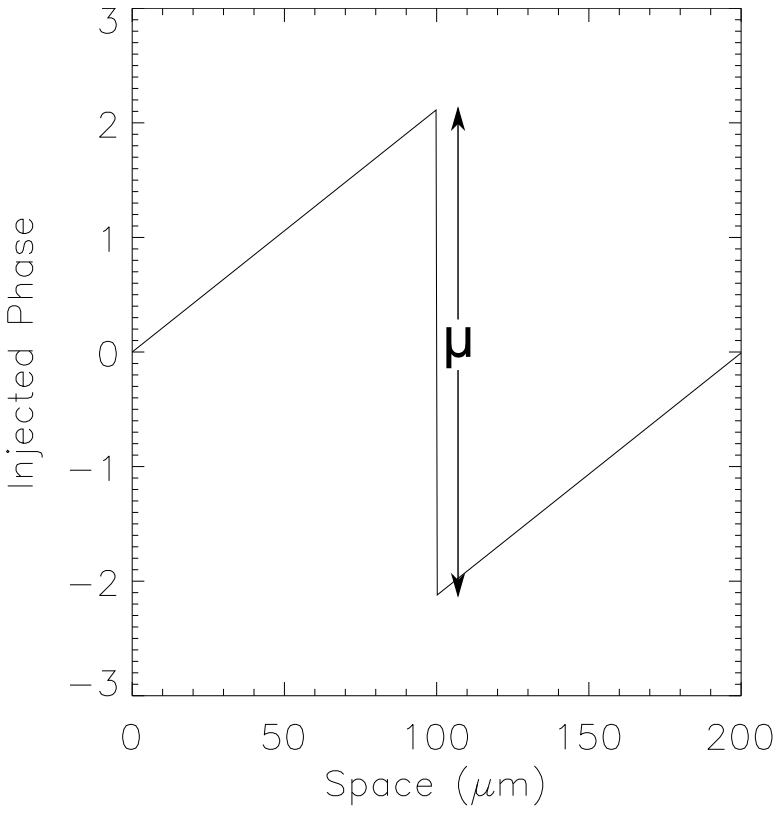

Figure 4.9: An example of the sawtooth modulation of the optical injection. We define the "amplitude" as μ, which is annotated in the diagram for convenience.

'drop' experienced at the phase discontinuity created by the sawtooth modulation, we move progressively from a region where the CS are stopped at the phase discontinuity, in a similar way to that observed for CS at a phase maximum, to regions where the CS exhibit different behaviours. The CS can either continue moving in the original direction, they can create a CS pulse train in the transverse plane of the VCSEL or they can be destroyed by the phase discontinuity. The behaviour of the CS can be controlled by adjusting the gradient of the system.

Starting with one tooth, we find that for an amplitude (or phase discontinuity size) $\mu \leq 1.121$, the CS is stopped at the phase discontinuity, as shown in figure 4.10. When we increase the amplitude to the range $1.121 < \mu < 2.14$, a CS pulse train is created (see figure 4.11), and for the range $2.14 \leq \mu < 2.15$, the CS continues past the phase discontinuity (see figure 4.12). When the amplitude is increased further, the CS is destroyed in the range $2.17 \leq \mu$, as shown in figure 4.13.

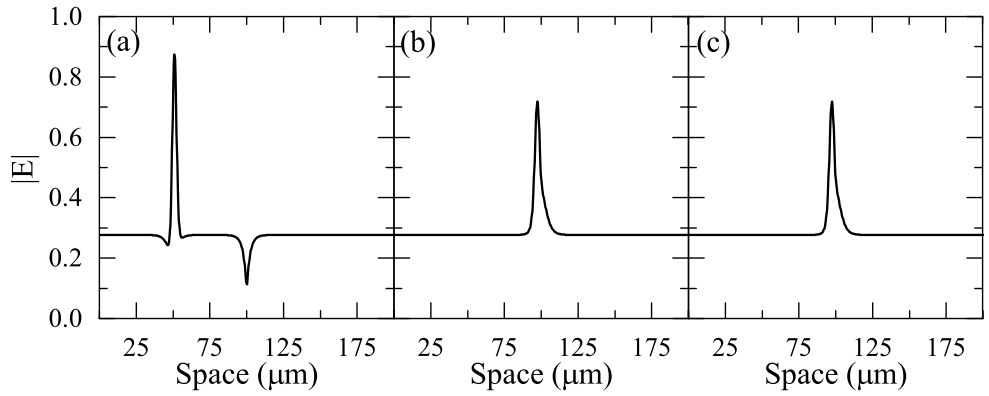

Figure 4.10: Motion of a CS with a sawtooth modulation of the optical injection. Here, the gradient is such that the CS stops at the phase discontinuity. In (a) the CS is shown at time $t = 0$ns, (b) shows $t = 57$ns and (c) shows $t = 100$ns. The gradient used is $\mu = 1.12$ and other parameters are as figure 3.5.

4.2.2 Motion induced by periodic modulation of the detuning

We now switch the method of inducing CS motion by introducing a periodic modulation of the VCSEL detuning. This modulation takes the form of equation (4.7), where a sinusoidal modulation of the detuning of the VCSEL is introduced.

$$\theta = \theta_0 + \mu \sin(kx + \varphi) \tag{4.7}$$

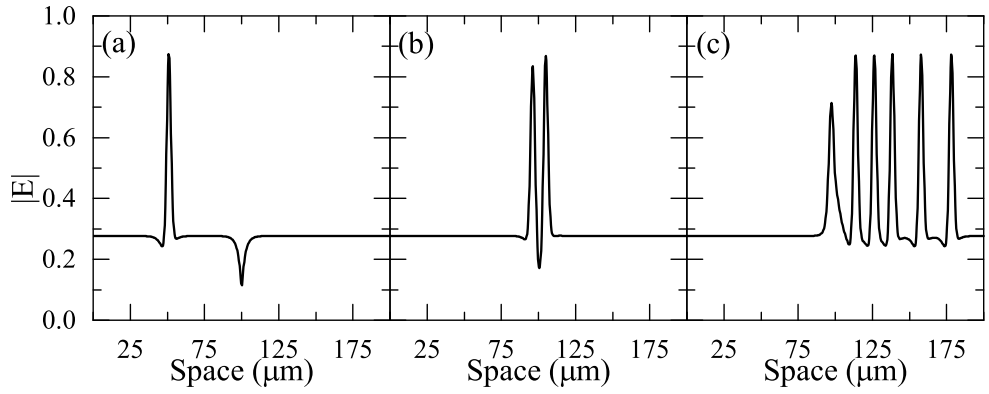

Figure 4.11: Motion of a CS with a sawtooth modulation of the optical injection. Here, the gradient is such that a CS pulse train is created at the phase discontinuity. In (a) the CS is shown at time $t = 0$ns, (b) shows $t = 57$ns and (c) shows $t = 101$ns. The gradient used is $\mu = 1.13$ and other parameters are as figure 3.5.

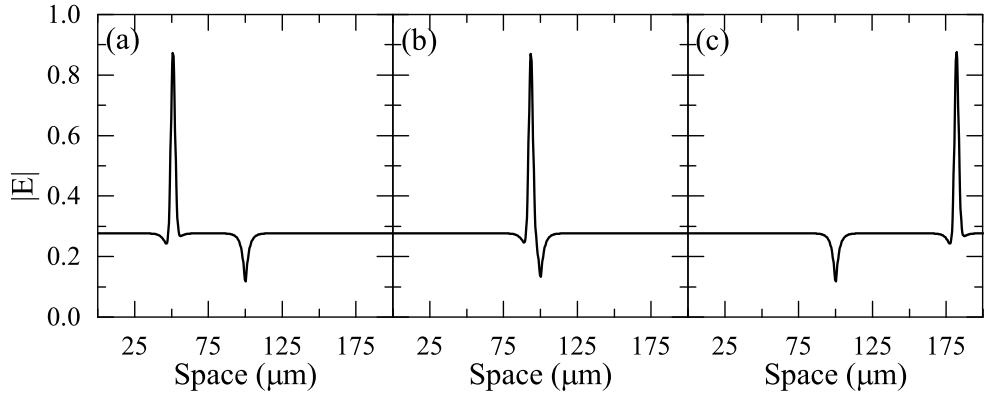

Figure 4.12: Motion of a CS with a sawtooth modulation of the optical injection. Here, the gradient is such that the CS continues uninhibited at the phase discontinuity. In (a) the CS is shown at time $t = 0$ns, (b) shows $t = 28$ns and (c) shows $t = 49$ns. The gradient used is $\mu = 2.14$ and other parameters are as figure 3.5.

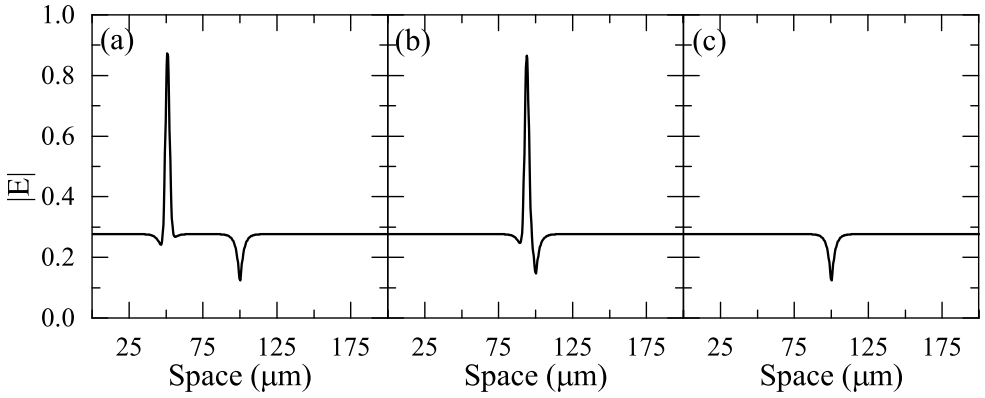

Figure 4.13: Motion of a CS with a sawtooth modulation of the optical injection. Here, the gradient is such that the CS is destroyed at the phase discontinuity. In (a) the CS is shown at time $t = 0$ns, (b) shows $t = 28$ns and (c) shows $t = 35$ns. The gradient used is $\mu = 2.17$ and other parameters are as figure 3.5.

Where θ_0 is the background detuning, μ is the amplitude, k_x is the transverse wavevector and φ is an arbitrary phase shift.

Figure 4.14 shows an example of motion in the VCSEL with optical injection, induced by a periodic modulation of the detuning. We see clearly that the CS moves towards the nearest maximum of the VCSEL field, i.e. the minimum of the detuning modulation. Note the modulations observed in the background are produced by the fact that the VCSEL is operating only slightly above threshold. Due to this, the detuning modulation induces regions where the VCSEL is operating closer too, or indeed below, the lasing threshold. This in turn creates the modulations observed in the VCSEL background.

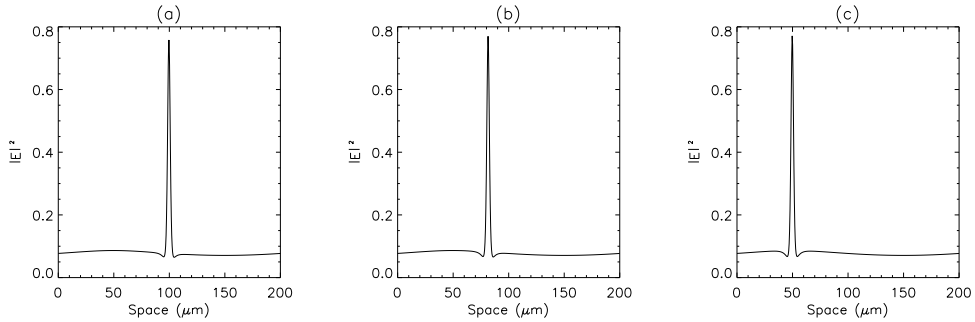

Figure 4.14: An example of motion induced by periodic modulation of the detuning of the optical injection. We show the motion from the writing position towards the nearest maximum of the modulation, with (a) at $t = 0$ns, (b) $t = 1000$ns and (c) $t = 2500$ns. Parameters are $\mu = 0.01$, $k = 0.036$ and other parameters are those of figure 3.5.

Subsequently, we have measured the velocity of CS when propelled by a detun-

ing modulation. Figure 4.15 shows the velocity as a function of the amplitude, μ of the detuning modulation. We can clearly see that, while using detuning modulation does indeed induce motion, the range of the motion is limited with respect to that observed when using phase modulations of the optical injection. The problem arises from the fact that, when varying the detuning, we quickly move to a region where the CS solution is unstable, leaving the system to return to the homogeneous steady state.

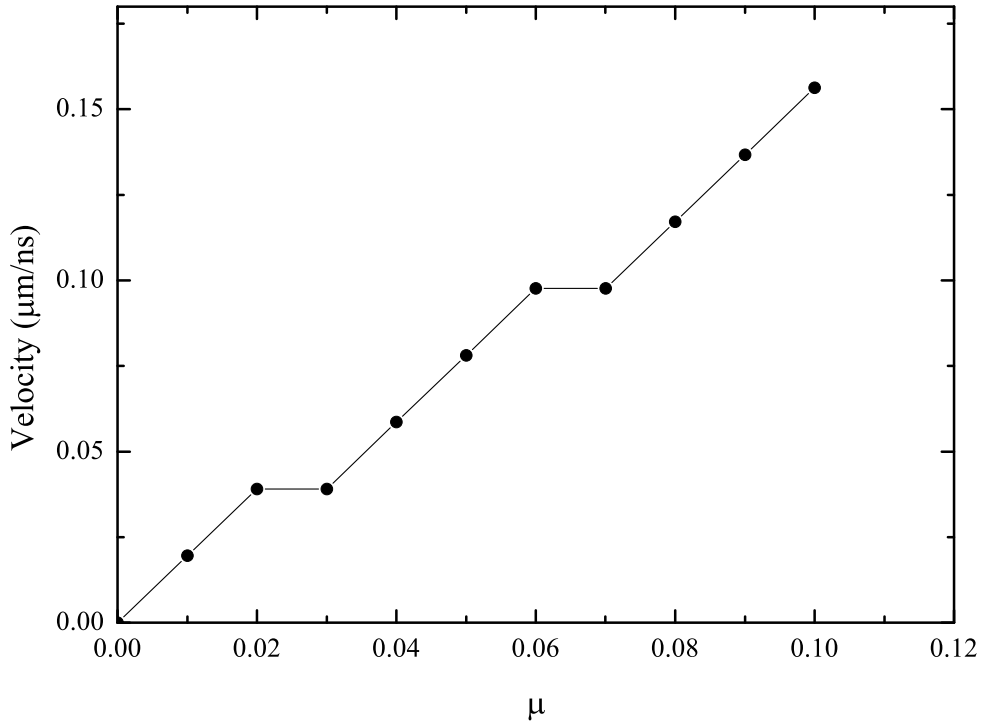

Figure 4.15: Velocity of a CS induced by a detuning modulation of the VCSEL. The velocity is shown as a function of the amplitude of the detuning modulation, μ. For this, the wave vector of the modulation is fixed at $k = 0.036$ and all other parameters are those of figure 3.5

4.2.3 Cavity soliton velocity with injected frequency tuning

For simplicity, a linear gradient is introduced to the phase of the injected field by setting $E_I = E_{I0} \exp(iKx)$. As shown in [20, 21], the CS velocity depends linearly on the applied gradient over a large range, and then it saturates. For higher values of K, the moving CS solution becomes unstable, and the homogeneous background state is recovered. As shown in [54], it turns out that the addition of a linear phase gradient in the holding beam generates, after a suitable change of variables, two extra terms in the field equation. The first one transforms the time derivative of the field into a convective derivative as discussed previously,

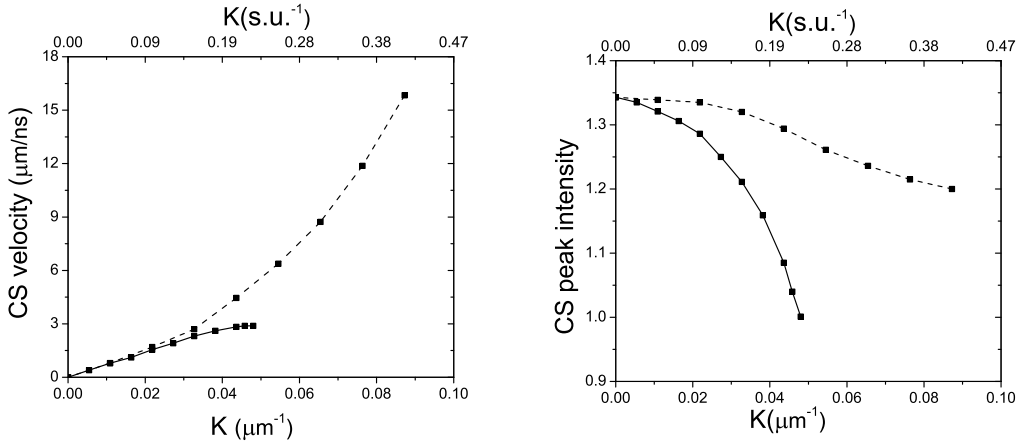

Figure 4.16: CS velocity, (a) and CS peak intensity, (b) as a function of the amplitude K of the phase gradient. Solid (dashed) line: without (with) detuning compensation (see text). Parameters are as figure 3.5.

thus indicating that travelling CS are solutions of the field equation. The second one effectively modifies the value of the cavity detuning parameter θ, according to the following relation:

$$\theta = \theta_0 + aK^2, \tag{4.8}$$

where a is the diffraction parameter. The effect of equation (4.8) is that for large values of K, the correction to the cavity detuning eventually leads to a destabilisation of the travelling CS. This interpretation has been validated in [58], where the existence domain of CS was calculated in the parameter space (θ, K) for the case below threshold. There, it has been shown that the boundaries (in the parameter θ) of the CS existence domain obtained for $K = 0$ change according to the law expressed by equation (4.8) when K is increased. Knowing this, we can progressively adapt the value of the cavity detuning parameter θ when K is increased, in such a way to compensate for the variation introduced in the detuning by the gradient *via* equation (4.8). This amounts to a blue-shift of the injected frequency by a term equal to aK^2/τ_p, where τ_p is the photon lifetime.

We therefore introduced this correction in our numerical simulations and the result is shown in figure 4.16. In figure 4.16 (a) the solid line is the CS velocity as a function of K, for the case without correction: the saturation effect comes into effect quickly and then the curve stops at a gradient amplitude of about $0.0480\mu\text{m}^{-1}$, where, for our choice of the parameters, the CS reaches the velocity of 2.9μm/ns. The dashed line shows the results obtained with the correction to the injected field frequency. First of all, we note that the travelling CS survives

up to values of the gradient amplitude that are on the order of $0.0873\mu\text{m}^{-1}$ (about two times bigger that the case without correction), where the velocity reached by the CS is about 15.8μm/ns (more than 5 time larger than in the case without correction). This is associated with the fact that saturation disappears, also suggesting that the saturation of the CS velocity is an effect due to the variation of the cavity detuning introduced by the gradient according to equation (4.8), and it is not due to the slow dynamics of carriers that cannot follow the field.

As a matter of fact, the correction to the injected frequency modifies the concavity of the curve (see Fig. 4.16 (a)) and the growth rate of the velocity increases, making the process of CS displacement more efficient. In figure 4.16 (b) we show the CS peak intensity as a function of the gradient amplitude K. We observe that for the case without the θ correction (solid line) the peak intensity decreases very rapidly, while for the case with the correction (dashed line) it decreases much slower.

It will therefore be possible to realise an ultra–fast delay line although, as a side effect, we observe a strong deformation in the CS profile at large speeds, as shown in figure 4.17. This fact can be a limiting factor in the rate of encoding information in the line. The deformation consists in the creation of a dip in the intensity plus a tail in the spatial distribution, and a delayed minimum of the carrier distribution that follow the travelling CS (see figure (4.17)). The lag of the population variable is due to its slow dynamics with respect to that of the field and increases with the phase gradient that induces the CS motion. The ultra–fast CS profile presents a strong similarity with the travelling CS profile observed in experiments [20, 59], thus suggesting that observable CS in VCSELs are usually strongly pinned by spatial inhomogeneities of the cavity, so that they effectively move only in the presence of fairly strong gradients.

It is also interesting to look at what happens for higher values of the gradient amplitudes K for the case with the frequency correction. In figure 4.18, we show the 2D transverse profile of the travelling structure (left: field intensity, right: carrier distribution) for $K = 0.1091\mu\text{m}^{-1}$. As soon as the CS starts to move, it develops damped spatial oscillations in its wake. This phenomenon is due to the fact that the carrier dynamics are much slower than that of the field, so the hole in the carrier population that is usually located at the (stationary) CS peak, now lags behind the travelling CS. This phenomenon gives rise to a new intensity peak that in turn creates a new carrier hole and eventually an entire set of travelling filaments in the wake of the CS. It is worth noting that such structure would be unstable in the absence of the phase gradient.

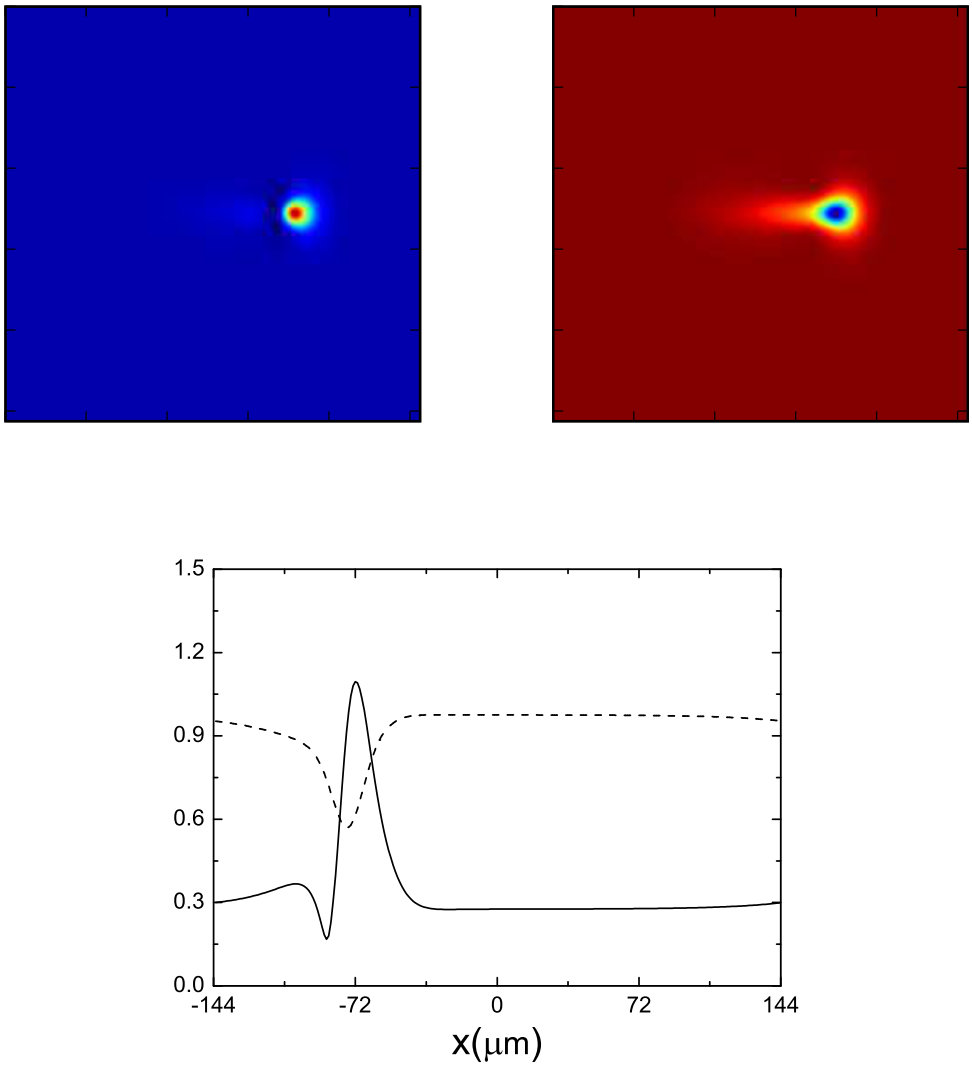

Figure 4.17: Ultra–fast CS profiles. First line: 2D profiles of field intensity (left) and carrier distribution (right). Color scale: blue corresponds to minima and red to maxima. Second line: 1D profile of the field intensity (solid line) and carrier distribution (dashed line). Here the gradient is directed rightwards, $K = 0.08724\mu\text{m}^{-1}$, and the detuning is compensated according to equation (4.8). Other parameters as in figure 3.5.

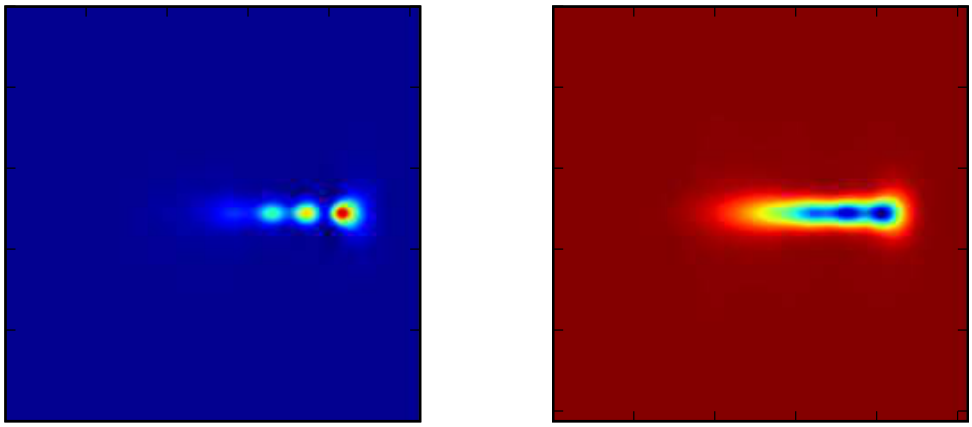

Figure 4.18: 2D profiles of field intensity (left) and carrier distribution (right). Color scale: blue corresponds to minima and red to maxima. Here the gradient is directed rightwards, $K = 0.1091\mu\text{m}^{-1}$, and the detuning is compensated according to equation 4.8. Other parameters as in figure 3.5.

4.3 Motion of cavity solitons in lasers with frequency selective feedback

Due to the absence of the optical injection, to induce motion in the VCSEL with FSF we need to use a method other than the manipulation of injected fields. To achieve this, we suggest using a periodic modulation of the detuning. For convenience, we rewrite the device equations here.

$$\begin{aligned}
\frac{\partial E}{\partial t} &= -\left(1+i\theta\right)E + i\nabla^2 E - i\sigma\left(\alpha+i\right)\left(N-1\right)E + \frac{2\sqrt{T_1}}{\left(T_1+T_2\right)}F \\
\frac{\partial N}{\partial t} &= -\gamma\left[N - J + |E|^2\left(N-1\right)\right] \\
F(t) &= e^{-i\delta\tau_f}\hat{G}\left(t-\frac{\tau_f}{2}\right)\left[-r_1 F\left(t-\tau_f\right) + t_1 E\left(t-\tau_f\right)\right] \\
\hat{G}(t)\left[h(t)\right] &= \frac{r_g}{2\beta}\int_{t-2\beta}^{t} e^{i\Omega_g(t'-t)}h(t')dt'
\end{aligned} \tag{4.9}$$

Where E is the electric field, N the carrier density, F describes the electric field in the external cavity, θ the detuning between the VCSEL frequency and the chosen reference frequency, σ is a coupling constant, α is the linewidth enhancement factor, T_1 and T_2 are the transmittivities of the VCSEL mirrors, J is the current, δ is the detuning between the feedback field and the chosen reference frequency, τ_f is the external cavity round-trip time and r_1 and t_1 are the amplitude reflec-

tion and transmission coefficients of the VCSEL output mirror. The operator $\hat{G}$ describes the frequency selective operation at the volume Bragg grating on the field envelope. Time is scaled to the VCSEL cavity lifetime, and γ is the ratio of the cavity lifetime to the carrier response time. As discussed previously, a periodic modulation allows us to build arrays of CS in a single device. Given the results from the previous section, we suggest using a triangular modulation of the VCSEL detuning, now defined as $\theta(x) = \theta_0 + (2\mu/\pi)\sin^{-1}[sin(kx+\varphi_x)]$, where θ_0 is the background detuning value, μ is the amplitude of the modulation, k is the transverse wavevector and φ_x is an arbitrary phase shift.

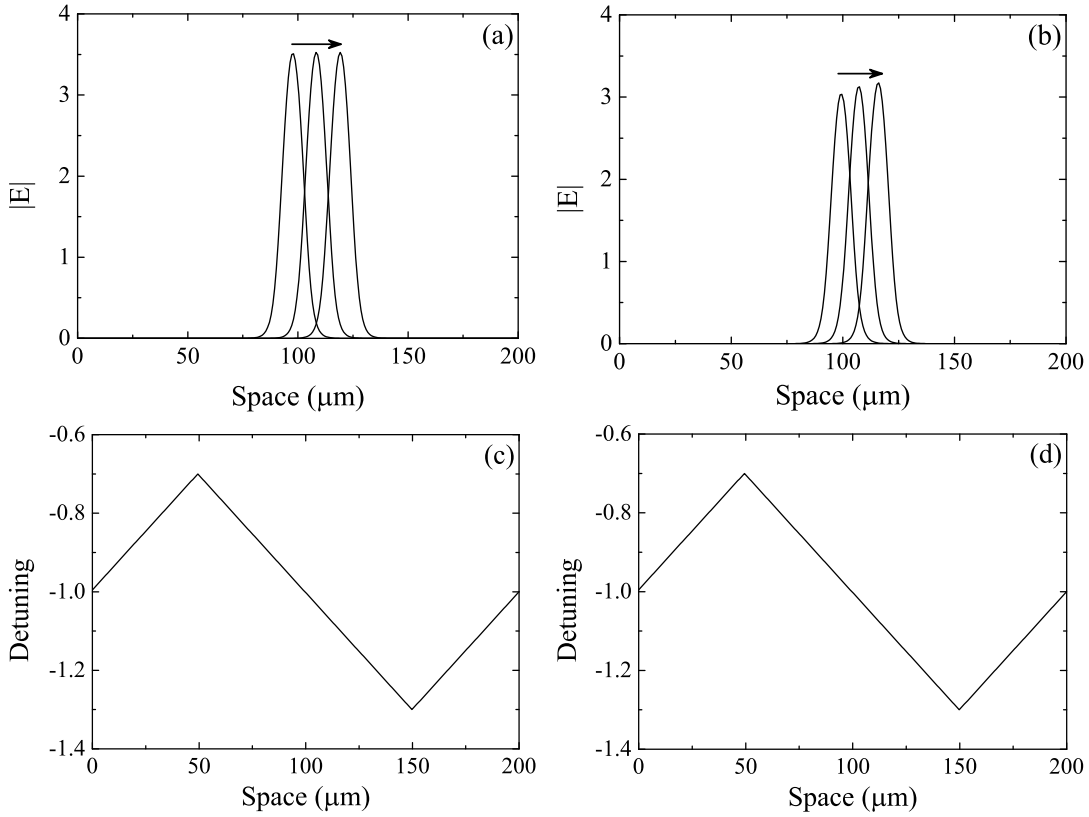

Figure 4.19: Motion of a LCS in the VCSEL with FSF with a triangular modulation of the detuning for $\tau_f = 0.05$ns (a) and $\tau_f = 0.41$ns (b), while (c) and (d) show the respective detuning modulation. The LCS travels towards the modulation minimum with the solid line showing $t = 0$ns, the dashed $t = 49$ns and the dotted $t = 99$ns. Other parameters are as figure 3.9

Figure 4.19 shows the motion of a LCS as it moves towards the minimum of the modulation of the detuning. Presented here are the results from simulations with two different external cavity lengths, which were performed to calculate the velocity of the LCS in the VCSEL with FSF. In figure 4.20, we introduce the velocity of the LCS as a function of modulation amplitude μ, utilising a triangular modulation of the detuning.

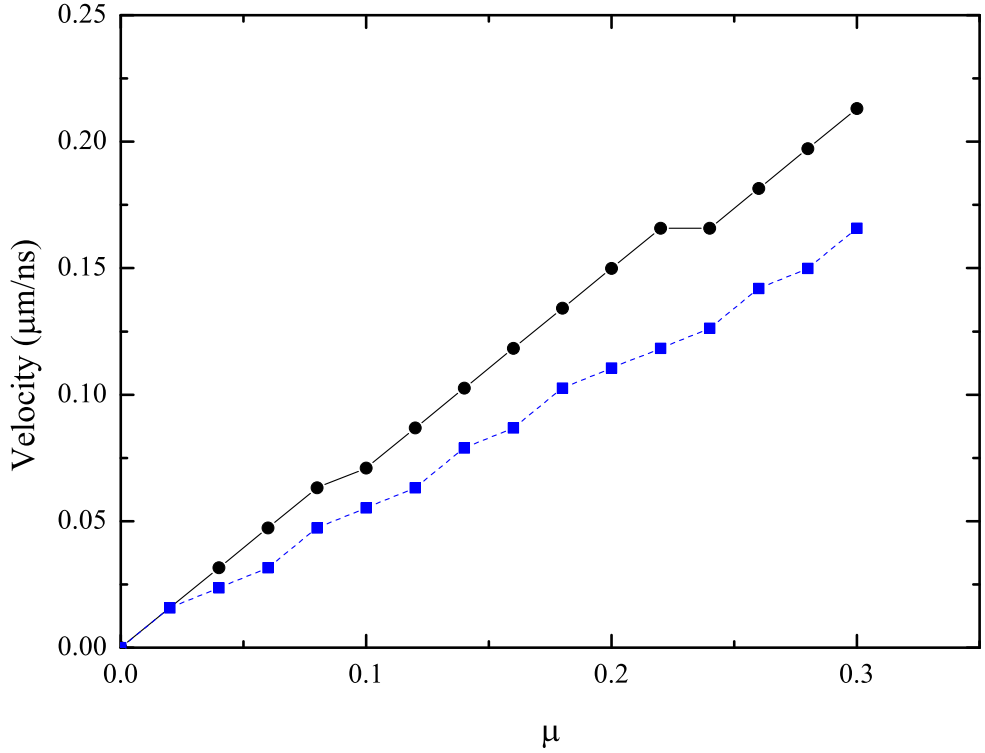

Figure 4.20: Velocity of a LCS in the VCSEL with FSF. The dots represent $\tau_f = 0.05$ns and the squares represent $\tau_f = 0.41$ns.

It is clear from figure 4.20 that changing the length of the external cavity causes the velocity of the LCS to decrease slightly. This is most likely due to a damping effect caused by the delayed feedback. With a longer external cavity, the LCS has time to move further from the central (spatial) region where the feedback is strongest. Further, due to the fact we use detuning gradients to induce motion in the LCS, it is both expected and shown that the range of possible velocities is limited. Figure 4.20 shows the maximum velocity to the point where bistability at the minimum of the modulation is lost. At this point, when the detuning amplitude becomes too large, the modulation minimum enter the region where the patterned solution is stable but the homogeneous solution is not. This results in spontaneous formation of one or more localised structures at the modulation minimum.

4.4 Motion of cavity solitons in Kerr cavities

We now introduce motion of CS in a Kerr cavity by initially considering a linear phase gradient of the optical injection. We first reintroduce the model equation

for convenience:

$$\frac{\partial E}{\partial t} = E_I - (1 + i\theta)E + i|E|^2 E + i\frac{\partial^2}{\partial x^2}E \tag{4.10}$$

where E is the electric field, E_I is the injected field, θ is the detuning and $i\partial^2/\partial x^2$ represents diffraction. The injected field is described by equation (4.11a). We also introduce at this stage a periodic modulation of the optical injection, as described in equation (4.11b). In this case we again restrict ourselves to a triangular phase modulation of the optical injection, as described previously, since this provides a constant gradient and subsequently a constant velocity for fixed parameters.

$$E_I = E_{I0} \exp(iKx) \tag{4.11a}$$

$$E_I = E_{I0} \exp\{i\frac{\mu}{2\pi} \sin^{-1}[sin(kx + \varphi)]\} \tag{4.11b}$$

Here, E_{I0} is the amplitude of the injected field, K is the linear gradient, μ is the amplitude of the modulation, k is the transverse wavevector and φ can represent an arbitrary phase shift of the periodic modulation. In figure 4.21, the velocity of the CS in a Kerr cavity are shown as a function of the phase gradient. This shows a linear relationship between the velocity and the applied phase gradient on which the CS finds itself.

4.5 Conclusions

In this chapter we have investigated methods of inducing motion in CS in photonic devices. It has been demonstrated that, in all three systems of interest, established methods for inducing motion in CS provides the required gradient and indeed induces motion over suitable parameter ranges. Beginning with the VCSEL with optical injection, we have shown that both phase modulations of the optical injection and modulations of the detuning provide very different results. In particular, the range of the amplitudes over which the CS is stable is greatly reduced when considering detuning modulations with respect to the injected phase modulations. This arises from the fact that changing the detuning quickly moves the system to a regime where the CS solution is no longer stable and the system returns to the homogeneous state.

In the VCSEL with FSF, we are unable to induce motions by using phase modulations in the manner described for the VCSEL with optical injection specifically due to the lack of the injected field. We demonstrate that a periodic modulation of the detuning is sufficient to induce CS motion in this system. This method

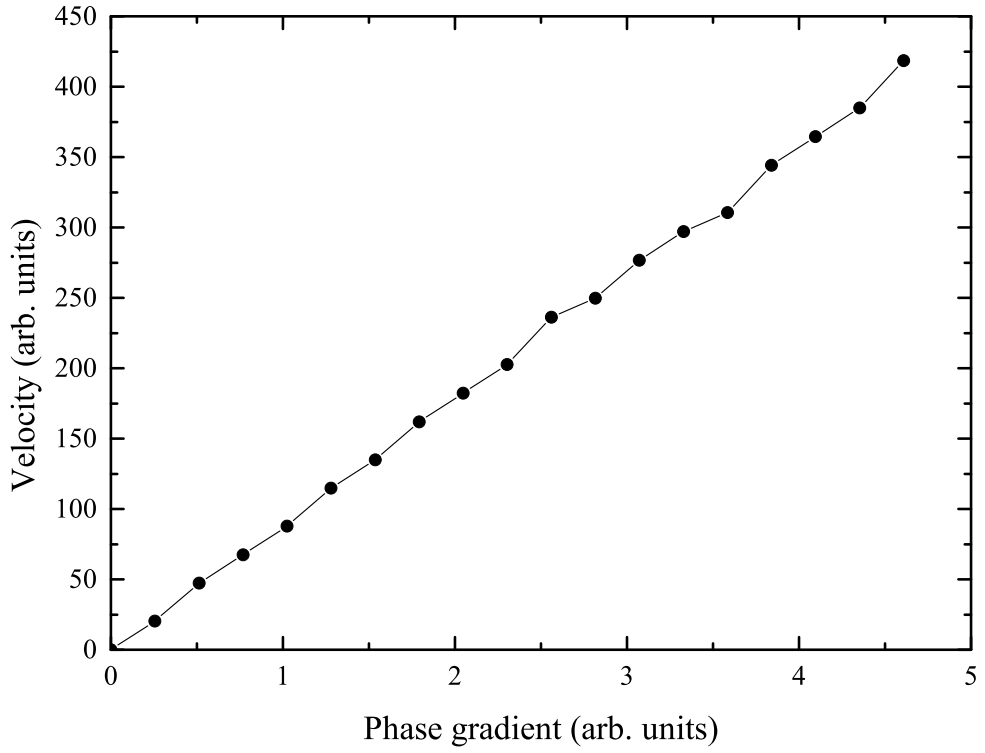

Figure 4.21: Velocity of cavity solitons in a Kerr cavity as a function of the phase gradient applied to the optical injection. Parameters are those of figure 3.16.

produces similar problems to the VCSEL with optical injection when moving to larger gradients. In this case, when the amplitude of the detuning becomes too large, the minimum enters a region where only the patterned state is stable. This results in the spontaneous formation of localised structures at the modulation minima.

Finally, motion of CS in a Kerr cavity is explored using linear phase gradients introduced to the optical injection. In this case, we have not investigated the use of detuning gradients or modulations, as the results of the previous cases show a limited velocity and range of stability when compared to injected phase gradients and modulations. Here we find a linear relationship between the velocity and the applied gradient.

Chapter 5

Cavity soliton interactions in photonic devices

5.1 Introduction

Cavity Solitons (CS) can be switched on and off, at will, by the operator. For this reason, they are excellent candidates for use as elements of an optical memory [22, 26] or an all-optical delay line [20, 21]. In these applications, CS can come into close contact with each other and it is then important to understand how they interact with each other. The aim of this chapter is to investigate CS interactions in simulations of photonic devices based on VCSELs.

We have already seen in the previous chapters that CS possess translational invariance, i.e. they can be positioned in any location of the transverse plane. Laser CS, such as those described in VCSELs with Frequency Selective Feedback (FSF) [29] and VCSELs with saturable absorbers [52], also possess phase invariance. Such invariance is removed in VCSELs with optical injection since the external field breaks the free rotation of the laser phase. We will then first discuss in section 5.2 the interaction of CS in VCSELs with optical injection where there is no phase invariance and where we break the translational invariance by spatially modulating the phase of the injected field. The external modulation forces separate CS to move towards the same region of space and consequently to interact with each other. This case is then contrasted with forced interactions in a simplified Kerr cavity model under the action of a spatially modulated pump in section 5.3. Here we observe some of the CS interaction features described in the VCSEL simulations of section 5.2, such as CS merging, but also CS locking due to the overlap of their modulated tails. In section 5.4, instead we investigate the interactions of CS in models of VCSELs with FSF in the presence of phase

invariance. We first study coupled CS on homogeneous backgrounds and then CS trapped by spatial defects due to imperfections of the growth process of the semiconductor material.

5.2 Forced collisions of cavity solitons in a laser with optical injection

In the VCSEL with optical injection, the nature of forced collisions of two or more CS is introduced. The collisions are enabled by introducing a periodic modulation to the phase of the injected field, as described in section 4.2. By using such periodic modulations, two (or more) CS can be written near a phase maxima, thus inducing motion towards a common point. When the CS collide, the results can be analysed.

Induced collision of diffractive autosolitons have been described in pioneering numerical simulations of systems with two homogeneous states for the implementation of optical adders (not to be confused with optical snaking) [60]. In this case the collision between a larger and smaller autosoliton destabilises the domain walls that connect the two homogeneous states leading to the survival of just one of the colliding solitons [60]. Collisions leading to de-stabilisation of domain walls can also be induced by noise [61]. In the case of CS in VCSELs with optical injection there is no bistability between homogeneous states and no domain walls connecting them. The merging mechanism of CS described here is related to the absorption of energy from the pump and its release in the form of short pulses.

5.2.1 Collisions and merging of cavity solitons in a laser with optical injection

To investigate the mechanism of CS collisions and merging, extensive simulations have been performed of the VCSEL equations:

$$\begin{aligned} \frac{\partial E}{\partial \tau} &= \frac{E_I - i\left(\alpha+\theta\right)E + i\nabla^2 E}{\sqrt{\varepsilon}} + \left(1 - i\alpha\right)WE \\ \frac{\partial W}{\partial \tau} &= \sigma\left[J - \left(1+\sqrt{\varepsilon}W\right)\left(1+|E|^2\right)\right] \end{aligned} \tag{5.1}$$

where E is the electric field, W the rescaled carrier density, E_I the optical injection, α the linewidth enhancement factor, θ the detuning between the optical

injection and the VCSEL and J the pump current. Time is scaled to cavity decay rate ε, with $\sigma = \gamma/\varepsilon^2$, where γ is the decay rate of the carriers. Diffraction is described in two transverse dimensions by the Laplacian operator $\nabla^2 E$ and in one transverse dimension by $\partial_x^2 = (\partial^2/\partial x^2)$.

To induce motion and force collisions, we use a periodic phase modulation of the optical injection, as described in equations 5.2.

$$E_I = E_{I0} \exp[\mu \sin(kx + \varphi_x)] \tag{5.2a}$$

$$E_I = E_{I0} \exp\left\{\frac{2}{\pi}\mu \sin^{-1}\left[sin(k_x + \varphi_x)\right]\right\} \tag{5.2b}$$

$$E_I = E_{I0} \exp\left\{i\frac{2}{\pi}\mu \sin^{-1}\left[\sin(k_x x + \varphi_x)\sin(k_y y + \varphi_y)\right]\right\} \tag{5.2c}$$

Where E_{I0} is the amplitude of the injected field, μ is the amplitude of the phase modulation, k_x and k_y are the transverse wavevector and φ_x and φ_y are an arbitrary phase shift. In figure 5.1 we show the effect of a second CS on an initial CS already positioned at a maximum of the phase modulation. Here we have used a triangular phase modulation, as described in equation (5.2b), of the injected field to induce CS motion as described in the previous chapter of this thesis. A clear merging process takes place at the peak of the modulation.

Simulations over a wide range of the amplitude of the phase modulation, μ, display CS merging at the peak of the phase modulation, as shown in figure 5.1. This occurs even for very small values of μ, corresponding to small spatial gradients and very low velocities of the CS.

When more than two CS are introduced in the VCSEL they all move towards their nearest respective peak of the injected phase modulation and, when two or more meet, they merge to form a single CS (see figure 5.2). CS merging is commonplace in a driven laser system operating above threshold over a wide range of the modulation parameters.

CS merging is also observed in simulations with two transverse dimensions. Figure 5.3 shows an example where two newly written CS move towards their closest maximum of the conical phase modulation (5.2c) in a 2D lattice. When the maximum is empty, the CS is properly positioned. When the maximum is occupied by another CS, merging takes place.

We also note that 1D and 2D CS in VCSELs with optical injection have tails with almost no spatial oscillations. This fact greatly reduces possible mechanisms of the interaction between CS, resulting in the merging of CS described above and in maintaining a constant temporal separation between input pulses during

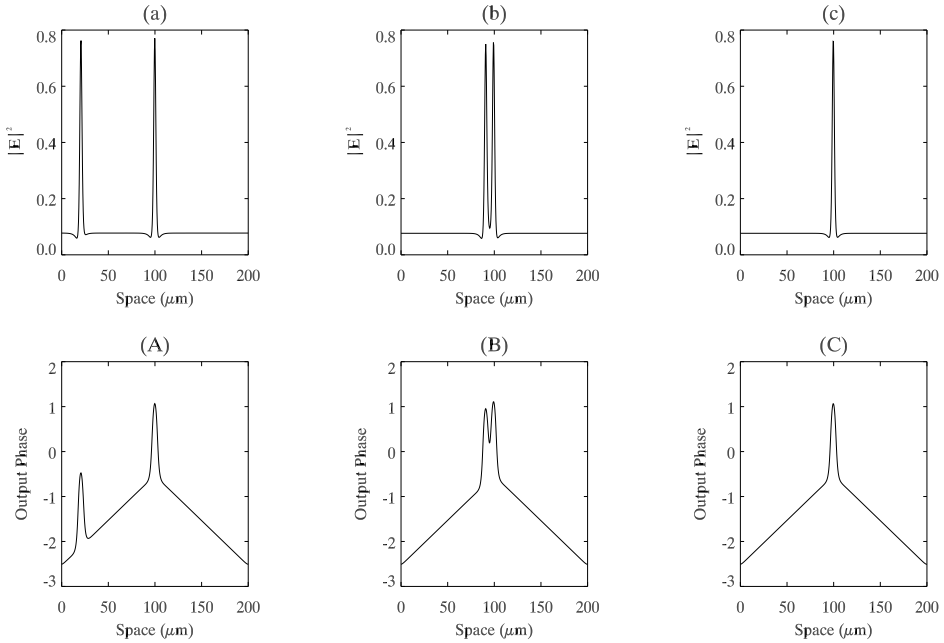

Figure 5.1: Merging of two CS in a VCSEL with triangular phase modulation of the optical injection. Panels (a)-(c) display the spatial profile of the laser intensity while panels (A)-(C) show the phase of the output field. Here $\mu = 1.0$, $k = 0.036$ and the other parameters are those of figure 3.5. (a) and (A) correspond to $t = 0$ns, (b) and (B) correspond to $t = 870$ns, (c) and (C) correspond to $t = 990$ns.

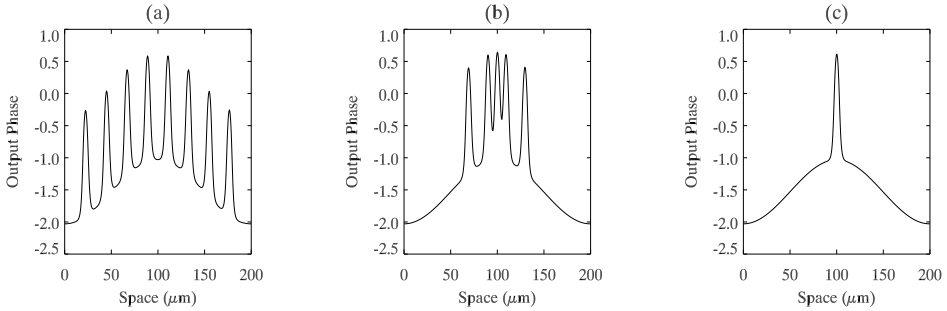

Figure 5.2: Merging of eight CS in a VCSEL with sinusoidal phase modulation of the optical injection. The phase of the output field is plotted versus the transverse spatial coordinate. Here the phase modulation of the injected field corresponds to $\mu = 0.5$, $k = 0.036$ and is switched on after a comb of eight equally spaced CS has been initiated. The other parameters are those of figure 3.5. (a) corresponds to $t = 0$ns, (b) corresponds to $t \approx 838$ns and (c) corresponds to $t \approx 2488$ns.

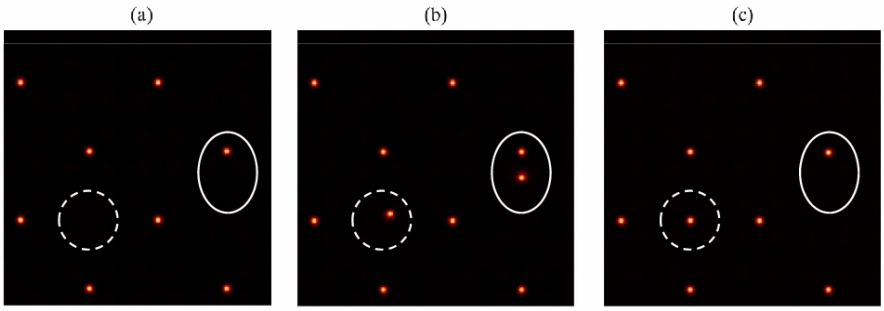

Figure 5.3: Motion and merging of CS in a VCSEL with phase modulation of the optical injection in 2D given by equation (4.6). Panel (a) shows the stationary 2D distribution of the output intensity before the writing of two new CS, (b) shows the distribution immediately after the writing of the two CS and (c) after $t = 27.5$ns from the writing of the two new CS. The CS in the dashed circle moves to the closest maximum of the modulation while the CS in the solid oval merges with a CS at the peak of the phase modulation.

their motion. Both effects are beneficial for the implementation of applications in optical information processing such as delay lines and optical memories.

5.2.2 Energy balance in lasers with optical injection during cavity soliton merging processes

The process of merging of dissipative spatial solitons is quite intriguing and deserves special attention. For example, spatial soliton merging is impossible in conservative systems where travelling solitons are well known to pass through each other unchanged. Merging of CS is then intrinsically related to their dissipative nature. Here we demonstrate that during merging there is the emission of light pulses accompanied by the violation of the energy balance in the system.

Energy balance has been studied in systems based on the complex Ginzburg-Landau equation. In particular, this phenomenon is described in [62], where the energy flow is described for the system as

$$\frac{\partial \rho}{\partial z} + \frac{\partial j}{\partial t} = P \tag{5.3}$$

where ρ is the energy density, $\rho = |\varphi|^2$, and φ is the field variable. The corresponding flux, j, is

$$j = \frac{i}{2}(\varphi\varphi_t^* - \varphi_t\varphi^*) \tag{5.4}$$

and the density of energy generation, P, can be derived from the model equation.

We now adapt this concept to our model, derive the energy balance equations and examine the energy flow in our system.

We consider first the simpler case of laser CS without dynamical contributions of the carrier population. By setting the population variable D to its equilibrium value, one obtains:

$$\frac{\partial E}{\partial \tau} = E_I - i\,(\theta + \alpha)\,E + i\partial_x^2 E + (1 - i\alpha)\,(D - 1)\,E \tag{5.5a}$$

$$D = \frac{J}{1 + |E|^2} \tag{5.5b}$$

where $\tau = \varepsilon t$. In analogy with the cubic-quintic Ginzburg-Landau equation [62], we introduce a continuity equation for the field E:

$$\frac{\partial \rho}{\partial t} + \frac{\partial j}{\partial x} = Q \tag{5.6}$$

where the density is $\rho = |E|^2$ and the current is $j = i(E\partial_x E^* - E^*\partial_x E)$. For conservative systems the quantity Q is identically zero. For injected and dissipative systems like (5.5) however we can write:

$$Q = 2\left[\mathrm{Re}\,(E_I E^*) + D|E|^2 - |E|^2\right] \tag{5.7}$$

The three contributions that form Q are identified as the energy provided by the external injection, the energy stored in the material by the laser pumping, J, and the losses at the laser output, respectively. Q is trivially equal to zero for homogeneous steady states while the spatial part $\partial_x j$ counterbalances Q locally for stationary CS. In this last case, however, the integration over the full transverse space of Q (as well as $\partial_x j$) is identically zero and one talks of 'energy balance' across the full profile of a CS.

We find that the energy balance for $\int Q\,dx$ persists in the case of CS moving on phase gradients. At the moment of the merging, however, clear violations appear. Figure 5.4 shows the time evolution of the energy balance before and after a CS merging event for the single equation model (5.5). Balance takes place both during the motion of one CS towards the second and after the collision event. Around the merging time, however, energy exchanges are clearly not balanced. Initially excess energy is absorbed from the injection to be later released through cavity losses. Note that this excess energy is not stored in the carrier distribution but is instead emitted from the VCSEL in the form of a short pulse, as shown in the inset of Figure 5.4.

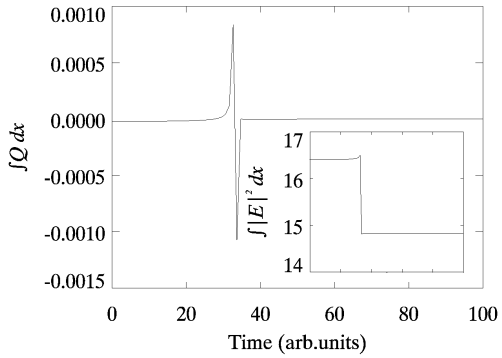

Figure 5.4: Time evolution of the energy balance $\int Q\,dx$ for the merging of two CS in the model (5.5). Inset: cavity losses $\int |E|^2 dx$ as a function of time (with scale as in the main image). Parameters are those of figure 3.5. Triangular modulation parameters are $\mu = 0.1$ and $k = 0.036$.

The physical description of CS merging in model (5.1) is more complicated due to the delayed dynamics of the carriers. When we take this into account, the density term in the continuity equation (5.6) becomes $\rho = |E|^2 - D^2$ while the current term, $j = i(E\partial_x E^* - E^*\partial_x E)$, is unchanged. There is a simple explanation for the negative sign in front of the carrier term, D^2, in the definition of ρ: in contrast with the peak of the field intensity, the carrier distribution has a trough at the center of the CS (see Figure 3.5 (c)). This means, for example, that field dissipations are larger at the centre of the CS while the carrier dissipations are reduced in the same place due to inhibited spontaneous emission. For equations (5.1) the definition of Q then has to be updated to:

$$\begin{aligned} &\frac{\partial(|E|^2 - D^2)}{\partial t} + \frac{\partial j}{\partial x} = \hat{Q} \\ &= 2\left\{\mathrm{Re}\left(E_I E^*\right) + (D-1)\,|E|^2 + \sigma\left[D\left(1 + |E|^2\right) - J\right]\right\} \end{aligned} \tag{5.8}$$

The addition of the carrier dynamics corresponds to the term multiplied by σ in the definition of $\hat{Q}$. Again $\hat{Q}$ is identically equal to zero for homogeneous steady states while $\int \hat{Q}\,dx = 0$ for a stationary CS due to energy balance. Figure 5.5 (a) shows the time evolution of the quantity $\int Q\,dx$ with Q from equation (5.7), i.e. without the carrier dynamics term, before and after a CS merging event for the model (5.1). The inclusion of the carrier dynamics in the definition of $\hat{Q}$ ensures balance during the motion of one CS towards the second (see the comparison between Figures 5.5 (a) and (b)). As in the previous case, energy exchanges are clearly not balanced around the merging of CS since excess energy is first

absorbed from the injection and later released through cavity losses. Again, the excess energy is emitted from the VCSEL in the form of light pulses, as shown in the inset of Figure 5.5 (b).

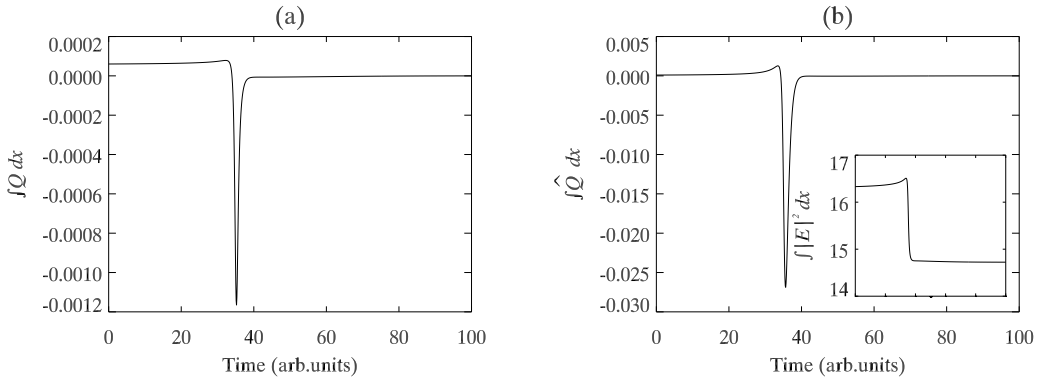

Figure 5.5: Time evolution of (a) the quantity $\int Q\,dx$ without the carrier density dynamics and (b) $\int \hat{Q}\,dx$ with the carrier density dynamics for the merging of two CS in the model (5.1). Inset: cavity losses $\int |E|^2 dx$ as a function of time (with the scale as in the main image). Parameters are those of figure 3.5. Triangular modulation parameters are $\mu = 1.0$ and $k = 0.036$.

5.3 Merging and locking of cavity solitons in a Kerr cavity

At difference from what we have observed in the model of a VCSEL with injected signal, forced collisions of CS in a Kerr cavity can take two forms. They can either lock together, becoming a multi-peaked CS structure, or they can merge, as described previously in section 5.2. There are also regions where locking and merging co-exist. We begin by rewriting the model equations, for convenience:

$$\frac{\partial E}{\partial t} = E_I - (1 + i\theta)E + i|E|^2 E + i\frac{\partial^2}{\partial x^2}E \tag{5.9}$$

where E is the field, E_I is the injected field, θ is the detuning and $i(\partial^2/\partial x^2)E$ is diffraction. Here, we detail the effects of varying the phase gradient applied to the CS by varying the amplitude of a triangular phase modulation, as described in equation 5.10.

$$E_I = E_{I0} \exp\left\{\frac{2}{\pi}\mu \sin^{-1}\left[\sin(kx + \varphi)\right]\right\} \tag{5.10}$$

Where E_{I0} is the amplitude of the injected field, μ is the amplitude of the phase modulation, k is the transverse wavevector and φ is an arbitrary phase shift.

It is important to note that the shape of the CS in the Kerr cavity differs from that of the VCSEL with optical injection. In particular, the CS in VCSELs have very short tails with no spatial modulations. In contrast, the CS in a Kerr cavity have longer tails with distinct spatial modulations (see, for example, figure 3.16).

5.3.1 Merging and locking of cavity solitons in a Kerr cavity

By varying the applied phase gradient, we can control the nature of the interaction between two CS in a Kerr cavity. Using this control parameter, a region of locking and merging is mapped, along with regions where merging and locking co-exist. The modulation is provided by equation (5.10), and figure 5.6 shows an example of the initial conditions used for the collisions.

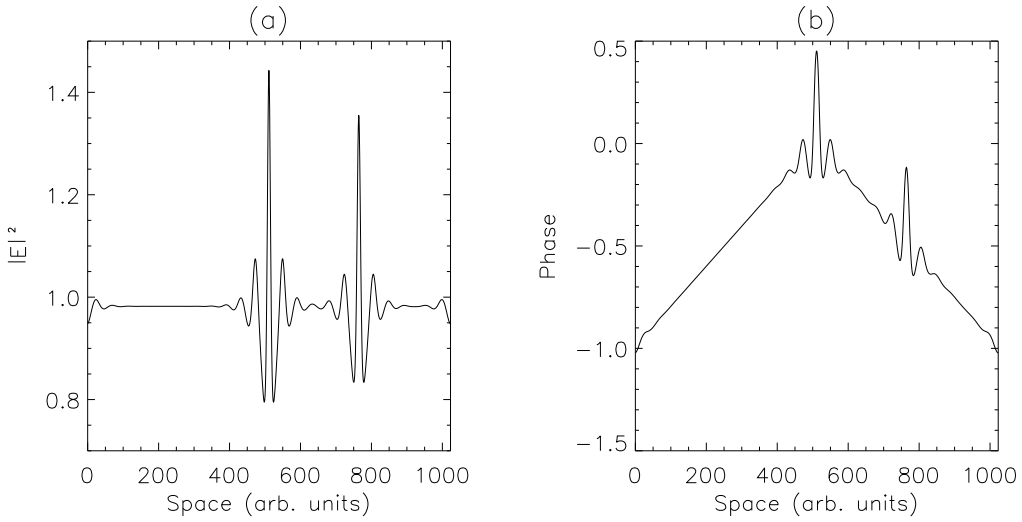

Figure 5.6: The initial conditions used to force collisions between CS. In this case, an additional CS is introduced to the right of the phase maximum. Panel (a) shows the intensity profile of the system while (b) shows the output phase. Parameters are those of figure 3.16.

We start with low values of the injected phase amplitude, μ, and gradually increase the amplitude. Initially, a CS is introduced to the left of the maximum shown in figure 5.6. We find three distinct behaviours, accompanied by a small region where CS writing was impossible. Examples of the three behaviours are shown in figure 5.7. In the range $0.05 \leq \mu < 0.25$, the second CS locks with the CS at the peak of the phase modulation. In the range $0.25 \leq \mu < 0.40$,

we observe a region of both merging and locking. The merging and locking phenomenon occurs when the cavity soliton locks with a multi-peaked structure at the phase maximum. As the cavity soliton locks, one of the peaks which formed the original structure is absorbed. This is most likely due to the number of peaks in the structure at the phase maximum becoming unstable when the additional CS locks with the structure at the peak.

When the phase gradient is increased to the range $0.41 \leq \mu < 0.60$ we observe a bifurcation when the behaviour switches to purely merging. As described for the case of the laser with optical injection, the CS drifts up the phase gradient and merges with the structure at the peak. Meanwhile, if the phase gradient is further increased to the range $0.60 \leq \mu < 0.77$, the behaviour of the interaction switches from pure merging back to a region where both locking and merging are present. In this case, a three peaked symmetric structure is observed after the collision.

It is important to note that, for the range of phase gradient $0.77 \leq \mu < 0.79$, it is impossible to write an additional CS. This is most likely due to the system being only being able to switch to an unstable soliton branch, rather than a stable solution. However for larger gradients, the writing process allows for switching to a stable solution again. In the range $0.79 \leq \mu < 0.85$ we find a region of pure merging. This is followed by the range $0.85 \leq \mu \leq 0.90$ where the behaviour switches back to pure locking once again. Figure 5.8 (a) shows the mapping of these behaviours as the phase amplitude increases.

When an additional CS is introduced to the right of the phase maxima, we observe similar behaviour to that described for an additional CS introduced on the left. There are some differences though. For the range $0.35 \leq \mu < 0.41$, we observe a switch from the merging and locking behaviour to pure locking. In the range $0.43 \leq \mu < 0.48$ we observe a shift from pure merging to locking and merging before a shift back to pure merging for the range $0.48 \leq \mu < 0.77$. Note that we do not see any change from pure merging at $\mu = 0.60$, as observed when an additional CS is introduced on the left.

Again, a region where the creation of an additional CS becomes impossible is observed for the range $0.77 \leq \mu < 0.80$. This is followed directly by pure locking, with no intermediate merging behaviour, in the range $0.80 \leq \mu \leq 0.90$. In figure 5.8 (b), we show how the behaviour of the interaction changes as the phase gradient, μ, increases for this case.

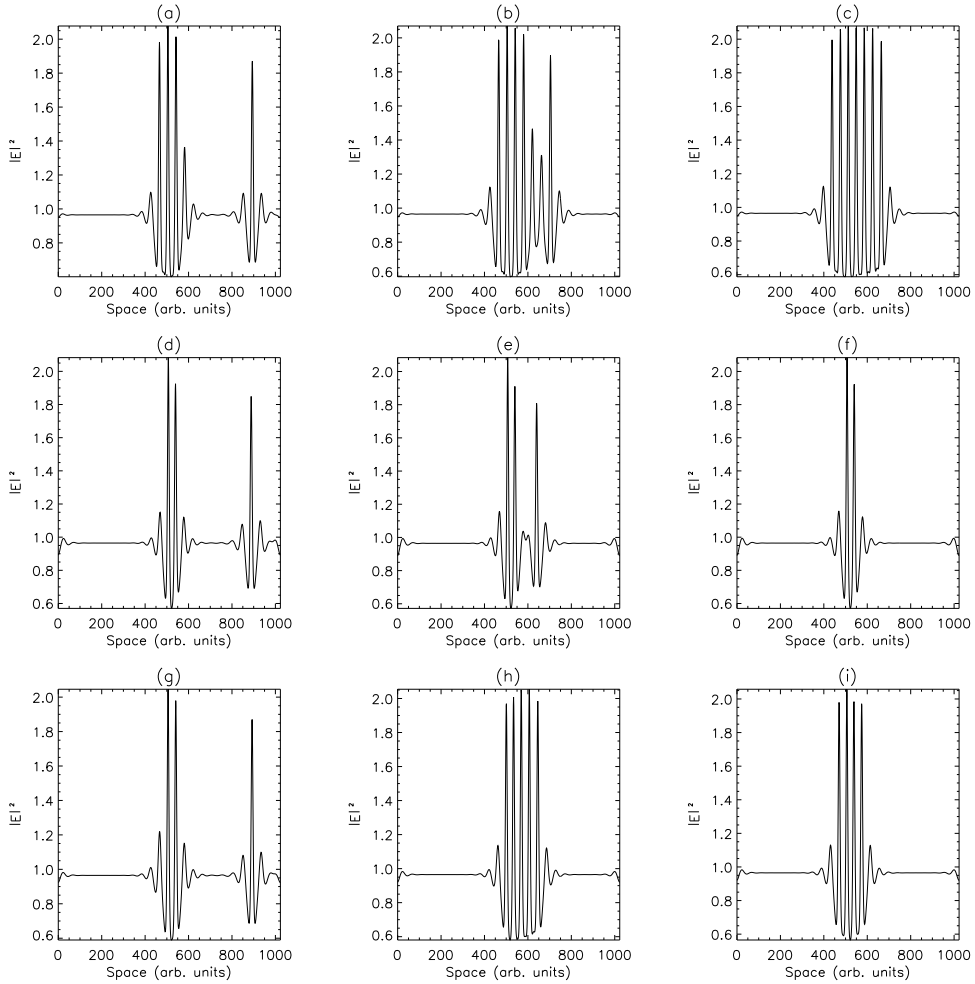

Figure 5.7: Example of the three behaviours observed during CS interaction. The first line (a) - (c) shows locking with a phase amplitude $\mu = 0.2$. A second CS is introduced in (a), at time $t = 0$, travelling towards the peak, with (b) ($t = 10740$) and (c) ($t = 15000$) showing the locking process. In (d) - (f) we show merging with a phase amplitude $\mu = 0.6$. A second CS introduced in (d) at time $t = 0$ moving towards the peak and (e) ($t = 2400$) and (f) ($t = 7980$) showing the merging process. Finally, in (g) - (i) we show the peculiar locking and merging phase with phase amplitude $\mu = 0.3$. A second CS introduced in (g), at time $t = 0$, moving towards the peak and (h) ($t = 4800$) and (i) ($t = 9000$) showing the combined locking and merging process. Other parameters are as figure 3.16.

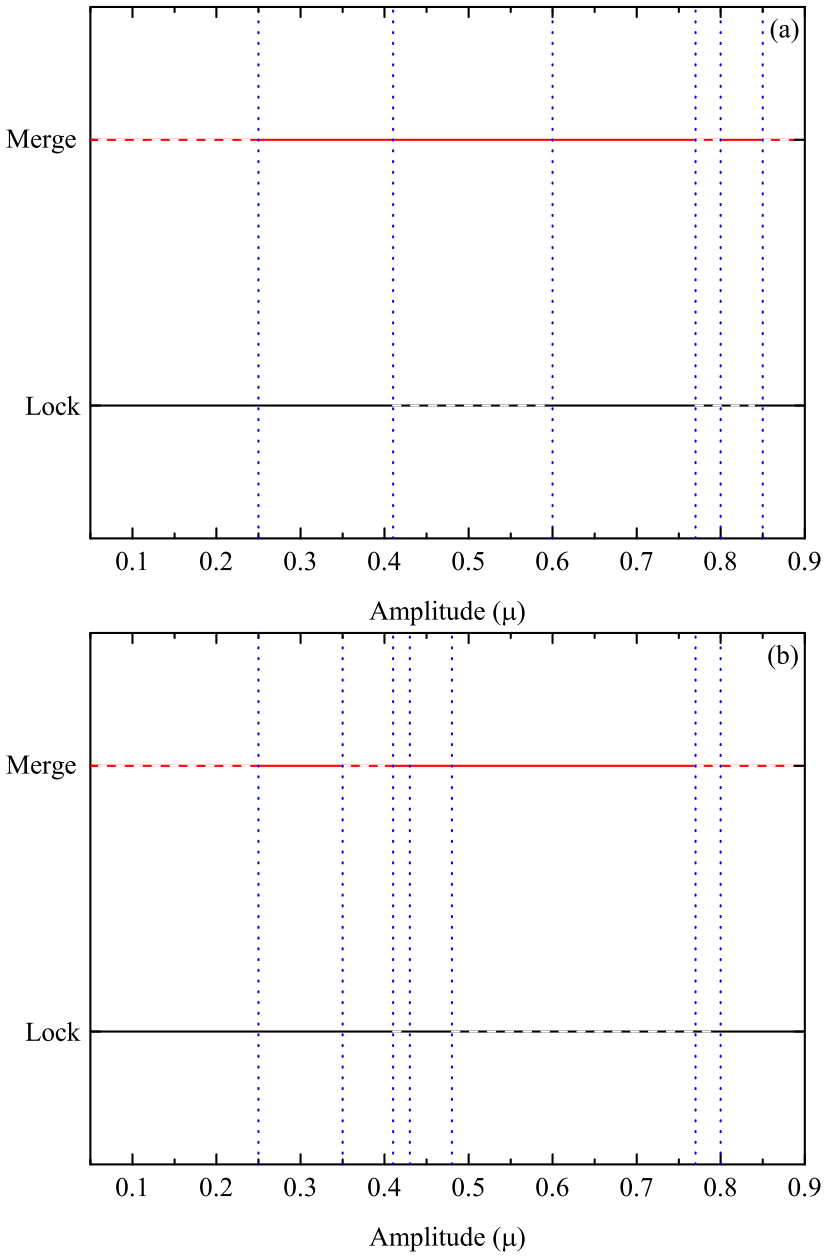

Figure 5.8: Behaviour of the interaction when an additional CS is introduced and forced to collide with the structure at the peak of a phase gradient, as the amplitude of the phase gradient (μ) increases. (a) The behaviour when an additional CS is introduced to the left of the phase maxima while (b) shows the behaviour when an additional CS is introduced to the right of the phase maxima.

5.3.2 Energy balance in a Kerr cavity during cavity soliton merging and locking processes

We now examine the energy flow in the Kerr cavity during CS collisions. A similar process to that sketched in section 5.2 is used. Obviously, the energy continuity equations are much simpler when applied to the model of the Kerr cavity. We re-introduce the continuity equation for simplicity:

$$\frac{\partial \rho}{\partial t} + \frac{\partial j}{\partial x} = Q \tag{5.11}$$

where the density is $\rho = |E|^2$ and the current is $j = i(E\partial_x E^* - E^*\partial_x E)$. For the case of the Kerr cavity, we can write:

$$Q = 2\left[\mathrm{Re}(E_I E^*) - |E|^2\right] \tag{5.12}$$

In this case, we have a two contributions to the value Q. These are identified as the energy input from the external injection and the energy losses at the output mirror. Again, Q is trivially zero for homogeneous steady states while the spatial part $\partial_x j$ counterbalances Q locally for stationary CS. When integrated over the full transverse space, Q (as well as $\partial_x j$) is identically zero and we can show 'energy balance' across the full profile of a CS in the Kerr cavity.

Similar to the case of the laser with optical injection, we find that energy balance persists for $\int Q\,dx$ in the case of CS moving on phase gradients. However as the CS interact with the structure at the peak, violations of the energy balance occur. For the case of locking, as shown in figure 5.9, the energy is balanced with $\int Q\,dx \approx 0$ before and after the interaction. Since these changes in the energy balance are very small, figure 5.9 displays background fluctuations due to numerical error. By decreasing the time step, the amplitude of these fluctuations decreases but obviously the numerical error cannot be completely eliminated. However, as the peak of the moving CS interacts with the tail of the stationary structure at the peak, there is a clear violation as energy in the system increases before decreasing as a pulse of light is emitted. It should be noted that, in contrast to the laser with injection, the Kerr cavity has no carrier distribution in which to store extra energy so there is clearly no question as to what happens to the extra energy.

For the case of full CS merging, we present the time evolution of the energy balance in figure 5.10. Again, energy is balanced before and after the interaction with $\int Q\,dx \approx 0$, but with large violations during the merging process. We first

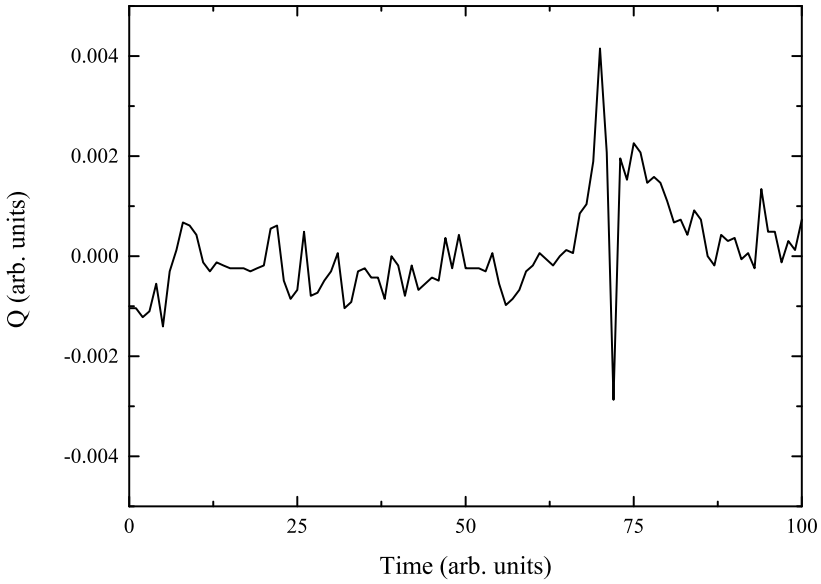

Figure 5.9: Energy balance before, during and after a locking interaction between two CS in a Kerr cavity. Before and after the interaction, the energy is balanced with $\int Q \approx 0$. During the process there is a brief increase in energy before the excess energy is released as a pulse.

see a smaller violation as the two tails interact, followed by a larger violation as the peaks interact with the tails. Finally, a larger violation occurs as the peak of the moving CS merges with the peak of the structure at the maxima.

5.4 Cavity soliton interactions in a laser with frequency selective feedback

Interactions between Laser Cavity Solitons (LCS) in the VCSEL with frequency-selective feedback are decidedly more complicated than those of the VCSEL with optical injection. The complications arise from the freedom of the individual LCS to choose their own frequency and phase, unlike the LCS in the previous systems which are locked to the frequency and phase of the injected field. Here we examine the effects of introducing two or more LCS into our system and examine their

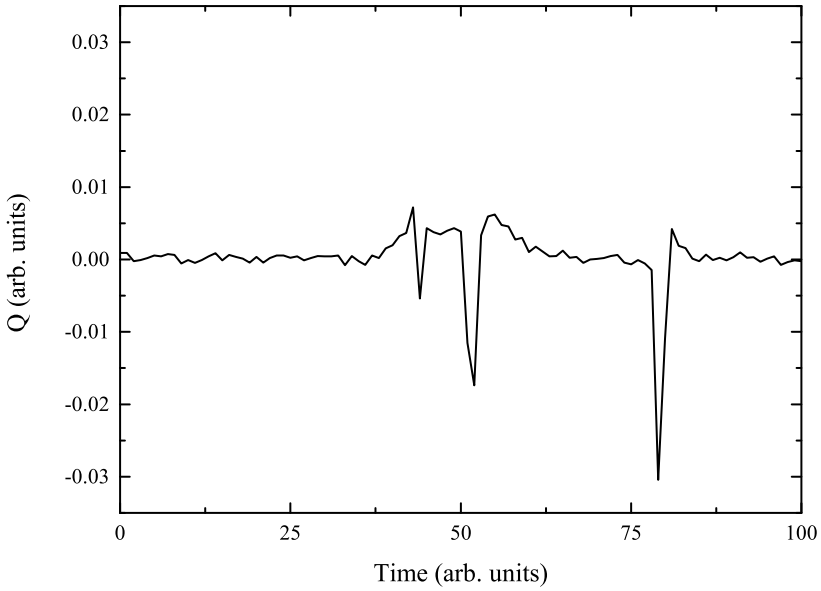

Figure 5.10: Energy balance before, during and after a merging interaction between two CS in a Kerr cavity. Before and after the interaction, the energy is balanced with $\int Q \approx 0$. During the process there are three brief violations, the first as the tails interact with each other, the second as the peaks interact with the tails and the third as the peaks merge.

effects on each other. For convenience, we reproduce the model equations here.

$$\begin{aligned}
\frac{\partial E}{\partial t} &= -\left(1+i\theta\right)E + i\nabla^2 E - i\sigma\left(\alpha+i\right)\left(N-1\right)E + \frac{2\sqrt{T_1}}{\left(T_1+T_2\right)}F \\
\frac{\partial N}{\partial t} &= -\gamma\left[N - J + |E|^2\left(N-1\right)\right] \\
F(t) &= e^{-i\delta\tau_f}\hat{G}\left(t-\frac{\tau_f}{2}\right)\left[-r_1 F\left(t-\tau_f\right) + t_1 E\left(t-\tau_f\right)\right] \\
\hat{G}(t)[h(t)] &= \frac{r_g}{2\beta}\int_{t-2\beta}^{t} e^{i\Omega_g(t'-t)}h(t')dt'
\end{aligned} \tag{5.13}$$

Where E is the electric field, N the carrier density, F describes the electric field in the external cavity, θ the detuning between the VCSEL frequency and the chosen reference frequency, σ is a coupling constant, α is the linewidth enhancement factor, T_1 and T_2 are the transmittivities of the VCSEL mirrors, J is the current, δ is the detuning between the feedback field and the chosen reference frequency, τ_f is the external cavity round-trip time and r_1 and t_1 are the amplitude reflection and transmission coefficients of the VCSEL output mirror. The operator $\hat{G}$ describes the frequency selective operation at the volume Bragg grating on the field envelope. Time is scaled to the VCSEL cavity lifetime, and γ is the ratio of the cavity lifetime to the carrier response time.

For the purpose of applications such as delay lines and optical memories, it is important to understand how multiple LCS interact. In [63], an analysis of multi-soliton solutions is performed in the quintic complex Ginzburg-Landau equation. The equation modelled takes the form of

$$i\delta\varphi = i\varphi_\xi + \left(\frac{D}{2} - i\beta\right)\varphi_{\tau\tau} + (1 - i\varepsilon)\,|\varphi|^2\varphi + (\nu - i\mu)|\varphi|^4\varphi \tag{5.14}$$

where τ is the retarded time, ξ is the propagation distance, δ, β, ε, μ and ν are real constants, φ is a complex field and D, which can be set to either $D = \pm 1$, is set to $D = 1$ representing the self focusing regime. Here the distance between the solitons, ρ, and their phase difference, Φ is defined in terms of energy (Q) and momentum (M) balance equations. Since the gain and losses of the system must be balanced for the existence of dissipative solitons, the rate of change of these variables becomes

$$F(\Phi) = \frac{d}{d\xi}Q = 0 \quad J(\Phi) = \frac{d}{d\xi}M = 0 \tag{5.15}$$

i.e. the rate of change of the energy and momentum should be zero. The results predict that, for $\varepsilon = 1.8$, with the other parameters defined as $\delta = -0.01$, $\beta = 0.5$, $\mu = -0.05$ and $\nu = 0$, two stable points exist in phase difference and separation at $\Phi = \pi/2$, where the zero solutions of the energy balance and momentum balance equations intersect, while for $\varepsilon = 0.4$ no stable solutions exist. Also presented is the existence of saddles, which are attractive spatially and repulsive in terms of the phase difference or repulsive spatially and attractive in terms of the phase difference, which fall on the intersection between the zeroes of the energy balance and the $\Phi = 0$ and $\Phi = \pi$ plane. Numerical results support these predictions, with one of three behaviours, detailed below and shown in figure 5.11.

1. The phase difference is attracted to $\Phi = 0$ and attracted by the second saddle (S_2 in figure 5.11) and repulsed by the saddle (S_3), in which case the solitons are attracted to each other and merge.

2. The phase difference is attracted to a fixed stable position and phase difference at $\Phi = \pi/2$. In this case, the separation and phase difference oscillate while approaching the fixed point, as shown by points F_1 and F_2 in figure 5.11 (a) only.

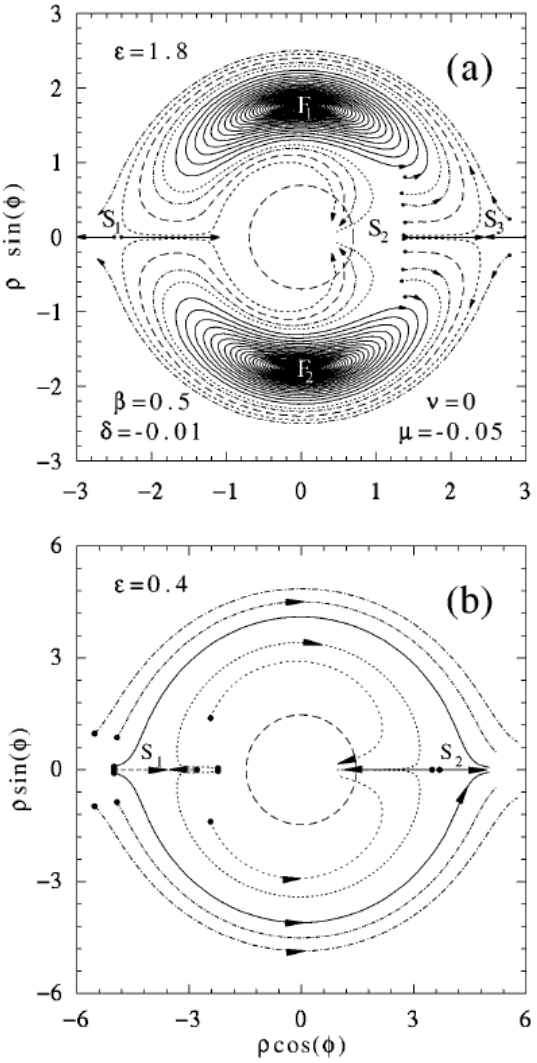

Figure 5.11: Trajectories showing the evolution of two-soliton solutions on the interaction plane for the parameters given in (a). The saddles are denoted by $S_{1,2,3}$, as appropriate, and the stable solution is denoted by $F_{1,2}$. The radius of the dashed circle in the centre represents the full width half maximum width of the soliton and, within this circle, solitons merge. Figure reproduced from [63].

3. The phase difference is attracted to $\Phi = \pi$ and repulsed at the first saddle (S_1). Here, once the soliton reaches the $\Phi = \pi$ locked state, they repulse each other, moving further apart.

In general, this means one of two behaviours between two or more interacting LCS in our systems. The first, when the phase difference between them is 0, allows the LCS to attract. The second, when the phase difference is π, allows the LCS to repel each other. It should be noted that the second is not possible in the driven systems, such as the laser with optical injection as the phase in these systems is fixed to that of the holding beam.

5.4.1 Cavity soliton interactions on a homogeneous background

When two LCS are written in our VCSEL with FSF, their frequencies and phases interact over larger distances than experienced in the VCSEL with optical injection. Again, because the frequency and phase of the LCS in the VCSEL with optical injection are fixed to that of the input, the frequency and phase of each individual cavity soliton is always identical. The phase is locked with 0 phase difference, and the frequency of each is locked to that of the injected field. This is not the case in the VCSEL with FSF, where the LCS are free to choose their own frequency and phase, which can be independent to that of the neighbouring laser cavity soliton.

Simulations of the complex Ginzburg Landau equations predict that interactions of two solitons will result in their spiralling slowly to fixed relative distances L, with a phase difference $\Phi = \varphi_2 - \varphi_1 = \pi/2$ unless merging takes place [64, 65]. Φ equal to zero and π states are also possible but correspond to saddles that are either phase or distance unstable [66]. Analytically, the attainment of a bound state reduces to the analysis of two transcendental equations in the (L, Φ) phase space. This situation is very similar to that described in [63, 67, 68].

In contrast LCS in our model of a VCSEL with frequency selective feedback, which is designed to better represent the experimental setup than the more generic complex Ginzburg Landau models, does not predict $\Phi = \pi/2$ locked states. Theoretically, the interaction of two phase-chirped LCS should lead to a phase locked state with a frequency difference close to $\pi/2$ in a way similar to what is observed in temporal-longitudinal systems [40]. The reality of VCSELs with frequency-selective feedbacks is however quite different from this scenario. First, realistic values of the linewidth enhancement factor α strongly reduce the

laser cavity soliton phase chirp making it impossible to observe the $\pi/2$ locking even on homogeneous backgrounds. Secondly and more importantly, LCS in real systems are pinned to local defects that are due to the growth process of the semiconductor material.

Our model and chosen parameters predict that only the $\Phi = \pi$ state is phase stable. Our model also predicts that possibly the $\Phi = 0$ phase state may be stable for larger distances, although simulations to find states at such distances are very time consuming and this is therefore not a state we have been able to observe. The two LCS, once locked at $\Phi = \pi$ slowly begin to repel each other and motion is induced pushing the two LCS apart. Simulations have been performed for considerable lengths of time and the velocity induced by the repulsion of the LCS slowly decreases until the LCS are essentially stationary with no further interactions. Figure 5.12 shows the quick evolution of the phase, followed by the slow dynamics of the motion, for $\alpha = 9.0$ and $\alpha = 5.0$. Also shown is a prediction for the point where the phase locking would change from $\Phi = \pi$ to $\Phi = 0$.

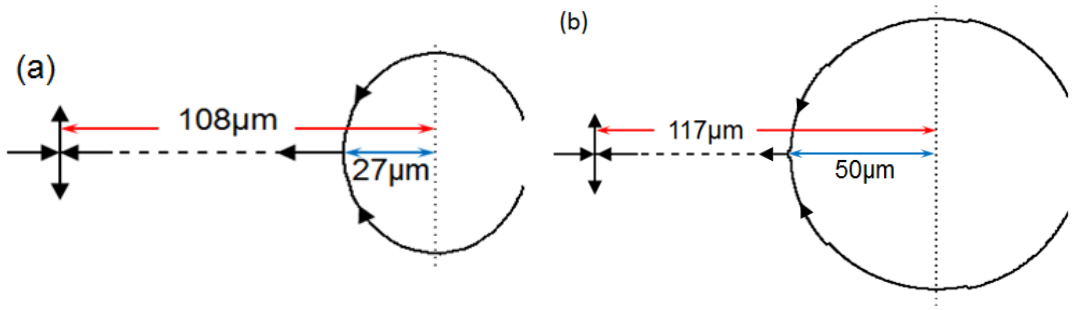

Figure 5.12: Phase plane for two interacting LCS for $\alpha = 9.0$ (a) and $\alpha = 5.0$ (b). The initial, fast phase locking is characterised by the initial sweep from $\Phi = 0.1\pi$ and $\Phi = -0.1\pi$ to the $\Phi = \pi$ phase locked state. The LCS then repel each other and the distance (L) increases.

5.4.2 Cavity soliton interactions with spatially modulated detuning

By introducing a spatially periodic modulation of the VCSEL detuning, we can induce motion of the laser cavity soliton towards a common minimum of the interaction potential. Inducing motion using this method allows us to overcome the repulsive force between the two LCS described previously and, in a similar method to that described in section 5.2, we can use this method to force collisions between two LCS in a VCSEL with FSF. For this purpose, we consider a

triangular modulation of the detuning, as described by equation (5.16).

$$\theta = \theta_0 + \frac{2}{\pi}\mu \sin^{-1}[\sin(k_x x + \varphi_x)] \tag{5.16}$$

Where θ_0 is the background detuning, μ is the amplitude of the modulation, k_x is the transverse wavevector and φ_x is an arbitrary phase shift.

We begin by focusing on two LCS in an initially phase locked state and with a round trip time, $\tau_f = 0.05$ns . The two LCS are created from the same profile, but with a phase shift of π. They are then allowed to relax in localised traps to prevent the repulsive force between the LCS inducing motion. Once the system is relaxed, and the phases of the LCS are locked, the defects are switched to a triangular modulation of the detuning, with each cavity soliton at approximately equal distance from the minima.

Figure 5.13 shows an example of the evolution of the motion towards the common minimum. In figure 5.13 (c), we see that the LCS have merged. Immediately before merging, the LCS begin to destabilise, and oscillate briefly.

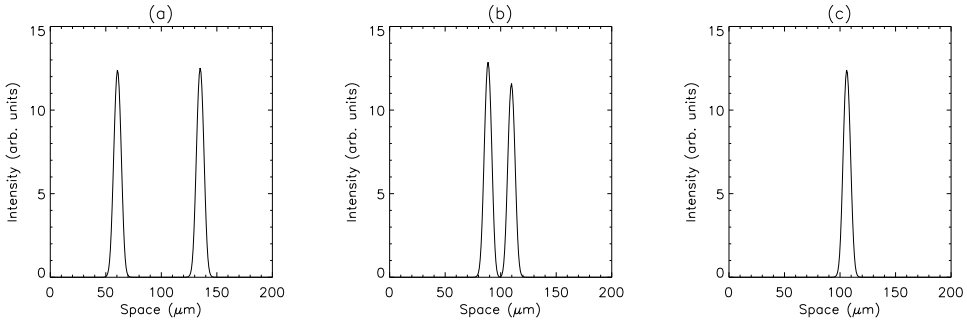

Figure 5.13: Collision of two LCS at the minimum of the detuning modulation. The initial condition is shown in (a) at time $t = 0$ns, (b) $t = 185$ns and (c) $t = 555$ns. The LCS merge after their initial collision. Parameters are $\tau_f = 0.05$ns, $\mu = 2.5$, $k_x = 2.5 \times 10^{-2}$ and $\varphi_x = -1.6$. Other parameters are those of figure 3.9

Now the effect of a longer external cavity length is examined. For this purpose, we use a round trip time of $\tau_f = 0.41$ns. Again, two LCS are created from a single profile with a phase shift of π between them. The LCS are allowed to relax in two localised defects of the detuning, before switching to a periodic modulation. This time, when the LCS collide with each other, they first oscillate but then annihilate each other, leading to a homogeneous "off" state, as shown in figure 5.14.

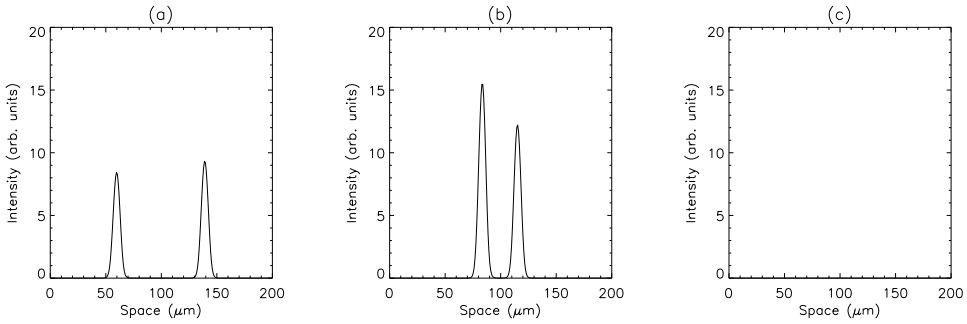

Figure 5.14: Collision of two LCS at the minimum of the detuning modulation. The initial condition is shown in (a) at time $t = 0$ns, (b) $t = 160$ns and (c) $t = 555$ns. The LCS annihilate after their initial collision. Parameters are $\tau_f = 0.41$ns, $\mu = 2.5$, $k_x = 2.5 \times 10^{-2}$ and $\varphi_x = -1.6$. Other parameters are those of figure 3.9

5.4.3 Interactions of laser cavity solitons pinned by local defects

Experimentally, the use of a completely homogeneous background is not physically realistic. Fluctuations during the epitaxial growth process produce localised material defects which pin the LCS to specific locations in the transverse plane of the VCSEL. In order to represent the experimental configuration more realistically, we introduce localised defects into the detuning of our VCSEL. This then allows us to examine the properties of the LCS in a more physically realistic setting.

To simulate these defects, three new parameters are introduced in the numerical simulations. The first is the distance between the first and second defect (*i.e.* the distance between the stationary LCS after relaxation), the second is the width of the defect and the third is the depth of each defect as simulated by a localised change in detuning. In order to pin the LCS, we use a negative change in the local detuning. Positive changes in the values of the local detuning do not pin the LCS as desired. An example of the detuning profile is shown in figure 5.15.

As the position of the LCS is now fixed, the phase plane shows similar behaviour to that of figure 5.12 without the repulsion. The phase of the two LCS quickly evolves to a locked state with a phase difference $\Phi = \pi$. It should be noted that since local defects prevent the motion of LCS, merging or annihilation of spatial solitons (such as those shown in figures 5.13 and 5.14) is not possible in the trapped configuration.

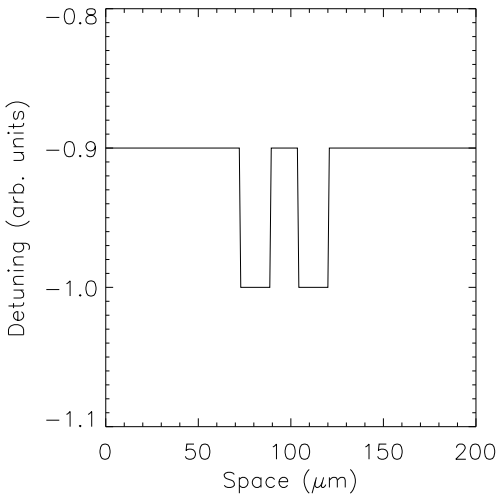

Figure 5.15: An example of the localised defects built into the detuning of the VCSEL with FSF.

Adler locking between two laser cavity solitons

By varying the change in the local detuning of one defect with respect to the other, it is possible to control the value of the phase at which the two LCS lock. Such behaviour is described by the Adler model, which has relevance in biological clocks, chemical reactions and mechanical and electrical oscillators. In optics frequency locking of the Adler type has been observed in lasers with injected signals for a long time [69] with more recent generalisations to coupled lasers [70], the spatio-temporal domain [71], quantum dot lasers [72] and frequency without phase lockings [73].

The archetypal equation describing synchronization between the coupled oscillators is the Adler equation [74, 75],

$$\frac{d\Phi}{dt} = \Delta\omega + \varepsilon \sin(\Phi) \tag{5.17}$$

where in-phase and anti-phase solutions are selected for zero detuning, $\Delta\omega = 0$, depending on the sign of the coupling parameter ε: for positive ε the final stable state is $\Phi = \pi$; for negative ε it is $\Phi = 0$. A comparison of the results of the Adler equation with positive ε and simulations of the synchronisation of LCS in the model with FSF and a more generic cubic complex Ginzburg Landau equation, as shown in [66], are presented in figure 5.16. The agreement is remarkable. In-phase and out-of-phase values have already been observed in numerical simulations of LCS in cubic-quintic complex Ginzburg Landau equations with regular variations

of the background [76, 77, 78] although no Adler scenario is suggested.

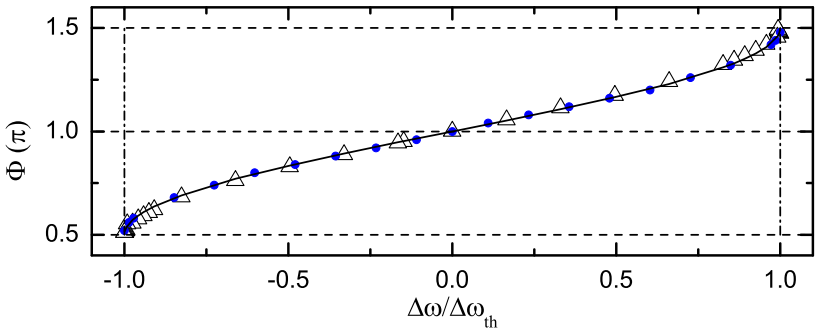

Figure 5.16: Locked phase differences Φ of pinned LCS for different frequency detunings (controlled by the potential depths θ_1 and θ_2) from integration of the cubic complex Ginzburg Landau equation as described in [66] and of the model with FSF. The solid line refers to the Adler equation 5.17.

To characterise the Adler locking both in the spatial and temporal domains, we display the time averaged far field images in the first column of figure 5.17, the optical spectra in the second column of figure 5.17 and the evolution of the phase in the third column of figure 5.17 for two points inside the locking range ($\Delta\omega/\Delta\omega_{th} = 0$ and 0.99) and two outside the Adler region ($\Delta\omega/\Delta\omega_{th} = 2$ and 7.5), respectively. Far field fringes are well defined in the region where the LCS are locked in frequency (see the full overlap of the soliton peaks in the frequency spectrum in figures 5.17 (b) and 5.17 (e)) indicating a strong interaction. For detunings just outside the Adler locking region some phase and spectral correlation survives due to non-uniform evolution of the phase (figures 5.17 (g), 5.17 (h) and 5.17 (i)). For detunings much larger than the locking range, however, the fringe visibility disappears (figure 5.17 (j), 5.17 (k) and 5.17 (l)). In particular, we note that the separation of the frequency in spectra for the individual LCS has separated further and the phase evolution is almost linear and continuous (figures 5.17 (k) and 5.17 (l)).

The Adler locked state between LCS is a robust feature independent of initial phases, frequencies and sequential order of creation of the two LCS. Once the locked state is attained, one of the two LCS can be switched off by a short, localised perturbation to the carrier density at its location. Hence, LCS retain their solitonic properties in the phase-locked state in the sense that they are still individually bistable and optically controllable.

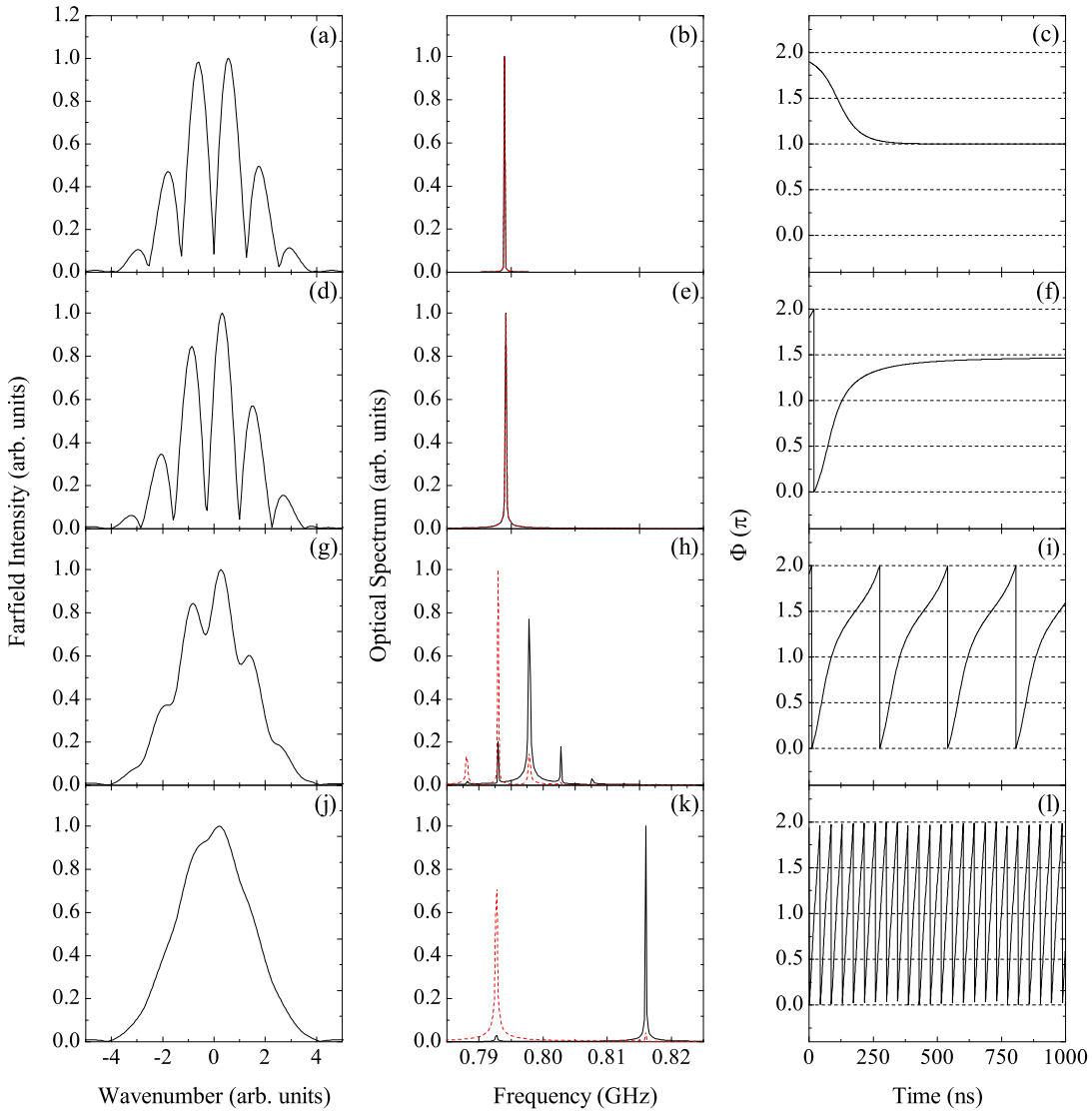

Figure 5.17: Far field images (a, d, g and j) averaged over 2μs, optical spectra (b, e, h and k) for a time window of 5μs and evolution of the phase difference (Φ) (c, f, i and l) for $\Delta\omega/\Delta\omega_{th} = 0$ (a-c), 0.99 (d-f), 2.0 (g-i) and 7.5 (j-l). In (b) and (e) the laser cavity soliton peaks (dashed and solid lines) overlap.

Interactions between three laser cavity solitons

We now briefly examine the effects of introducing a third laser cavity soliton to the system. As discussed previously, two LCS can lock in frequency and phase with respect to each other. When these LCS are pinned by localised defects of the detuning, the position becomes fixed and the phase difference locks in the range $-\pi/2 \leq \Delta\omega \leq \pi/2$. Here we study three LCS pinned by defects of equal depths ($\Delta\omega_{12} = \Delta\omega_{13} = \Delta\omega_{23} = 0$), to examine the effect a third laser cavity soliton has on the phase of the other two. This is achieved by using a single cavity soliton profile (carrier distribution, VCSEL field and feedback field), shifting it to the left and right by the desired distance, and adding the new profiles to the original cavity profiles. Figure 5.18 shows the three LCS used for this purpose. From this, the phase at the peak of CS1 is φ_1, CS2 is φ_2 and CS3 is φ_3.

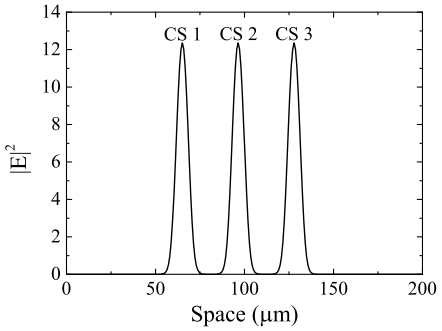

Figure 5.18: An example of three LCS, pinned by traps of equal depth to allow a study of the effects a third cavity soliton has on phase locking.

When the third laser cavity soliton is introduced, we find that the two outer peaks of figure 5.18 lock with phase difference $\Phi_{13} = \varphi_1 - \varphi_3 = 0$, as expected. However the third cavity soliton has the effect of changing the phase difference between the outer two and the inner cavity soliton away from π, resulting in and phase difference $\Phi_{12} = \Phi_{32}, \neq \pi$, where $\Phi_{12} = \varphi_1 - \varphi_2$ and $\Phi_{32} = \varphi_3 - \varphi_2$. We find the value of the phase difference becomes $\Phi_{12} = \Phi_{32} \approx 1.1\pi$, i.e. the value is close to π but is experiencing a shift due to the effect of the interactions between the outer two LCS. Figure 5.19 shows the evolution of the phase difference between the three LCS. This shows that there is an interaction between the outer two LCS, although the effect is weaker than that between the nearest neighbours.

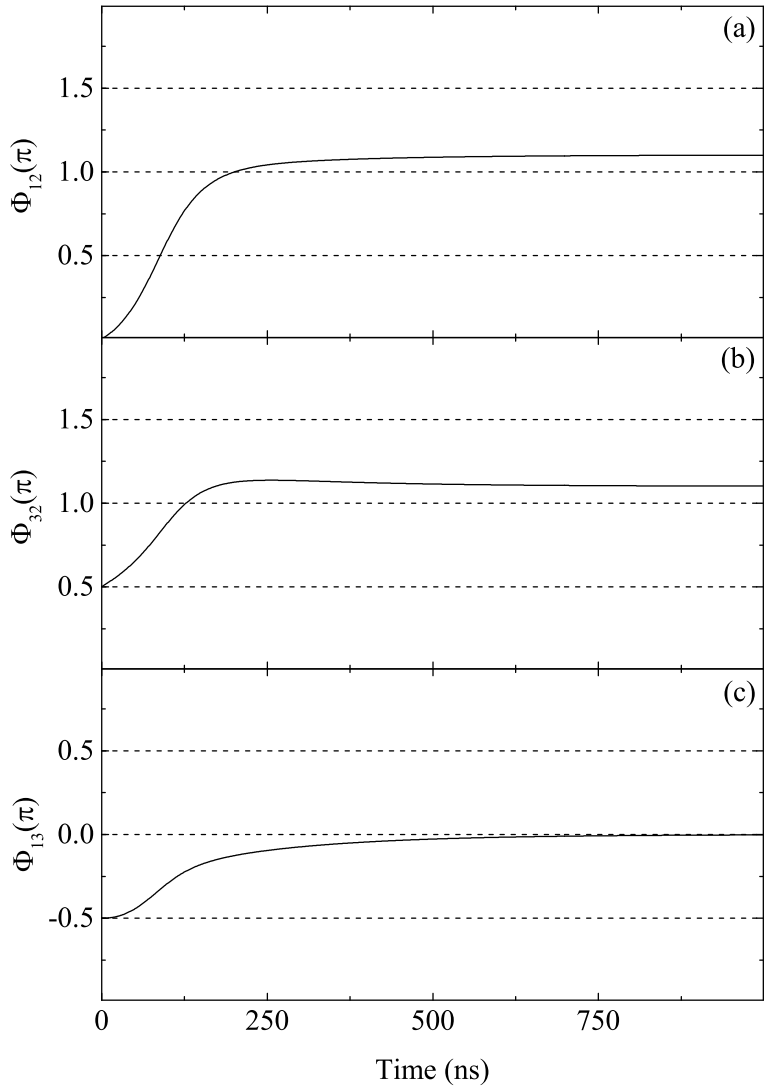

Figure 5.19: An example of three LCS, pinned by traps of equal depth to allow a study of the effects a third cavity soliton has on phase locking. In (a) we show the phase difference $\Phi_{12} = \Delta\varphi_1 - \Delta\varphi_2$, (b) shows $\Phi_{32} = \Delta\varphi_3 - \Delta\varphi_2$ and (c) shows $\Phi_{13} = \Delta\varphi_1 - \Delta\varphi_3$.

5.5 Conclusions

We have shown that cavity soliton interactions can vary greatly in different systems. In the laser with optical injection, a collision between two LCS results in merging, regardless of the phase gradient and therefore velocity. It has also been shown that before and after merging events energy flow in the system is balanced, while during merging there is an initial brief absorption of energy followed by it's release as a pulse of light.

In the Kerr cavity, cavity soliton collisions can have one of three results. The first is a state of pure merging, where the first cavity soliton merges with the structure at the peak. The second is a state of pure locking, where the first locks with the structure at the peak. The third is a state of locking and merging, where the first cavity soliton locks with a multi-peaked structure at the phase maxima and another peak merges as a result. This is due to the multi-soliton solution created by introducing another peak being unstable and the system rearranging itself accordingly.

In the laser with FSF, interactions are more complex due to the fact that the frequency and phase of each cavity soliton can differ from that of its neighbour. We have shown that, for realistic values of the linewidth enhancement factor, two LCS on a homogeneous background initially lock with a phase difference $\Phi = \pi$, before repelling each other, possibly towards an unstable saddle.

Collisions in this case require a gradient to overcome these repulsive effects, and the results have been varied. We have found that for LCS with a shorter external cavity, the two merge to form a single structure at the minimum of the detuning. However for an oscillatory cavity soliton with a longer external cavity, the two peaks destabilise, resulting in the annihilation of both structures. This is most likely due to the fact that the LCS lock to a phase difference $\Phi = \pi$ fairly quickly. When coupled with the longer cavity used to allow oscillations, the phase of the feedback remains locked at $\Phi = \pi$ for longer than that experienced in the shorter cavity and the two LCS essentially act as an erasing beam with respect to each other. Note that no merging or annihilation can take place in the case of conservative solitons. These features are then intrinsically associated to dissipation.

LCS pinned by localised defects remove the repulsive behaviour observed in the homogeneous case and allow for a setup that is closer to that observed experimentally. When the depth of one trap is varied with respect to the other, the LCS display Adler type phase locking until a threshold limit is reached, at which point the frequency and phase of each laser cavity soliton unlocks from that of

its neighbour. When a third laser cavity soliton is introduced, we observe that while the outer structures lock with a phase difference $\Phi_{13} = 0$, they lock with the inner structure with a phase difference $\Phi_{12} = \Phi_{32} \approx 1.1\pi$. This indicates that the outer two LCS are not only interacting with the inner structure but also with each other.

Chapter 6

Oscillations, pulsing and mode locking of laser cavity solitons

6.1 Introduction

Oscillations of Laser Cavity Solitons (LCS) is a relatively new subject. This due to the fact that, while the existence of localised structures in systems designed without an injected field were predicted some time ago [60], CS lasers have only been realised in recent years [39, 51, 79]. In [51], the system consists of two VCSELs mounted in a face to face configuration. The first VCSEL operates above threshold while the second operates below, acting as the saturable absorber. Recent numerical simulations of a model based on this system have revealed the existence of pulsed regimes which can be accessed by increasing the ratio between the carrier lifetime of the active and passive VCSELs [80].

In this chapter we study oscillations and pulsing of LCS in a model and in comparison with experiments of a VCSEL with Frequency Selective Feedback (FSF). For convenience, the model equations of the VCSEL with FSF are reproduced here:

$$\begin{aligned}
\frac{\partial E}{\partial t} &= -\left(1+i\theta\right)E + i\nabla^2 E - i\sigma\left(\alpha+i\right)\left(N-1\right)E + \frac{2\sqrt{T_1}}{\left(T_1+T_2\right)}F \\
\frac{\partial N}{\partial t} &= -\gamma\left[N - J + |E|^2\left(N-1\right)\right] \\
F(t) &= e^{-i\delta\tau_f}\hat{G}\left(t-\frac{\tau_f}{2}\right)\left[-r_1 F\left(t-\tau_f\right) + t_1 E\left(t-\tau_f\right)\right] \\
\hat{G}(t)[h(t)] &= \frac{r_g}{2\beta}\int_{t-2\beta}^{t} e^{i\Omega_g(t'-t)}h(t')dt' \\
\hat{G}(\omega)[h(\omega)] &= r_g e^{-i\beta(\Omega_g-\omega)}sinc(\beta(\Omega_g-\omega))h(\omega)
\end{aligned} \tag{6.1}$$

where E and N are the dynamic field and carrier distributions respectively, θ is the detuning, α is the linewidth enhancement factor, σ is a coupling constant, T_1 and T_2 are the transmittivities of the VCSEL mirrors, J is the current, γ is the decay rate of the carriers, $i\nabla^2 E$ describes diffraction in the laser cavity, τ_f is the external cavity round trip time, δ is the detuning of the external cavity to the reference frequency, r_1 and t_1 are amplitude reflection and transmission coefficients, r_g is the reflection coefficient of the Volume Bragg Grating (VBG), Ω_g is the central grating frequency with $1/\beta$ as the reflected bandwidth.

For the model of a laser with FSF, an initial study of LCS oscillations is presented in [29]. In the example given, the reflection coefficient of the volume Bragg grating, r_g, is used as a control parameter with a short external cavity of round trip time $\tau_f = 0.05$ns, corresponding to an external cavity length of 0.75cm. Using such a short external cavity length has the advantage of providing a larger mode spacing of the frequencies of the external cavity, in this case a spacing of $\Delta\nu = 20$GHz. The reflectivity of the volume Bragg grating is initially set to $r_g = 0.79$ and a stable, single frequency CS is observed with frequency $\omega \approx 17.2$GHz. On increasing the reflectivity of the end reflector to $r_g = 0.85$, a new single frequency CS with frequency $\omega \approx 2.0$GHz appears. This new CS exists in the band of modes adjacent to that containing the original, corresponding in physical terms to a frequency hop between the adjacent external cavity modes.

When an interim value of the reflectivity of the volume Bragg grating is selected, in this case $r_g = 0.83$, the CS contains frequencies corresponding to both of the above external cavity modes, it contains frequency components from both of the single frequency CS described above, resulting in intensity oscillations. Similar results have been observed experimentally. In the experimental case, control parameter becomes the pump current,J, and by increasing the current, one can move from a region where a single frequency soliton exists, to a region where two (or more) external cavity modes are excited before returning to a single frequency state [81].

This phenomenology appears to be quite general and analogous to observations of a laser with transverse modes when changing the cavity length [82], although in the case of the laser with FSF, single transverse mode solutions correspond to single frequency CS. Increasing the cavity round trip time has the consequence of generating sideband instabilities of the single frequency CS followed by the eventual appearance of a new single frequency solution in an adjacent external cavity mode.

As a consequence of the oscillating regimes observed in a laser with frequency

selective feedback, the possibility exists for the detection of mode locked CS oscillations and pulsing. Here we briefly reexamine the external cavity of the VCSEL with FSF before describing the method used to determine if the CS are indeed mode locked.

The VCSEL used in the experimental realisation and the models described in the thesis, while having a large transverse diameter (200μm), have a relatively short longitudinal length. The longitudinal length is typically 1 – 3λ. For this reason, the typical VCSEL has only one principle longitudinal mode on which it can lase, since the spacing between the laser modes is large. The external cavity, on the other hand, is relatively long. In this thesis we have thus far examined round trip times of $\tau_f = 0.05$ns to $\tau_f = 0.41$ns equating to external cavity lengths of approximately 0.75cm to 6cm. Experimental realisations have examined longer external cavities measuring approximately 15cm [50]. As explained in previous chapters, the strong feedback provided by the Volume Bragg Grating (VBG) can lower the VCSEL lasing threshold and can force the VCSEL to lase on different modes which become governed by the external cavity length. Figure 6.1 (a) shows an example of the external cavity. Note that wave shown in this figure is for illustrative purposes only and with the external cavity lengths examined, there typically exists approximately 10^4 – $10^5\lambda$, where λ is the wavelength of the light.

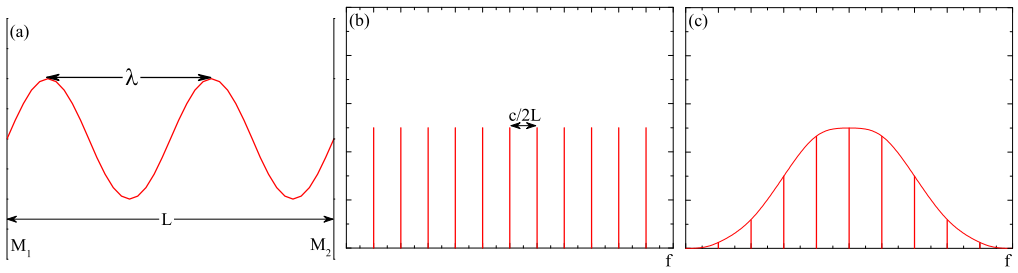

Figure 6.1: An example of the external cavity (a), the mode structure (b) and relative modes within the response range governed by its length (c). In (a) the wave shown is for illustrative purposes only while M_1 and M_2 are the VCSEL output coupler and VBG in this example.

From figure 6.1 (a), the mode separation and, ultimately, the modes relevant to the specific cavity length chosen can be described. These are shown is figure 6.1 (b) and (c). The mode structure is governed by:

$$\Delta f = \frac{c}{2L} = \frac{1}{\tau_f} \tag{6.2}$$

where Δf is the external cavity mode spacing, L is the external cavity length, τ_f

is the external cavity round trip time and c is the speed of light.

In [83], mode locking is defined by comparing the sum of the spectral broadenings, ν_i, of the modes in the optical spectrum with respect to that of the broadening in the RF spectrum, $\Delta\nu_{RF}$, as described in equation 6.3.

$$\Delta\nu_{RF} \ll \sum_{i}^{M} \Delta\nu_i \tag{6.3}$$

Where M is the total number of longitudinal modes in the optical spectrum and $\Delta\nu_i$ is the broadening of the ith mode in the optical spectrum. The criterium states that if the device is passively mode locked, the FWHM linewidth of the RF signal is much smaller than the sum of the spectral linewidths corresponding to all M of the main optical modes [83, 84].

Here we attempt to reproduce the experimental measurements using our model of a VCSEL with FSF. To this end, we first describe LCS oscillations in models of a VCSEL with FSF in section 6.2. We first examine peak oscillations of LCS due to unlocking of external cavity modes, before detailing our search for mode locked oscillations. Next we detail the results on the search for CS pulses and, in particular, for fully self localised three dimensional pulses as described in section 6.3. For each case, we explore the possibility of mode locking in such regimes. Finally, we present experimental results [81, 85] performed by T. Ackemann and N. Radwell for comparison with the numerical results.

6.2 Peak oscillations of laser cavity solitons in models of VCSELs with frequency selective feedback

Here we describe peak oscillations of CS in VCSELs with FSF. Such oscillations correspond to amplitude fluctuations in the peak of the CS. These oscillations are caused by an unlocking of the CS from the single frequency solution where there is only one external cavity mode operating, to a regime where multiple external cavity modes are excited, first described in [29]. As such, depending on the number of external cavity modes active in the CS spectrum, these oscillations can be either (almost) regular in time or they can become irregular to the point where chaotic oscillation dynamics are observed.

6.2.1 Peak oscillations due to unlocking of external cavity modes

As detailed above and in [29], a suitable control parameter can be used to move the system between stable single frequency solutions and multi frequency solutions. Here we focus on two values of the round trip time of the external cavity, $\tau_f = 0.41$ns and $\tau_f = 0.28$ns, to induce oscillations, with fixed values of the other parameters. We introduce figure 6.2, showing the threshold current for the new regime with $\tau_f = 0.28$ns. As before, the gap indicated by the horizontal dashed lines represents the region where both the homogeneous background state and the patterned state are stable.

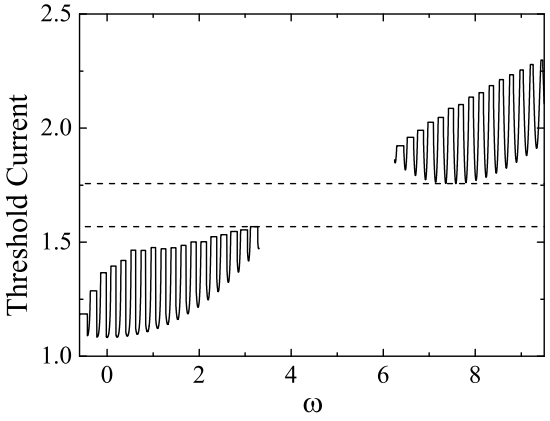

Figure 6.2: Plot of the threshold current as a function of frequency close to the grating frequency. Here $\tau_f = 0.28$ns. The gap indicated between the two horizontal dashed lines shows the region where bistability exists between the homogeneous and patterned states. Other parameters are as shown in figure 3.9.

We begin with the case of an external cavity round trip time, $\tau_f = 0.41$ns. In figure 6.3 (a), the intensity at the peak of the CS is presented for a duration of 30ns after transients have been discarded. These show that the CS is spatially stable and temporally oscillating. Figure 6.3 (b) shows the intensity of the peak of the CS over a shorter time period of (5ns), which shows reasonably regular oscillations as the CS evolves. Figure 6.3 (c) shows the time-frequency spectrogram taken for the peak of the CS. It is clearly visible that, in addition to the main CS frequency, weak side modes are generated, providing the mechanism for oscillations. For a description of the definition and numerical implementation of the spectrogram, see section 3.3.2.

Now we shorten the external cavity round trip time to $\tau_f = 0.28$ns and repeat the above procedure. We introduce figure 6.4 (a) showing the CS peak intensity over a duration of 30ns, while figure 6.4 (b) shows the same intensity over a shorter

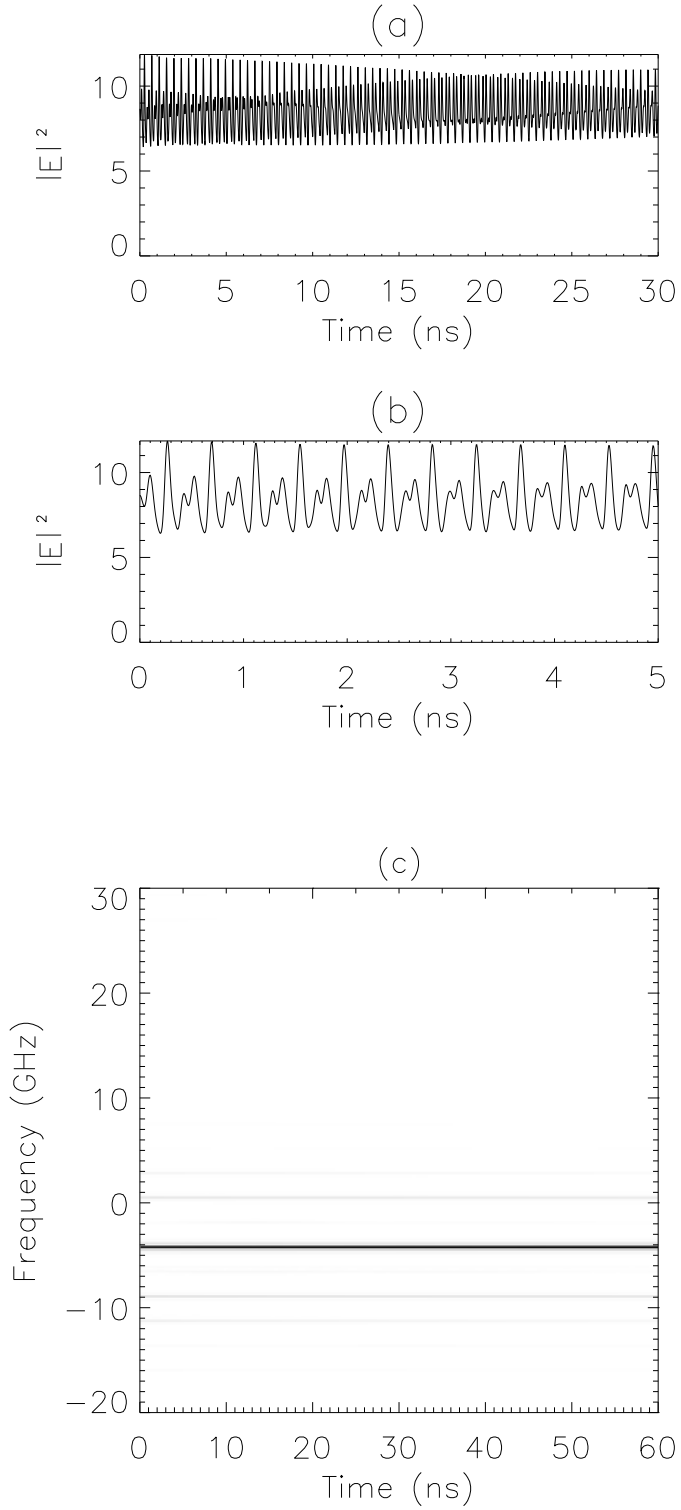

Figure 6.3: An oscillating CS in the VCSEL with FSF for $\tau_f = 0.41$ns. In (a) the CS peak intensity is plotted as a function of time, over 30ns while (b) shows these oscillations over the shorter period of 5ns. In (c) the time-frequency spectrogram of the CS is presented. Other parameters are as figure 3.9.

time period of 5ns. From these figures, we can see the CS oscillations are both sustained and reasonably regular. Figure 6.4 (c) introduces the time-frequency spectrogram for this simulation. We can clearly see one dominant mode and two fairly strong side modes, surrounded by approximately 5 weak side modes.

6.2.2 Search for mode locked oscillations

We now examine the possibility of these oscillations being mode locked. We consider the mode locking criteria as set in section 6.1, and in particular, in equation (6.3). For the case of the stable CS oscillations at $\tau_f = 0.41$ns, we integrate the model equations (6.1) over a long time ($t = 1\mu$s), with a sampling rate of 200GHz, corresponding to an output every 5ps. Figure 6.5 (a) shows the RF spectrum obtained from these numerical simulations while figure 6.5 (b) shows the optical spectrum.

We can clearly see from the figure 6.5 (b) that three external cavity modes are excited, one central mode and two weak side modes. From figure 6.5 (a), the linewidth of the RF spectrum $\Delta\nu_{RF} = 3$MHz and figure 6.5 (b) shows the sum of the broadenings $\sum_i^M \Delta\nu_i \approx 9$MHz. With reference to the mode locking criteria detailed previously $\Delta\nu_{RF} \not\ll \sum_i^M \Delta\nu_i$ and therefore the oscillations are not mode locked.

Subsequently, we examine the oscillations observed with the shorter external cavity, $\tau_f = 0.28$ns, for mode locking against the same criteria. Again, we integrate our model for 1μs with a sampling rate of 200GHz. Figure 6.6 (a) shows the RF spectrum obtained while figure 6.6 (b) shows the optical spectrum.

We can clearly see that there is one central mode with several weak side modes. The linewidth of the RF spectrum for this case is measured as $\Delta\nu_{RF} \approx 30$MHz, while the sum of the optical broadenings is measured to be $\sum_i^M \Delta\nu_i > 300$MHz. From this we conclude that, for this configuration, the peak oscillations of the LCS are mode locked as $\Delta\nu_{RF} \ll \sum_i^M \Delta\nu_i$.

6.2.3 Noisy peak oscillations in the presence of local defects in the VCSEL detuning

We now return to an external cavity round trip time of $\tau_f = 0.41$ns, and introduce a pinning defect, as described in section 5.4.3. In this regime, by introducing an appropriate detuning, we can move from a region where there is bistability, to a region where an oscillating pattern is observed. The use of a localised defect allows us to study temporal oscillations that are transversally localised by

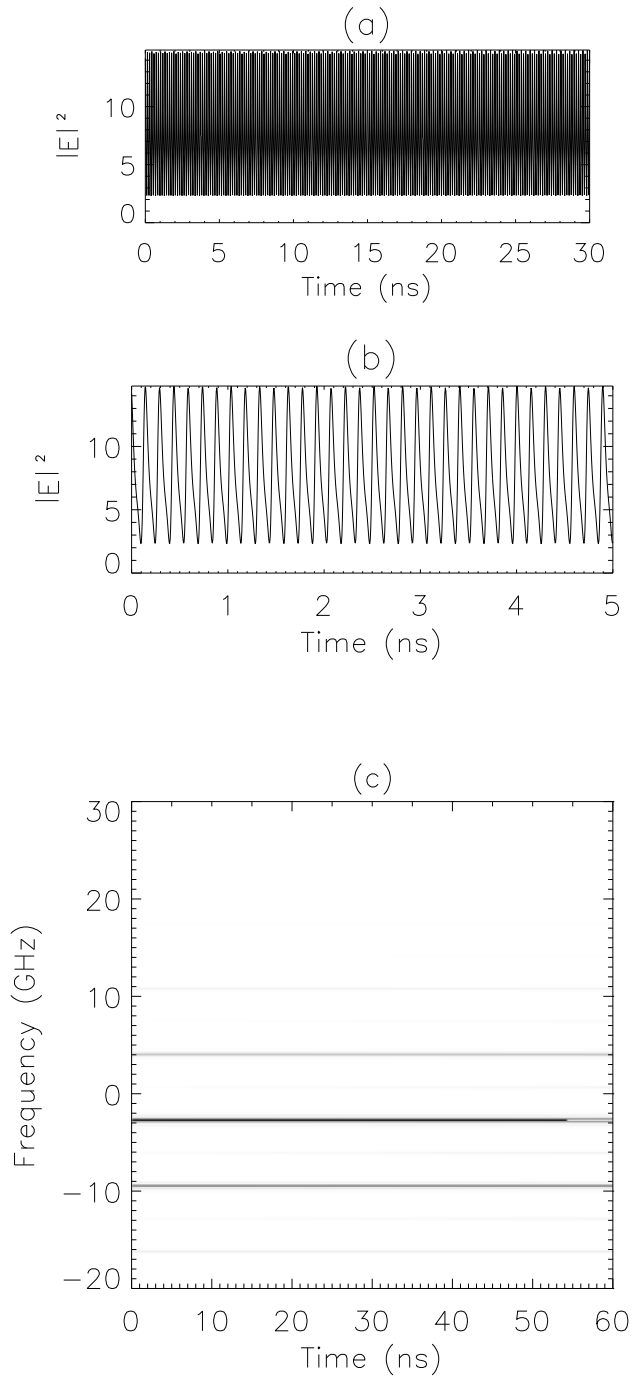

Figure 6.4: An oscillating CS in the VCSEL with FSF for $\tau_f = 0.28$ns. In (a) the CS peak intensity is plotted over a 30ns time scale, while (b) shows the CS peak intensity over a 5ns time scale. Panel (c) shows the time-frequency spectrogram of the CS presented in (a) and (b), taken over a 60ns period. Other parameters are as figure 3.9.

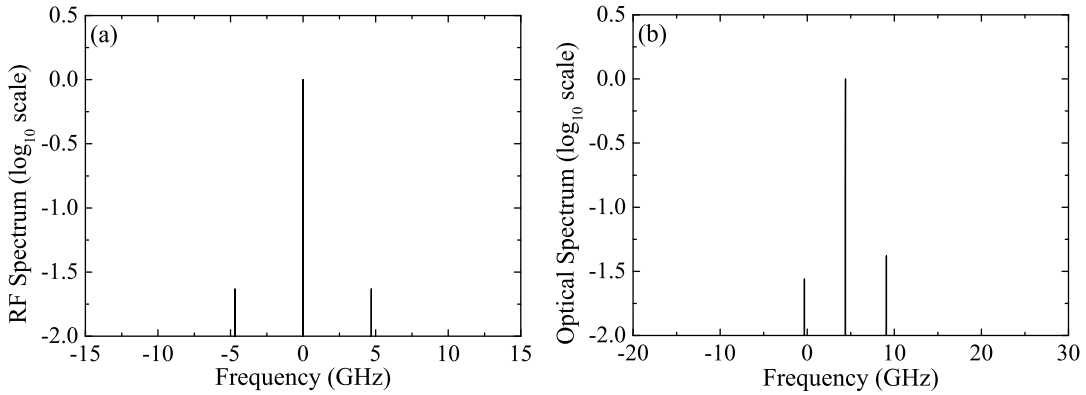

Figure 6.5: The RF spectrum, (a), and the optical spectrum, (b) are presented here. Results are taken from simulations over 1μs with an output every 5ps. The external cavity round trip time is 0.41ns and other parameters are those of figure 3.9.

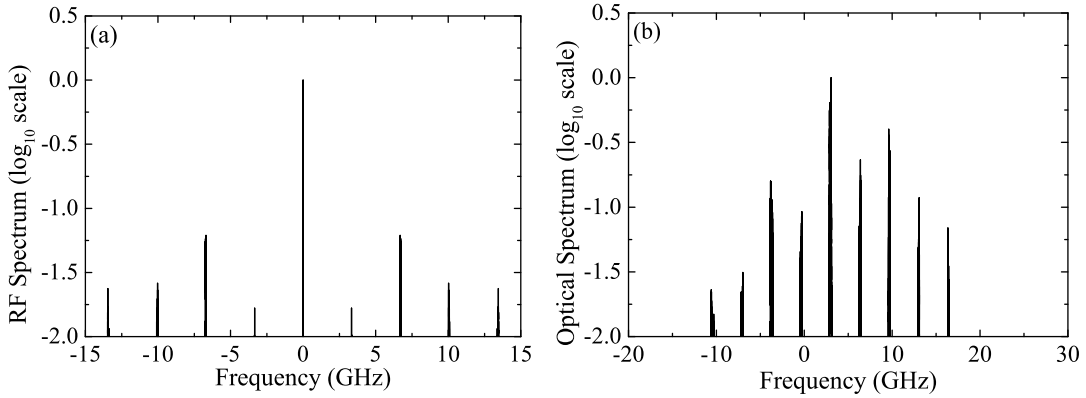

Figure 6.6: The RF spectrum, (a), and the optical spectrum, (b), are presented here. Results are taken from simulations over 1μs with an output every 5ps. The external cavity round trip time is 0.28ns and other parameters are those of figure 3.9.

the defect, a situation that is commonplace in experiments. We introduce figure 6.7 (a), showing the noisy peak oscillations over a duration of 100ns after transients have been discarded. In figure 6.7 (b) and (c), the RF and optical spectra are displayed respectively. Here we can clearly see more modes excited in the optical spectrum when compared to figure 6.5. Further, we calculate the linewidth of the RF spectrum to be $\Delta\nu_{RF} = 3$MHz while the sum of the broadenings of the optical spectrum is $\sum_i^M \Delta\nu_i > 1000$MHz. Therefore we conclude that these noisy oscillations are mode locked in this configuration.

6.3 Pulsing regimes in a laser with frequency selective feedback

The search for full three dimensional self localisation is currently of great interest [86]. In this section we present our results on this topic. To begin with, we introduce two values for τ_f which are exclusive to this section. As such, we present figure 6.8, which shows the threshold current as a function of frequency for our new values, $\tau_f = 1.1$ns, corresponding to an external cavity length of 16.5cm, and $\tau_f = 0.1$ns, corresponding to an external cavity length of 1.5cm.

We begin with the external cavity round trip time, $\tau_f = 1.1$ns. Presented in figure 6.9 are the dynamics of these simulations. In (a), we show the envelope, while (b) shows an enlarged section highlighting the pulses. It is clear from these figures that the CS amplitude either returns to the background state or comes very close to it. Further, it can also be shown that these pulses have a period of $t_p \approx 1.1$ns, therefore $\tau_f \approx t_p$. The time-frequency spectrogram shown in figure 6.9 (c) shows many external cavity modes are contributing to these pulses.

The drawback of this regime, though, is the fact that these pulses are a transient behaviour of the system. The long term implication is that these pulses die out after a few hundred nanoseconds and the system returns to the background state.

We now move to a shorter external cavity of round trip time $\tau_f = 0.10$ns. Here we observe CS pulses with more regularity. Figure 6.10 shows the results obtained with this value of τ_f. In figure 6.10 (a) we show the that the oscillation of the LCS is asymptotically stable by displaying the peak intensity over 60ns. Figure 6.10 (b) shows the oscillations over a shorter time of 2ns, which shows the general shape of the pulses is much smoother than that shown for $\tau_f = 1.1$ns. Finally, figure 6.10 (c) shows the time-frequency spectrogram, again taken at the peak of this CS. Here we observe the existence of two strong modes with three

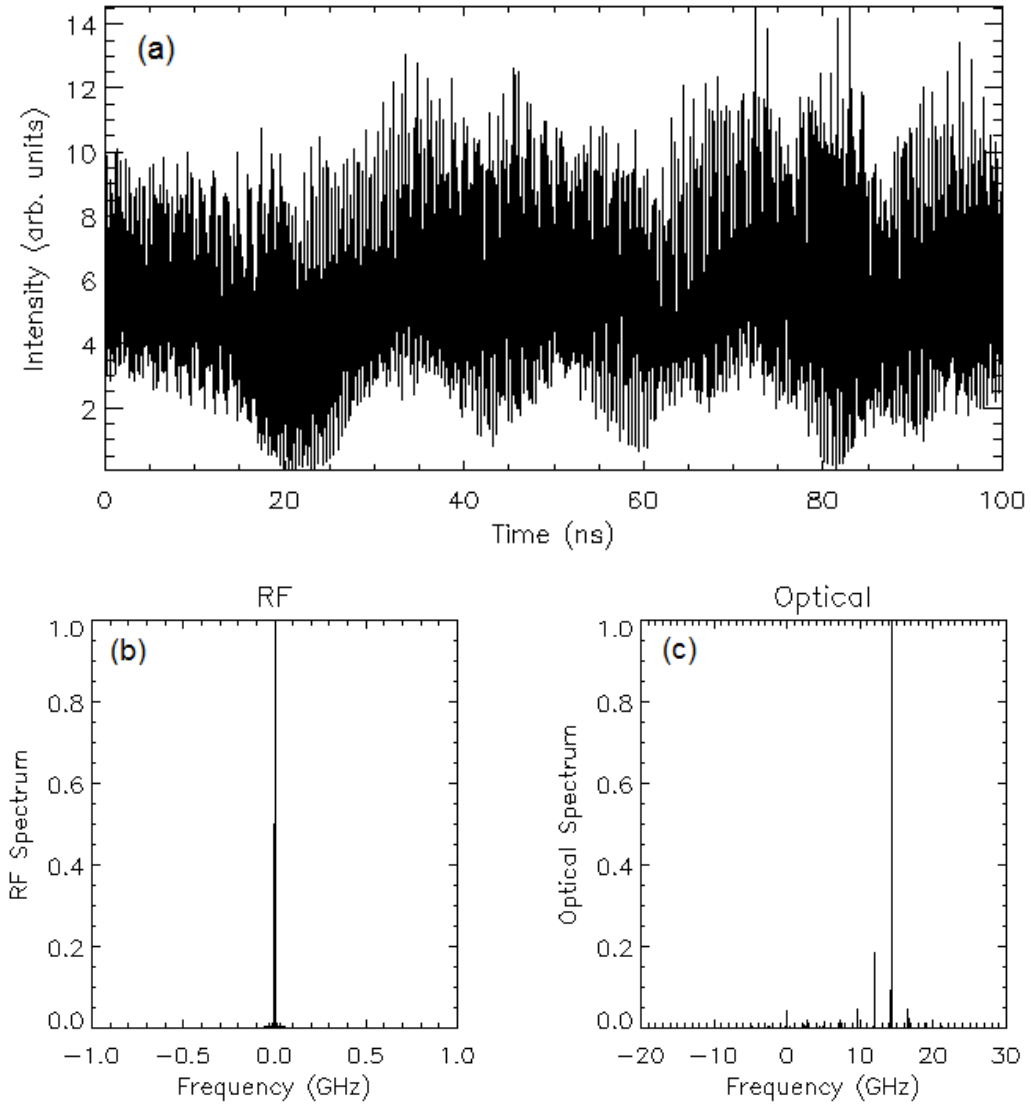

Figure 6.7: The peak oscillation (a), the RF spectrum (b) and the optical spectrum (c) of a localised structure, confined transversely by a local pinning defect. Here the local detuning in the defect is $\theta_t = -1.825$ while the background detuning is $\theta_0 = -1.0$. The external cavity round trip time is $\tau_f = 0.41$ns and other parameters are those of figure 3.9.

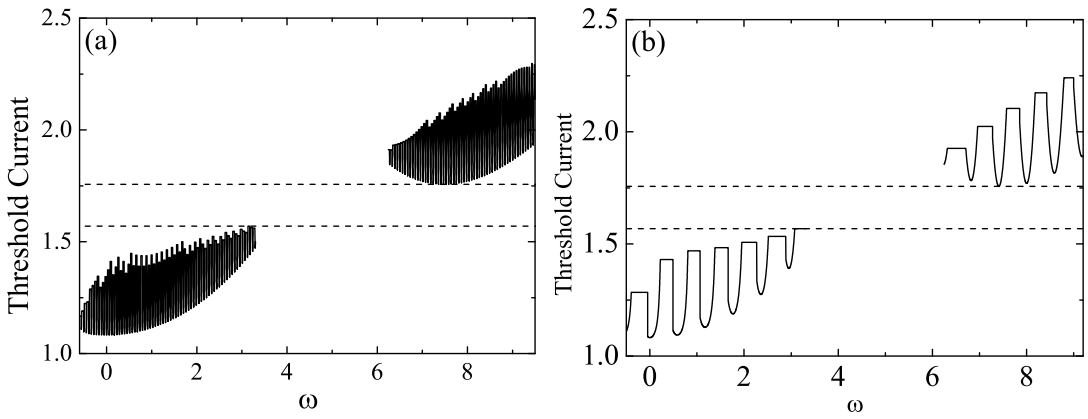

Figure 6.8: Plot of the threshold current as a function of frequency close to the grating frequency. Here, (a) shows $\tau_f = 1.1$ns while (b) shows $\tau_f = 0.10$ns. The gap indicated between the two horizontal dashed lines shows the region where bistability exists between the homogeneous and patterned states. Other parameters are as shown in figure 3.9.

weak side modes participating in the dynamics of the pulsing. The oscillation has an excursion larger than that of section 6.2 but it does not show long intervals around zero, as figure 6.9.

6.3.1 Search for mode locked pulses

Due to the short time scales on which the pulses exist, it is not possible to accurately determine if the pulses with $\tau_f = 1.1$ns are indeed mode locked using the criteria set out at the start of this chapter. Therefore we concentrate here on the case where $\tau_f = 0.1$ns. We integrate the device equations over a long time period ($t = 1\mu$s), with a sampling rate of 200GHz. Figure 6.11 (a) shows the RF spectrum and figure 6.11 (b) shows the corresponding optical spectrum obtained from these simulations.

We can clearly see from figure 6.11 (b) six groups of modes, each with at least ten contributing modes. The two groups of modes between -5GHz and 10GHz which make up the strongest contribution with four weak groups of side modes, in agreement with figure 6.10 (c). We calculate, from figure 6.11, the linewidth of the RF spectrum to be $\Delta\nu_{RF} \approx 30$MHz and the sum of the broadenings of the optical spectrum to be $\sum_i^M \Delta\nu_i \gg 300$MHz. From this, we can clearly see that these oscillations are mode locked as $\Delta\nu_{RF} \ll \sum_i^M \Delta\nu_i$.

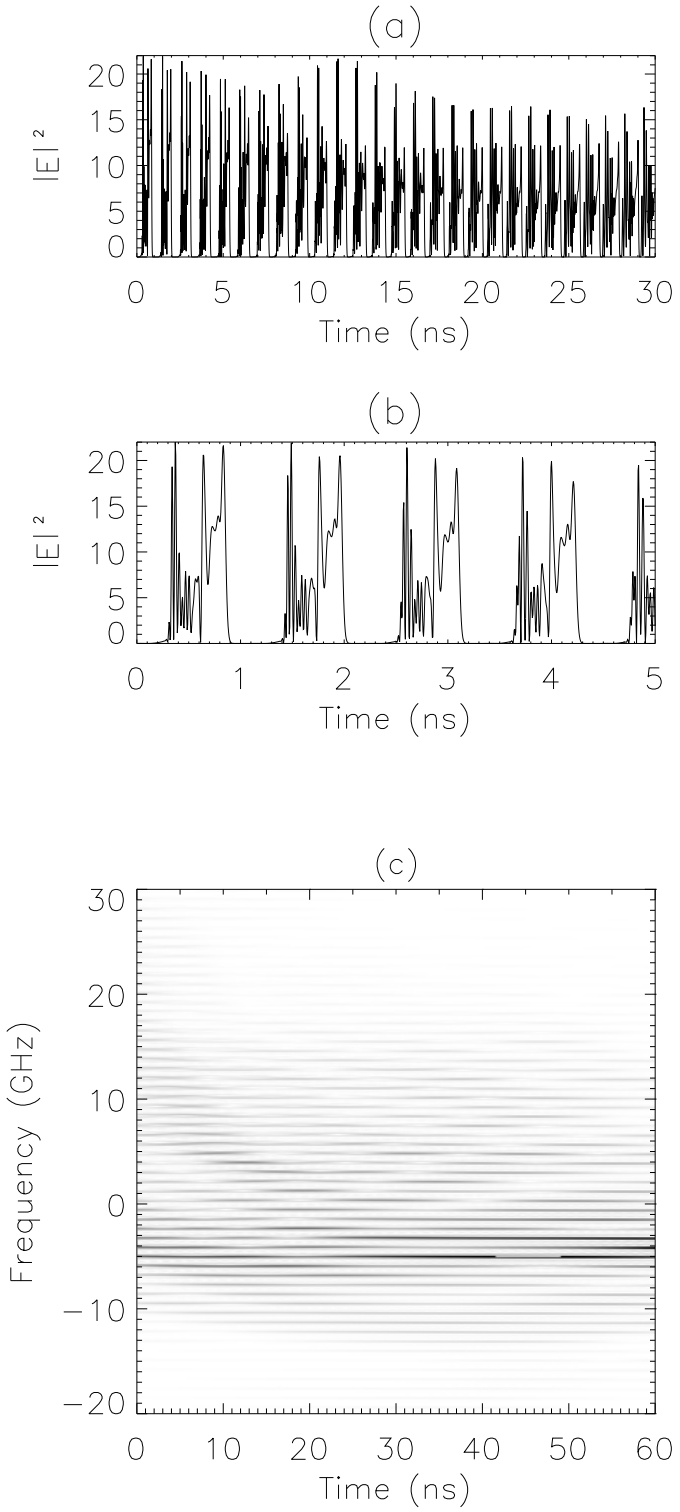

Figure 6.9: An oscillating CS in the VCSEL with FSF for $\tau_f = 1.1$ns. In (a) the CS peak intensity is plotted as a function of time over 30ns, while (b) shows the CS peak intensity plotted over 5ns. In (c) we show the time frequency spectrogram of the CS presented in (a). Other parameters are those of figure 3.9.

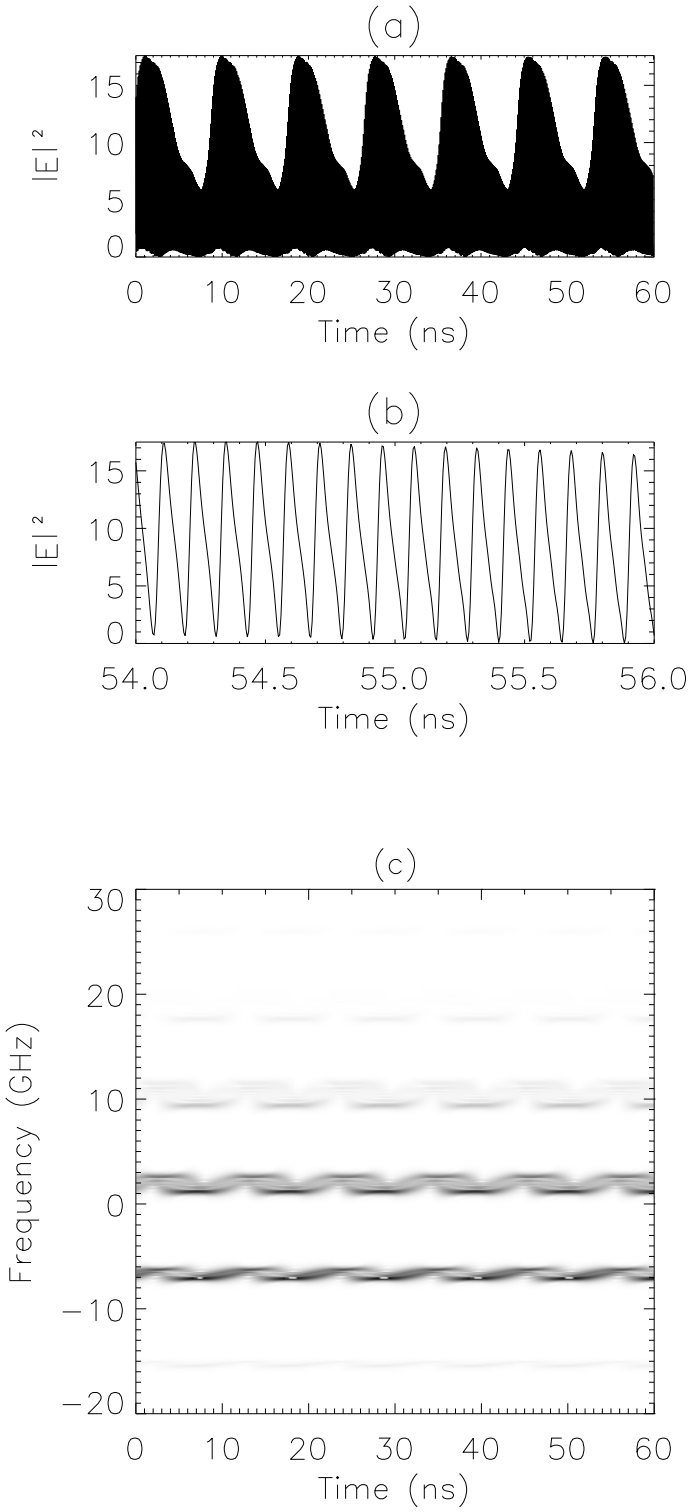

Figure 6.10: An oscillating CS in the VCSEL with FSF for $\tau_f = 0.1$ns. In (a) the CS peak intensity is plotted as a function of time plotted over 60ns, while (b) shows the CS peak intensity plotted over 2ns. In (c) we show the time-frequency spectrogram of the CS presented in (a). Other parameters are those of figure 3.9.

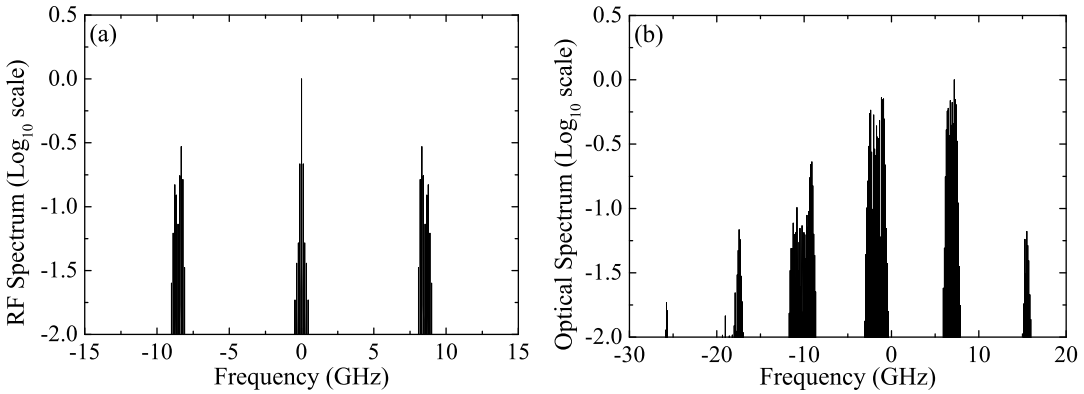

Figure 6.11: The RF spectrum, (a), and the optical spectrum, (b), are presented here for $\tau_f = 0.1$ns. Results are taken from simulations over 1μs with an output every 5ps. Other parameters are those of figure 3.9.

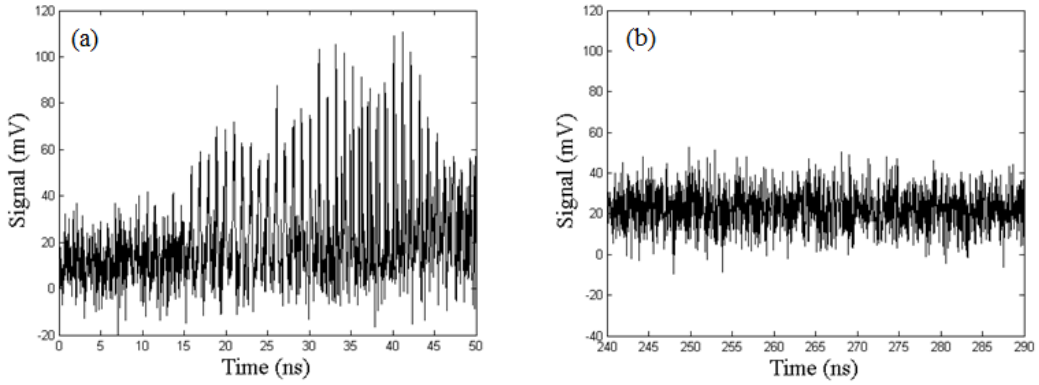

Figure 6.12: Experimental results obtained with a long external cavity with round trip time $\tau_f = 1.1$ns. In (a) we see strong pulsing at the start of the experiment, while (b) shows noisy oscillations in the later stages.

6.4 Experimental results

We now briefly discuss experimental results by N. Radwell and T. Ackemann and that are useful to compare with the numerical simulations of the peak oscillating and pulsing regimes [81, 85]. The experiments are performed with a long external cavity corresponding to a round trip time around $\tau_f = 1.1$ns. In figure 6.12 the early (a) and later (b) stages of the peak intensity of an experimental LCS with FSF are displayed. Initially we observe transient oscillations (figure 6.12 (a)). This is in agreement with the numerical results, although as the experiment continues, noisy peak oscillations are observed instead of the disappearance of the LCS. The initial strong pulsing is determined to be mode locked, while the final noisy oscillations are not.

Next, we introduce the experimental results for a shorter external cavity, with round trip time $\tau_f = 0.61$ns. In figure 6.13 (a) and (b) we show the pulsing

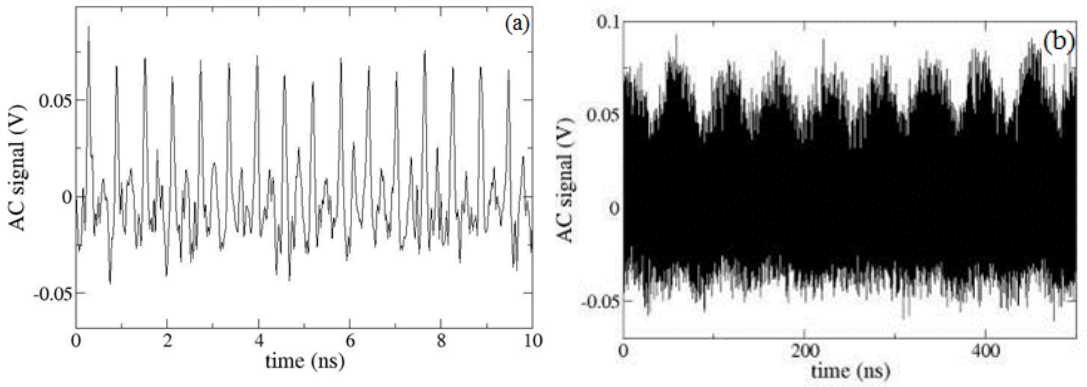

Figure 6.13: Experimental results obtained with a shorter external cavity with round trip time $\tau_f = 0.61$ns. In (a) we see fairly well defined pulsing over a duration of 10ns, while (b) shows the envelope over 500ns.

regime over a duration of 10ns and 500ns respectively. There are clear pulses that are fairly well defined in panel (a) while panel (b) shows these pulses are not of a transient nature. Further, the envelope presented in panel (b) shows some resemblance to that shown for the numerical results with an external cavity round trip time $\tau_f = 0.1$ns, shown in figure 6.10. Finally, for this configuration, the RF linewidth is measured as $\Delta\nu = 5.5$MHz while the sum of the broadenings of the optical modes is $\sum_i^M \Delta\nu_i \geq 30$MHz. We therefore conclude that there are indications of incomplete mode locking for this configuration.

6.5 Conclusions

In this chapter we have successfully shown both oscillating and pulsing LCS. These phenomena are typically not observed in models based on a driven cavity. Beginning with the oscillations, we have shown that these are present for different external cavity lengths, and the external cavity length can assume an important role in governing these oscillations. Further, for the shorter external cavity length, $\tau_f = 0.28$ns, we have observed mode locked oscillations.

Fully localised three-dimensional CS pulses are an active area of exploration. We show pulses in the laser with FSF, again for two external cavity lengths. Firstly we introduce pulsing in a long cavity, comparable to that used during similar experimental research. This shows interesting pulsing effects with contributions from many external cavity modes however we also note that these oscillations appear to be a transient effect. For a shorter cavity, however, we observed well defined stable and regular peak oscillations, whose intensity returns either to zero or very close to zero during each round trip. We show that there

are approximately five or six groups of modes in operation and we note the pulses are separated by approximately 0.12ns. This separation is close to the external cavity round trip time and can be explained by the fact that the VCSEL field evolves on a similar time scale, typically 0.01ns. Further it is also shown that these pulses are mode locked. Therefore, we conclude that these pulses are well confined transversally, display large intensity modulations and are mode-locked. They are a good candidate for the so-called 'light bullets.'

Chapter 7

Conclusions

In this thesis we have investigated the dynamics and interactions of Cavity Solitons (CS) in photonic devices. Our study focused on three models of optical systems, a laser with optical injection, a laser with Frequency Selective Feedback (FSF) and a driven Kerr cavity. We have started with the establishment of CS in all three systems, by use of a spatially localised writing beam with a duration that can be controlled by the operator. We shown how CS can be erased in these systems and generally that there is bistability between the background "off" state and the CS "on" state.

Our CS are optically controllable, by using an appropriate optical gradient in the system. Where possible, control of the position is best achieved by using a gradient in the phase of the optical injection, as this allows for faster drift velocities to be achieved. It is not always possible, however, to control the phase of an optical injection. In particular, systems based on a laser with FSF have no optical injection in which to manipulate. In this case, a gradient can be introduced to the detuning between the laser frequency and the reference frequency. This again allows for drift in the desired direction and is also compatible with systems with optical injection such as the Kerr cavity and the driven laser.

We have shown the effects of collisions between CS in all systems, with each system behaving in its own unique way from each other. For the laser with optical injection, when two (or more) CS collide we exclusively see merging. This occurs, even when the CS are drifting with a low velocity, on a slight gradient. In the Kerr cavity, we observe three different types of behaviour, which can be controlled by varying the applied gradient. We have shown that we can move between regions where the CS merge, where they lock and where we can observe both locking and merging. In both these systems we have also shown that there is energy balance in the system both before and after the CS interactions, as one would expect.

However during the interaction, we see a clear violation of this energy balance with an initial increase in energy in the system before this energy is released and the system returns to the equilibrium value. The laser with FSF shows that we can observe merging or annihilation of the two CS, leaving either one or no CS, respectively.

Further, in the laser with FSF, we have shown that the CS tend to lock their phases, with a phase difference of π between them for our chosen parameters. This locking causes the CS to repel each other. Other parameter regions can of course exhibit phase locking with 0 phase difference, which we expect would allow attraction between the two CS. Further, the CS can be pinned by localised defects. This is a common problem experimentally which we simulate by introducing localised defects in the detuning of the laser. This pins the CS in place however they are still able to lock with π phase difference. We have successfully shown Adler type locking between the two pinned CS when we vary the 'depth' of one of the traps with respect to the other.

We finally introduce CS oscillations and pulsing in our model of a laser with FSF. We have shown that these oscillating and pulsing regimes can be controlled by varying the length of the external cavity in this system. We have shown that the oscillations can be fairly regular although irregular regimes also exist. These oscillations can be either mode locked or unlocked for different external cavity lengths. We have introduced transient pulses with an irregular shape when the system has a long external cavity and also sustained pulses with a much more regular shape for a shorter external cavity length. It has also been shown that these pulses are mode locked for the case of the short external cavity length. Further, on measurement, we find the time between the pulse to be approximately equal to that of the round trip time, indicating that these pulses may indeed be fully self localised three dimensional pulses or "optical bullets."

7.1 Applications based on the properties of these cavity solitons

We now revisit the motivation for the research included in this thesis. In chapter 1, two applications were introduced which would lend themselves well to the properties of CS. Here we discuss these properties and introduce a third applications based on some of the properties discussed in this thesis.

7.1.1 All-Optical Delay Line

The all-optical delay line is well suited to CS, as discussed in [20]. The CS can be written, drift across the transverse plane of the cavity on an optical gradient to be read out and erased. We propose that the read out and erasing procedures can be achieved using CS merging. In the laser with injection, we have shown that the energy balance in the system is violated during the merging process leading to a pulse of light being emitted from the device. This pulse can be used in place of the read-out operation, where a pulse obviously represents a "1" and no pulse represents a "0." Further, the CS is automatically erased during the merging process, removing the need for a separate erasing beam completely [21].

7.1.2 Optical Memories

CS are well suited to the storage of data in optical memories. They can be written and erased independently, at fixed locations in the VCSEL. We propose that the use of a periodic modulation is an ideal method of pinning CS in such a device. Any CS which is written slightly off the correct maxima would automatically reposition itself. Further, merging can introduce a method of error checking. Where a CS is written in an incorrect location, i.e. where a second CS is already placed at the maxima, the new CS would travel to the peak and merge. This merging would release a pulse from the system which could be detected, alerting the operator to the misplaced CS [21, 26].

7.1.3 Optical logic gates

We propose the use of CS for optical logic gates. The properties in these systems would lend themselves well to three types of logic gate, the 'OR' gate, the 'AND' gate and the 'XOR' (exclusive 'OR') gate. The properties of these gates are shown in table 7.1.

Input 1	Input 2	OR	AND	XOR
0	0	0	0	0
1	0	1	0	1
0	1	1	0	1
1	1	1	1	0

Table 7.1: Table showing the input and output states of the 'OR,' 'AND' and 'XOR' logic gates. The first two columns show the input while the third show the respective output for each of the three logic gates.

For the purposes of the 'OR' gate, our laser with injected signal would lend itself well to its implementation. Two writing beams can be utilised as the input parameters, and these writing beams should be located at equal distance on either side of a single peak of a periodic modulation. The CS can then travel to the peak. If there is a CS at the peak then we have a logical '1' while if there is no CS we have a logical '0.' Further the 'AND' gate can be implemented by detecting the pulse given off during the merging process. If a pulse is released from the system them we have a logical '1' and if no pulse is released then we have a logical '0.'

The 'XOR' would require the laser with FSF. In this system, we have observed that the interaction of two CS can cause the annihilation of both CS, given the correct parameters. Here we propose a similar scheme to that described for the 'OR' and 'AND' gates, with two writing beams at an equal distance on either side of a modulation minimum (presuming we are modulating the detuning). If one CS is written on one side of the minimum, the CS will drift to the minimum and remain there, providing a logical '1.' However if two CS are written, they would both drift to the minimum and collide, causing their annihilation and leaving a logical '0.'

7.2 Future developments

The future of this research remains with further exploration of the parameter space. In particular, in the model of a laser with FSF, further characterisation of oscillating and pulsing regimes is required. We have observed regular, sustained pulsing for a short external cavity with length 1.5cm, which is much shorter than the experimental realisation. It would be interesting to refine our parameters further to a region which was more similar to the corresponding experiment. Another parameter which could be explored further in this model is the linewidth enhancement factor, α. The majority of our results use $\alpha = 9.0$, however a more realistic range would be $3.0 \leq \alpha \leq 5.0$.

Further, in appendix A, we introduce the derivation of the model of a laser with double injection. This model was derived and has been tested using similar parameters to those established for the laser with optical injection. Here we have a system which is unexplored, with very little work completed theoretically. Initial experiments have indicated the possibility of observing CS sitting on top of a patterned state with this system, however this has yet to be confirmed in this model.

Appendix A

Derivation of the model of a laser with double injection

In this appendix, we introduce the derivation of a laser with double injection. Again, we consider a VCSEL as our laser for the purpose of this derivation. Here we aim to derive the cavity field through the application of the mean field limit (MFL) to the case of a cavity under the action of two injected (pump) fields. We start from a generic field equation

$$\partial_z \mathcal{F} + \frac{n}{c}\partial_t \mathcal{F} = -\alpha \mathcal{P} + \frac{i}{2k_1}\nabla^2 \mathcal{F} \tag{A.1}$$

where $\mathcal{F}$ is the field in the material, α the susceptibility c the speed of light, $\mathcal{P}$ the polarization, k_1 the wave-vector, and ∇^2 the transverse Laplacian. The boundary condition at the entrance of the medium at $z = 0$ is

$$\mathcal{F}(x, y, 0, t) = e^D \mathcal{F}\left(x, y, L, t - \frac{\mathcal{L} - L}{c}\right) + TE_1(x, y) + TE_2(x, y)e^{i(\Delta k\, z - \Delta\omega\, t)} \tag{A.2}$$

where the propagation operator D is

$$D = \ln R - i\delta + (\mathcal{L} - L)\frac{i}{2k_1}\nabla^2 \tag{A.3a}$$

$$\delta = \frac{\omega_c - \omega_1}{c}\mathcal{L} \qquad T = 1 - R, \tag{A.3b}$$

with R (T) the mirror reflectivity (transmittivity), ω_c the closest cavity mode to the reference frequency, L the length of the medium, $\mathcal{L}$ the length of the cavity, E_1 the amplitude of the first injection, E_2 the amplitude of the second injection,

and where

$$\Delta k = k_2 - k_1 \tag{A.4a}$$

$$\Delta\omega = \omega_2 - \omega_1 \tag{A.4b}$$

are the wave-vector and frequency differences between the two injected fields. Assuming that the frequency and wave-vector of the second injection are close to that of the first injection so that the refractive index n is the same, we have

$$\Delta k = \frac{n\,\Delta\omega}{c}\,. \tag{A.5}$$

Note that the reference system is anchored to the wavelength and frequency of the first injected field. Note also that the reflectivity (transmittivity) R (T) can contain distributed losses such as absorptions during the cavity propagation as long as they do not violate the MFL conditions described later. In the following we will use the transmittivity of the mirror T as a small parameter.

In order to force the boundary condition (A.2) into the propagation equation (A.1), the usual MFL transformation is entered

$$z' = z \tag{A.6a}$$

$$t' = t + \left[\frac{\mathcal{L} - L}{c}\right]\frac{z}{L}\,. \tag{A.6b}$$

Although equation (A.6a) looks trivial, it is there to remind us that z' is a cyclic variable from $z' = 0$ to $z' = \mathcal{L}$, the cavity length. Under the conditions (A.6), we obtain

$$\partial_z = \partial_{z'} + \left[\frac{\mathcal{L} - L}{cL}\right]\partial_{t'} \qquad \partial_t = \partial_{t'} \tag{A.7a}$$

$$\partial_z + \frac{n}{c}\,\partial_t = \partial_{z'} + \left[\frac{\mathcal{L} - L}{cL}\right]\partial_{t'} + \frac{n}{c}\,\partial_{t'} = \partial_{z'} + \left[\frac{\mathcal{L} + (n-1)L}{cL}\right]\,\partial_{t'}\,. \tag{A.7b}$$

Note that the usual MFL transformation of the time variable leaves a refractive index dependence in the coefficient of $\partial_{t'}$. By introducing the new field variable F such that

$$\begin{aligned} F(x,y,z',t') = \Gamma\mathcal{F}(x,y,z',t') &+ TE_1\frac{z'}{L} \\ &+ TE_2\frac{z'}{L}\exp\left\{i\left[\Delta k\left(\frac{\mathcal{L} + (n-1)L}{nL}\right)z' - \Delta\omega\,t'\right]\right\} \end{aligned} \tag{A.8}$$

with

$$\Gamma = \exp\left(D\frac{z'}{L}\right) , \tag{A.9}$$

we first obtain a synchronous longitudinal boundary condition

$$F(x,y,0,t') = \mathcal{F}(x,y,0,t') = F(x,y,L,t') \tag{A.10}$$

and then

$$\partial_{t'}F = \Gamma\partial_{t'}\mathcal{F} - i\Delta\omega\, TE_2\frac{z'}{L}\exp\{...\} \tag{A.11a}$$

$$\begin{aligned}\partial_{z'}F = {} & \Gamma\partial_{z'}\mathcal{F} + \frac{D}{L}\left(F - TE_1\frac{z'}{L} - TE_2\frac{z'}{L}\exp\{...\}\right) + TE_1\frac{1}{L} \\ & + TE_2\frac{1}{L}\exp\{...\} + i\Delta k\left(\frac{\mathcal{L}+(n-1)L}{nL}\right)TE_2\frac{z'}{L}\exp\{...\}\end{aligned} \tag{A.11b}$$

where $\exp\{...\}$ is the exponential in the last term of equation (A.8). This leads to the dynamical equation for the field F

$$\begin{aligned}&\partial_{t'}F + \frac{cL}{\mathcal{L}+(n-1)L}\quad\partial_{z'}F \\ &\quad = \frac{c}{\mathcal{L}+(n-1)L}\Bigg[D\left(F - TE_1\frac{z}{L} - TE_2\frac{z'}{L}\exp\{...\}\right) + \Gamma L\left(\partial_z\mathcal{F} + \frac{n}{c}\,\partial_t\mathcal{F}\right) \\ &\quad + TE_1 + TE_2\exp\{...\}\Bigg] + i\left(\Delta k\frac{c}{n} - \Delta\omega\right)TE_2\frac{z'}{L}\exp\{...\}\end{aligned} \tag{A.12a}$$

$$\begin{aligned}&\quad = \frac{c}{\mathcal{L}+(n-1)L}\Bigg[D\left(F_j - TE_1\frac{z}{L} - TE_2\frac{z'}{L}\exp\{...\}\right) + \left(-\alpha L\Gamma\mathcal{P} + \frac{iL}{2k_1}\nabla^2 F\right) \\ &\quad + TE_1 + TE_2\exp\{...\}\Bigg] .\end{aligned} \tag{A.12b}$$

Note that the last term in E_2 coming from the derivatives of the phase shift of the second injection comes out to be identically zero.

Under the usual MFL assumptions, i.e.

$$\begin{aligned} T \ll 1; \qquad & \delta = O(T) \ll 1; \\ (\mathcal{L}-L)/2k_1 = O(T) \ll 1 & \end{aligned} \tag{A.13}$$

one obtains

$$D \approx T\left[-(1+i\theta)+i\frac{\mathcal{L}-L}{2k_1T}\nabla^2\right] \qquad \Gamma_j \approx 1+\frac{D}{L}z \tag{A.14}$$

which, at the first order in T leads to

$$\begin{aligned}\partial_{t'}F+\frac{cL}{\mathcal{L}+(n-1)L}\ \partial_{z'}F \\ = K\Bigg[-\frac{\alpha L}{T}\mathcal{P}-(1+i\theta)F+ia\nabla^2F+E_1 \\ +E_2\exp\left\{i\left[\Delta k\left(\frac{\mathcal{L}+(n-1)L}{nL}\right)z'-\Delta\omega\ t'\right]\right\}\Bigg]\end{aligned} \tag{A.15}$$

where we have defined the field decay rate and the diffraction parameter as:

$$K=\frac{cT}{\mathcal{L}+(n-1)L} \tag{A.16a}$$

$$a=\frac{\mathcal{L}}{2Tk_1}\,. \tag{A.16b}$$

At this point of the MFL procedure one expands all variables in a Fourier series of longitudinal modes, considers that longitudinal modes are well separated (this is particularly true for VCSEL cavities that are extremely short), retains only the zero-spatial-frequency mode and drops the $\partial_{z'}F$ derivative in the equation (A.15). However we have an explicit dependence from z' in the phase of the second injection. Let us consider such phase term over a single round trip:

$$\Delta k\left(\frac{\mathcal{L}+(n-1)L}{nL}\right)\mathcal{L}=\frac{\Delta k}{k_1}\left(\frac{\mathcal{L}+(n-1)L}{nL}\right)k_1\mathcal{L}\,. \tag{A.17}$$

If we consider the reasonable assumption

$$\frac{\Delta k}{k_1}=\frac{\lambda_1-\lambda_2}{\lambda_2}=O(T) \tag{A.18}$$

then the phase shift due to the z' spatial term of the phase of the second injection is negligible ($O(T)$) during a round trip since the length of the VCSEL cavity is only few times longer than the lasing wavelength. This means that the MFL procedure described above retains validity since it is correct at order zero in T. However the small phase shift of the second injection accumulates round trip after round trip so that it would be incorrect to neglect it on secular time scales. To

consider it properly on long time scales we write

$$\Delta\Phi = \Delta\omega \left[\left(\frac{\mathcal{L} + (n-1)L}{cL} \right) z' - \Delta\omega \, t' \right] \tag{A.19}$$

and consider the cyclic nature of the z' variable. After many round trips

$$\Delta\Phi = \Delta\omega \left(\frac{n\mathcal{L}}{c} - t \right) . \tag{A.20}$$

The first term in the parenthesis is of order T while the second keeps increasing with t. As a consequence after the MFL procedure we can rewrite equation (A.15) as:

$$\partial_t F = K \left[-\frac{\alpha L}{T}\mathcal{P} - (1+i\theta)F + ia\nabla^2 F + E_1 + E_2 e^{-i\Delta\omega \, t} \right] . \tag{A.21}$$

The second injection acts as a periodic forcing on the equations with a single injection. The frequency of the forcing is given by the frequency separation between the two injections in the limit of small changes of wavelength between the two injections.

References

[1] A. Einstein, Annalen der Physik **17**, 132 (1905).

[2] C. C. Davis, *Lasers and Electro-Optics: Fundamentals and Engineering*, Cambridge Univeristy Press, Cambridge, New York, 1996.

[3] S. H. Strogatz, *Nonlinear dynamics and chaos*, Perseus Books Group, 1994.

[4] J. Rinzel and G. B. Ermentrout, *Methods in neuronal modelling: from synapses to netwroks*, Analysis of neural excitabitlity and oscillations, MIT Press, Cambridge, MA, 1989.

[5] E. H. Dowell and M. Ilgamova, *Studies in nonlinear Aeroelasticity*, Springer, New York, 1988.

[6] J. M. T. Thompson and H. B. Stewart, *Nonlinear dynamics and chaos*, Wiley, Chichester, U.K., 1986.

[7] P. G. Drazin, *Nonlinear systems*, Cambridge University Press, Cambridge, U.K., 1981.

[8] A. M. Turing, Phil. Trans. R. Soc. Lond. B **237**, 37 (1952).

[9] M. C. Cross and P. C. Hohenberg, Rev. Mod. Phys. **65**, 851 (1993).

[10] J. D. Murray, *Mathematical biology*, Springer, Berlin, 1989.

[11] L. A. Lugiato and R. Lefever, Phys. Rev. Lett **58**, 2209 (1987).

[12] G.-L. Oppo, M. Brambilla, and L. A. Lugiato, Phys. Rev. A **49**, 2028 (1994).

[13] G.-L. Oppo, J. Math. Chem. **45**, 95 (2007).

[14] J. S. Russell, Report on waves, in *Rep. Brit. Assoc. for the Advancement of Science*, page 311, 1844.

[15] A. C. Newell, *Solitons in mathematics and physics*, SIAM, Philidelphia, 1985.

[16] J. Boussinesq, J. Math. Pures Appl. **17**, 55 (1872).

[17] S. Trillo and W. Torruellas, *Spatial solitons*, Springer, 2001.

[18] A. C. Scott, *Encyclopedia of nonlinear science*, Routledge, Taylor and Francis Group, New York, 2005.

[19] T. Ackemann and W. Firth, Dissipative solitons in pattern-forming nonlinear optical systems: Cavity solitons and feedback solitons, in *Dissipative Solitons*, edited by N. Akhmediev and A. Ankiewicz, volume 661 of *Lecture Notes in Physics*, page 55, Springer Berlin Heidelberg, 2005.

[20] F. Pedaci et al., Appl. Phys. Lett. **92**, 011101 (2008).

[21] C. McIntyre, A. M. Yao, G. L. Oppo, F. Prati, and G. Tissoni, Phys. Rev. A **81**, 013838 (2010).

[22] S. Barland et al., Nature **419**, 699 (2002).

[23] L. A. Lugiato and L. M. Narducci, Fundamental systems in quantum optics, in *Les Houches School, Session LIII, 1990*, (Elsevier, Amsterdam, 1992).

[24] A. J. Scroggie, *Spontaneous Optical Patterns in Two and Four Level Atomic Systems*, PhD thesis, Dept. of Physics, University of Strathclyde, 1995.

[25] X. Hachair et al., IEEE J. Sel. Top. Quantum Electron. **12**, 339 (2006).

[26] F. Prati, G. Tissoni, C. McIntyre, and G. L. Oppo, Eur. Phys. J. D **59**, 139 (2010).

[27] G. L.Oppo, A. M. Yao, F. Prati, and G. deValcaracel, Phys. Rev. A **79**, 033824 (2009).

[28] D. M. Kane and K. A. Shore, *Unlocking Dynamical Diversity: Optical Feedback Effects on Semiconductor Lasers*, Wiley, New York, 2004.

[29] A. J. Scroggie, W. J. Firth, and G. L. Oppo, Phys. Rev. A **80**, 013829 (2009).

[30] L. Spinelli, G. Tissoni, M. Bramilla, F. Prati, and L. A. Lugiato, Phys. Rev. A **58**, 2542 (1998).

[31] M. Giudici, S. Balle, T. Ackemann, S. Barland, and J. R. Tredicce, J. Opt. Soc. B **16**, 2114 (1999).

[32] P. V. Paulau et al., Phys. Rev. E **75**, 056208 (2007).

[33] P. V. Paulau, D. Gomilla, T. Ackemann, N. A. Loiko, and W. J. Firth, Phys. Rev. E **78**, 016212 (2008).

[34] R. Lang and K. Kobayashi, IEEE J. Quantum. Electron. **16**, 347 (1980).

[35] G. H. M. van Tartwijk and D. Lenstra, Quantum Semiclassic. Opt. **7**, 87 (1995).

[36] D. Pieroux and P. Mandel, Phys. Rev. E **68**, 036204 (2003).

[37] M. Yousefi, D. Lenstra, and G. Vemuri, Phys. Rev. E **67**, 046213 (2003).

[38] N. Radwell and T. Ackemann, preprint (2009).

[39] Y. Tanguy, T. Ackemann, W. J. Firth, and R. Jäger, Phys. Rev. Lett. **100**, 013907 (2008).

[40] Y. Tanguy, N. Radwell, T. Ackemann, and R. Jäger, Phys. Rev. A **78**, 023810 (2008).

[41] W. H. Press, B. P. Flannery, S. A. Teukolsky, and W. T. Vetterling, *Numerical Recipes: The Art of Scientific Computing*, Cambridge Univeristy Press, 1986.

[42] W. H. Press, S. A. Teukolsky, W. T. Vetterling, and B. P. Flannery, *Numerical Recipes: The Art of Scientific Computing*, Cambridge Univeristy Press, 2007.

[43] T. Ackemann, W. J. Firth, and G. L. Oppo, Adv. in At., Mol. and Opt. Phys. **57**, 323 (2009).

[44] A. Schreiber, M. Kreuzer, B. Thüring, and T. Tschudi, Opt. Comm. **163**, 415 (1997).

[45] S. Barbay et al., Opt. Lett. **31**, 1504 (2006).

[46] P. V. Paulau et al., Phys. Rev. Lett. **108**, 213904 (2012).

[47] X. Hachair et al., Phys. Rev. A **69**, 043817 (2004).

[48] G. S. McDonald and W. J. Firth, J. Opt. Soc. Am. B **7**, 1328 (1990).

[49] Y. Tanguy, T. Ackemann, and R. Jäger, Opt. Express **15**, 16773 (2007).

[50] N. Radwell et al., Eur. Phys. J. D **59**, 121 (2010).

[51] P. Genevet, S. Barland, M. Giudici, and J. R. Tredicce, Phys. Rev. Lett. **101**, 123905 (2008).

[52] P. Genevet, S. Barland, M. Giudici, and J. R. Tredicce, Phys. Rev. A **79**, 033819 (2009).

[53] V. B. Taranenko and C. O. Weiss, Lect. Notes. Phys. **613**, 373 (2003).

[54] W. J. Firth and A. J. Scroggie, Phys. Rev. Lett. **76**, 1623 (1996).

[55] A. J. Scroggie, J. M. McSloy, and W. J. Firth, Phys. Rev. E **66**, 036607 (2002).

[56] A. J. Scroggie, J. Jeffers, G. McCartney, and G. L. Oppo, Phys. Rev. E **71**, 046602 (2005).

[57] F. Pedaci, P. Genevet, S. Barland, M. Giudici, and J. R. Tredicce, Appl. Phys. Lett. **89**, 221111 (2006).

[58] E. Caboche et al., Phys. Rev. A **80**, 053814 (2009).

[59] E. Caboche et al., Phys. Rev. Lett. **102**, 163901 (2009).

[60] N. N. Rosnaov, Opt. Spectrosc. **72**, 243 (1992).

[61] I. Rabbiosi, A. J. Scroggie, and G. L. Oppo, Phys. Rev. Lett. **89**, 254102 (2003).

[62] N. Akhmediev and A. Ankiewcz, Dissipative solitons, in *Dissipative Solitons*, Springer, 2004.

[63] N. N. Akhmediev, A. Ankiewicz, and J. M. Soto-Crespo, Phys. Rev. Lett. **79**, 4047 (1997).

[64] P. Grelu and N. Akhmediev, Nat. Photon. **6**, 84 (2012).

[65] T. Ackemann et al., Frequency and phase locking of laser cavity solitons, in *Spontaneous Symmetry Breaking, Self-Trapping, and Josephson Oscillations in Nonlinear Systems*, edited by B. Malomed, volume 1 of *Progress in Optical Science and Photonics*, Springer, Expected 2013.

[66] P. V. Paulau, D. Gomila, P. Colet, B. A. Malomed, and W. J. Firth, Phys. Rev. E **34**, 036213 (2011).

[67] D. Turaev, A. G. Vladimirov, and S. Zelik, Phys. Rev. E **75**, 045601(R) (2007).

[68] A. G. Vladimirov, G. V. Khodova, and N. N. Rosanov, Phys. Rev. E **63**, 056607 (2001).

[69] C. J. Buczek, R. J. Freiberg, and M. L. Skolnick, Proc. IEEE **61**, 1411 (1973).

[70] L. Fabiny, P. Colet, R. Roy, and D. Lenstra, Phys. Rev. A **47**, 4287 (1993).

[71] P. Coullet, D. Daboussy, and J. R. Tredicce, Phys. Rev. E **58**, 5347 (1998).

[72] D. Goulding et al., Phys. Rev. Lett. **98**, 153903 (2007).

[73] J. Thevenin, M. Romanelli, M. Vallet, M. Brunel, and T. Erneux, Phys. Rev. Lett. **107**, 104101 (2011).

[74] R. Adler, Proc. IRE **34**, 351 (1946).

[75] R. Adler, Proc. IEEE **61**, 1380 (1973).

[76] Y. J. He et al., Opt. Lett. **34**, 2976 (2009).

[77] W. Chang, N. Akhmediev, and S. Wabnitz, Phys. Rev. A **80**, 013815 (2009).

[78] W. Chang, N. Akhmediev, S. Wabnitz, and M. Taki, J. Opt. Soc. Am. B **26**, 2204 (2009).

[79] T. Elsass et al., Appl. Phys. B **98**, 327 (2010).

[80] G. Tissoni, F. Prati, and M. Brambilla, Pulsing and excitable solitons in a semiconductor laser with saturable absorber, in *CLEO/Europe and EQEC 2011 Conference Digest*, (Optical Society of America, 2011).

[81] N. Radwell, *Characteristics of a cavity soliton laser based on a VCSEL with frequency selective feedback*, PhD thesis, Dept. of Physics, University of Strathclyde, 2010.

[82] L. A. Lugiato, G. L. Oppo, J. R. Tredicce, L. M. Narducci, and M. A. Pernigo, J. Opt. Soc. Am. B **7**, 1019 (1990).

[83] R. Maldonado-Basilio, S. Latkowski, F. Surre, and P. Landais, Opt. Comm. **283**, 299 (2010).

[84] S. Latkowski, R. Maldonado-Basilio, and P. Landais, Opt. Express **17**, 19166 (2009).

[85] C. McIntyre, G.-L. Oppo, N. Radwell, T. Ackemann, and W. Firth, Mode-locked laser cavity solitons, in *CLEO/Europe and EQEC 2011 Conference Digest*, (Optical Society of America, 2011).

[86] F. W. Wise and P. DiTrapani, Opt. Photon. News **13**, 28 (2002).